UNIVERSITY OF SEVILLE

DOCTORAL THESIS

Velocity-space resolved measurements of fast-ion losses due to magnetohydrodynamic instabilities in the ASDEX Upgrade tokamak

Author:
Joaquin Galdon-Quiroga

Supervisor:
Dr. Manuel Garcia-Munoz
Dr. Eleonora Viezzer

A thesis submitted in fulfillment of the requirements for the degree of Doctor of Philosophy

in the

Plasma Science and Fusion Technology Group
Department of Atomic, Molecular and Nuclear Physics

October 3, 2018

Declaration of Authorship

I, Joaquin Galdon-Quiroga, declare that this thesis titled, "Velocity-space resolved measurements of fast-ion losses due to magnetohydrodynamic instabilities in the ASDEX Upgrade tokamak" and the work presented in it are my own. I confirm that:

- This work was done wholly or mainly while in candidature for a research degree at this University.
- Where any part of this thesis has previously been submitted for a degree or any other qualification at this University or any other institution, this has been clearly stated.
- Where I have consulted the published work of others, this is always clearly attributed.
- Where I have quoted from the work of others, the source is always given. With the exception of such quotations, this thesis is entirely my own work.
- I have acknowledged all main sources of help.
- Where the thesis is based on work done by myself jointly with others, I have made clear exactly what was done by others and what I have contributed myself.

Signed:

Date:

A mis padres, Reyes y Manuel…

UNIVERSITY OF SEVILLE

Abstract

Faculty of Physics
Department of Atomic, Molecular and Nuclear Physics

Doctor of Philosophy

Velocity-space resolved measurements of fast-ion losses due to magnetohydrodynamic instabilities in the ASDEX Upgrade tokamak

by Joaquin Galdon-Quiroga

The confinement of suprathermal ions in magnetically confined fusion plasmas is essential to ensure a good fusion performance. Auxiliary heating systems - and fusion reactions themselves - create fast-ion populations, which must be confined for long enough time to transfer their energy to the bulk of the plasma via Coulomb collisions. A good confinement of the fast-ions is needed to ensure a good plasma heating and current drive. Furthermore, if fast-ions are lost to the walls of the machine in a sufficiently intense and localized way, irreversible damage to plasma facing components can be provoked. Therefore, a deep understanding of the mechanisms leading to fast-ion transport and eventual losses is of paramount importance. The need to develop control tools to avoid these losses is now becoming a priority in the roadmap to future burning plasma experiments. In this sense, scintillator based fast-ion loss detectors (FILD) have been proven to be a powerful diagnostic to study the interaction between fast-ions and magnetohydrodynamic (MHD) instabilities, contributing to unravel the physics underlying the transport mechanisms.

In this thesis the study of fast-ion losses in the presence of various MHD instabilities in the ASDEX Upgrade tokamak is presented. A comprehensive description of scintillator based FILDs response is given here for the first time, with a special focus on its velocity-space resolution. As any other instrument in physics, the resolution of the system is finite, in this case due to the size of the detector pinhole and the gyrophase distribution of the measured ions. The detector response is described in terms of a simple model based on a weight function formalism. The model allows to calculate synthetic FILD signals given a velocity-space distribution of fast-ions reaching the detector pinhole. This enables a direct comparison between simulations and experimental measurements, taking into account the response of the instrument. Velocity-space tomography techniques have been implemented, which allow to obtain the undistorted velocity-space distribution of fast-ions reaching the detector pinhole. The tool improves the velocity-space resolution of FILD measurements, which can potentially reveal additional details in the velocity-space dynamics of fast-ion losses.

These improvements have been applied to the study of different MHD induced fast-ion losses. The first velocity-space resolved absolute measurement of fast-ion losses in the presence of a tearing mode in the ASDEX Upgrade tokamak is presented. An estimate of the different loss channels in absolute terms is given. These measurements, supported by simulations of fast-ion losses including the modelling of ICRF power deposition, suggest that MHD induced fast-ion losses are responsible for the anomalously large heat load measured by the FILD detector, which is then damaged irreversibly. This case represents a perfect example of the potential consequences derived from a bad confinement of the fast-ion population.

The velocity-space dynamics of fast-ion losses induced by edge localized modes (ELMs) are investigated. It is observed that, in low collisionallity discharges, a fast-ion population with energies well above the main neutral beam injection (NBI) - dubbed *high-energy feature* - is measured. The high-energy feature is correlated with the occurrence of ELMs. The pitch-angle structure of the high-energy feature is observed to change with the edge safety factor and the NBI source, which is found to be related with the topology of the orbits. The high-energy feature is also observed in mitigated ELM regimes, while not seen in ELM suppressed regimes. This observation is interpreted as the acceleration of beam ions during the ELM crash, when magnetic reconnection is believed to take place. A resonant interaction between the beam-ions and the parallel electric fields emerging during the ELM is proposed as a possible acceleration mechanism, and is observed to qualitatively agree with the main experimental results. The observation motivates a kinetic description of fast-ions in ELM models. Additionally, the finding might also be of interest to the astrophysics community, where acceleration of charged particles in plasmas is ubiquitous, in particular in solar flares, which show similarities with ELMs in tokamaks.

Acknowledgements

First of all I would like to thank my supervisors, Dr. Manuel Garcia-Munoz and Dr. Eleonora Viezzer, for introducing me to the field of fusion and giving me this opportunity. I am grateful for their priceless scientific orientation and the many enlightening physics discussions.

I would also like to acknowledge all the people which have contributed in some extent to this work: Dr. F.Ryter and Dr. P.Schneider for their advice; Dr. Igochine, Dr. Fietz and Dr.Maraschek, for their help with the MHD analysis; Dr. B.Sieglin for his contribution with thermography measurements; Dr. M.Nocente for his contribution with the modelling and many helpful discussions; D.Vezinet for his contribution with SXR tomography; Dr. G.Tardini for introducing me to the TRANSP code; Dr. F.Orain and M.Hoelzl, for the discussions about ELM physics and their support with the modelling; Dr. Mantsinen for her contribution with the modelling of ICRH power deposition with PION; Dr. Burckhart, W.Popken and S.Martinov, for supporting and helping many times both, with software and hardware issues; Dr. M.Salewski and Dr. A.Jacobsen for their help and support in the development of the velocity-space tomography applied to FILD measurements; Dr. Suttrop, Dr. Willensdorfer, Dr. Freethy and S.Denk, for their help with the interpretation of the ECE measurements; Dr. J.Garcia and Dr. M.C.Jimenez-Ramos for the helpful discussions about scintillator physics.

I would like to thank all the colleagues of the PSFT group for making it so easy to work with them and the great atmosphere: Javi, Juanfran and Juanma, the engineers of the group, for all the great evenings in Calle Feria (and many other places!); Patri, for making the paperwork so easy; the newer members of the group Pilar, Diego, Jesus, Jose and Pablo; and especially Mauri and Lucia, who have accompanied me since the very first minute.

I would also like to mention the colleagues from CNA and the Physics Faculty: Charles Alive, Charles Silver, Jorge, Mario, Mercedes and Migue, who also were there during the Master.

I would also like to thank all the colleagues at IPP: Sina, Steffen, Andreas, Mike, Athina, Philip, Sven, Asger, Anton, Gregor, ... and in general the whole AUG team, for hosting me so nicely during my stays! Thank you so much!

Agradecer también la ayuda inestimable a los amigos de siempre, porque desconectar también es necesario, especialmente a Serrano, Donner, Joaqui y demás *familiares*; y a Luna, Marina, Monti, Lourdes y Alberto, por las incontables tardes de Alameda y Salvador!

Por último, me gustaría agradecer a las personas más cercanas que han estado a mi lado estos años: a mis padres, por hacerlo posible; a Reyes, por su paciencia y el apoyo más incondicional y afectuoso; y a Manuel, por las innumerables y reveladoras conversaciones.

Contents

List of Figures

List of Tables

List of Abbreviations

AE	**A**lfvén **E**igenmode
AUG	**A**SDEX **Upg**rade
CCD	**C**harge **C**oupled **D**evice
CTS	**C**ollective **T**homson **S**cattering
CXRS	**C**harge Exchange **R**ecombination **S**pectroscopy
ECE	**E**lectron **C**yclotron **E**mission
ECRH	**E**lectron **C**yclotron **R**esonance **H**eating
ELM	**E**dge **L**ocalized **M**ode
EPM	**E**nergetic **P**article **M**ode
ETB	**E**dge **T**ransport **B**arrier
FIDA	**F**ast **I**on **D**-**A**lpha
FILD	**F**ast **I**on **L**oss **D**etector
FLR	**F**inite **L**armor **R**adius
HFS	**H**igh-**F**ield **S**ide
ICRF	**I**on **C**yclotron **R**esonance **F**requency
ICRH	**I**on **C**yclotron **R**esonance **H**eating
ICE	**I**on **C**yclotron **E**mission
IDA	**I**ntegrated **D**ata **A**nalysis
IR	**I**nfra**r**ed
MHD	**M**agneto**h**ydro**d**ynamics
MP	**M**agnetic **P**erturbation
NBI	**N**eutral **B**eam **I**njection
NPA	**N**eutral **P**article **A**nalyzer
LFS	**L**ow-**F**ield **S**ide
OH	**O**hmic **H**eating
PB	**P**eeling-**B**allooning
PFC	**P**lasma **F**acing **C**omponents
PMT	**P**hoto**m**ultiplier **T**ube
RES	**R**enewable **E**nergy **S**ources
RSAE	**R**eversed **S**hear **A**lfvén **E**igenmode
SNR	**S**ignal-to-**N**oise **R**atio
SOL	**S**crape-**o**ff **L**ayer
SXR	**S**oft **X**-**R**ay
TAE	**T**oroidicity induced **A**lfvén **E**igenmode
TF	**T**oroidal **F**ield
TM	**T**earing **M**ode
TS	**T**homson **S**cattering

List of Symbols

Cyclotron Frequency	$\omega_c = qB/m$
Energy	$E = mv^2/2$
Magnetic moment	$\mu = mv_\perp^2/2B$
Larmor radius	$r_L = mv_\perp/qB$
Pitch Angle	$\eta = cos\Lambda = v_\parallel/v$
Toroidal Canonical Angular Momentum	$P_\phi = mRv_\parallel + q\Psi$
Toroidal precession frequency	ω_d
Transit frequency	ω_b
Safety Factor	$q = \Delta\phi/2\pi$
Velocity-space distribution at the pinhole	$\Gamma_P(\rho_L, \Lambda)$
Velocity-space distribution at the scintillator	$\Gamma_S(\rho_L', \Lambda')$
FILD weight function	$w(\rho_L, \Lambda, \rho_L', \Lambda')$

"La naturaleza lo sabrá actuando, lo mismo que el observador observando, porque cada objeto físico es un foco de poder creativo."

Antonio Escohotado, *Caos y Orden*

Chapter 1

Introduction

1.1 Fusion as an alternative energy source

The quality-of-life of modern societies has reached unprecedented levels and this is commonly linked to the large (electrical) energy consumption per capita. The main energy sources that have made this possible since the last century are fossil fuels, nuclear fission and, only lately, renewable energy sources (RES) such as solar and wind. This is illustrated in Fig.1.1, where the evolution of the global contribution of different energy sources is depicted.

However, the sustainability of these resources is now in question and there is an increasing concern about the impact of these on the environment and its consequences. On the one hand, fossil fuels are a limited resource and expectations are that they will run out in few decades. The emission of gases, especially those contributing to the so called *greenhouse effect*, and their impact on the environment is a major drawback. On the other hand, although the fuel needed for nuclear fission power plants is also limited (on a longer timescale), the main concern with this resource is the handling of the long-lived radioactive waste which is produced. Furthermore, the risks inherent to the usage of radioactive sources should not be ignored and have had an impact on the public opinion, especially after the well-known accidents of Chernobyl in 1986 [1] and Fukushima in 2011 [2].

The current alternative to maintain the levels of electric power production are the renewable energy sources (RES), which are naturally unlimited and harmless for the environment. The main RES are solar (photovoltaic and concentration), wind (on- and off-shore) and hydroelectric, although the growing potential of the latter is limited due to the finite number of useful emplacements. However, the *intermittency* inherent to solar and wind RES, causes a fundamental problem of *dispatchability*, i.e: the energy is only produced when the resources are available and not when the demand requires it.

In this scenario nuclear fusion emerges as a promising alternative energy source to complement the classical RES. Nuclear fusion is based on a nuclear reaction in which two light nuclei (reactants) interact and produce a heavier nucleon, delivering a large amount of energy in the process determined by the difference in the binding energy of the nuclei involved. On Earth, the most convenient fusion reaction, due to its high cross-section at achievable temperatures [4], is:

$$ {}^{2}_{1}D + {}^{3}_{1}T \rightarrow {}^{4}_{2}He + n + 17.6MeV \tag{1.1} $$

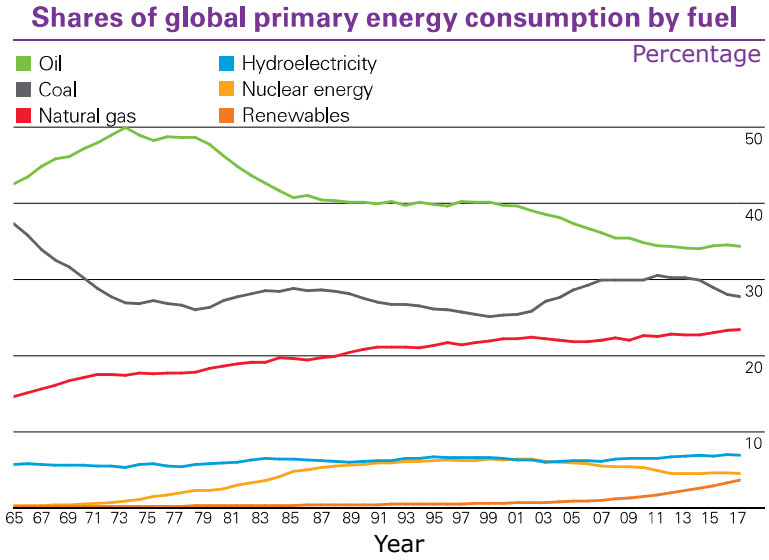

FIGURE 1.1: Evolution of global energy consumption by source. Figure adapted from [3]

In this reaction the reactants are two isotopes of hydrogen: deuterium (D) and tritium (T). The reaction produces an *alpha* particle and a neutron, delivering 17.6 MeV as kinetic energy of the products. It is therefore free of CO_2 (or any other greenhouse effect gas) and, opposite to nuclear fission, does not generate long-lived radioactive waste.[1]

Concerning the fuel, deuterium is naturally abundant on Earth and can be extracted from water, while tritium is a radioactive isotope with a half-life time of $\approx$ 12 years, and it is therefore not present in the environment. However, it can be produced through a nuclear reaction involving Lithium (Li) and could be directly *breeded* in the reactor:

$$n + {}^{6}_{3}Li \rightarrow {}^{4}_{2}He + {}^{3}_{1}T \tag{1.2}$$

From the scientific and technological point of view, achieving controlled nuclear fusion on Earth poses an extraordinary challenge. The nuclear fusion reactions can only take place at very high energies (maximum cross section for D-T reaction is at $\sim 10^2$ keV), in order to overcome the Coulomb repulsion between nuclei. At these high energies, the electrons are not bound to the nuclei and the matter reaches the fourth state, i.e: plasma, commonly defined as a *quasi-neutral ionized gas which exhibits collective behaviour*. In addition to this, there is also a purely scientific motivation related to side-band research in many different fields such as material science and plasma physics among others.

In order to make fusion profitable from the energetic point of view, the amount of usable energy released from fusion reactions should be larger than the amount of energy that we feed into the system in order to heat up the plasma. A common figure of merit that is used to characterize this is the fusion energy gain, which is defined as:

[1] The neutrons generated in the reaction will *activate* the materials of the installation. Estimations reveal a low radio toxicity level after 100 years [5].

$$Q = \frac{P_{fusion}}{P_{heating}} \tag{1.3}$$

where P_{fusion} is the power generated by fusion reactions and $P_{heating}$ is the input power needed to heat up and maintain the plasma. Only when $Q \geq 1$ we will start profiting from fusion. If a sufficiently good confinement is achieved, the energy provided by the α particle heating should be enough to maintain the temperature of the plasma. Under these conditions, the external heating power is not needed ($P_{heating} = 0$) and $Q \to \infty$. This is called *ignition*.

The conditions for the achievement of ignition can be conveniently expressed through the triple product [6]:

$$n \cdot T \cdot \tau_E > 5 \cdot 10^{21} m^{-3} keVs \tag{1.4}$$

where n is the plasma density, T is the plasma temperature [2], and τ_E is the energy confinement time. What this triple product states is that in order to enter the ignition regime, the plasma should have a high enough density, at a high enough temperature and should be confined during a sufficiently large period of time.

1.2 Tokamaks

Different paths have been (and continue to be) explored towards the achievement of controlled nuclear fusion on Earth. These can be categorized into two main groups: inertial confinement and magnetic confinement methods. From the technological point of view, probably the most advanced design up to date is the *tokamak*, which will be the focus for the remaining of this thesis. In the following a brief introduction to the tokamak concept will be given[3].

Tokamaks are based on the magnetic confinement of plasmas and characterized by a toroidal symmetry. The magnetic confinement of plasmas relies on the fact that charged particles are *bound* to magnetic field lines by means of the Lorentz force, which leads to helical trajectories of charged particles around these field lines. In a tokamak, the magnetic configuration is the result of the superposition of a toroidal magnetic field and a poloidal magnetic field. Fig.1.2 shows schematically the main elements of a tokamak. The toroidal magnetic field is generated by means of a limited number of toroidal field (TF) coils (in blue). A transformer coil in the center of the device (in magenta) induces a current I_p (in magenta) in the plasma (in yellow) in the toroidal direction. The plasma current generates a magnetic field in the poloidal direction which then leads to helical magnetic field lines, needed to assure the confinement of the particles[4]. Thus, as long as the plasma current is inductive, the tokamak by definition operates in a pulsed regime[5].

[2] In this work, following the convention in the field, temperatures are given in units of eV by means of the Boltzmann's constant: $T[eV] = k_B[eV/K] \cdot T[K]$

[3] For a detailed description of tokamaks see the textbook *Tokamaks*, J.Wesson [6]

[4] This will become clear in chapter 2, where particle drifts are explained.

[5] Intensive research efforts are made seeking for non-inductive scenarios in which the plasma current is driven by other means (e.g: using external heating systems) [7].

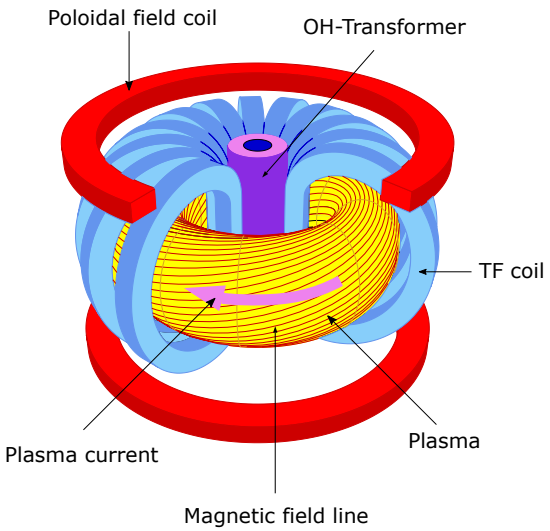

FIGURE 1.2: Sketch showing the basic elements of a tokamak. Figure adapted from the ASDEX Upgrade intranet (www.aug.ipp.mpg.de/wwwaug/)

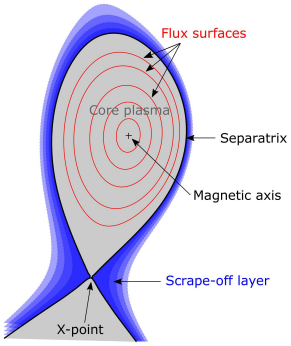

FIGURE 1.3: Poloidal plot of a tokamak magnetic equilibrium.

In tokamaks, the helicity of the magnetic field lines is described by the safety factor which is defined as:

$$q = \frac{\Delta\phi}{2\pi} \tag{1.5}$$

which can be understood as the change in the toroidal angle (ϕ) of the field line after one complete poloidal turn. The helical magnetic field lines lie on nested constant magnetic flux surfaces, to which charged particles are bound. This, together with the toroidal symmetry of the device which solves the problem of *end losses* unavoidable in linear devices, provides a good basis for the confinement of charged particles. Still, the confinement is not perfect and particles diffuse radially outwards towards the walls of the vessel due to Coulomb collisions and/or plasma instabilities.

An example of a typical divertor configuration is illustrated in Fig.1.3. The closed magnetic flux surfaces are shown in red. The last closed magnetic flux surface, called *separatrix*, is shown in black. The plasma is well confined in the shaded region. Outside the separatrix the magnetic field lines are not closed anymore. This region,

shown in blue, is called scrape-off layer (SOL).

In order to reach the temperature needed for fusion relevant conditions, different mechanisms are displayed. First, the toroidal current heats the plasma via Joule dissipation. The ohmic heating (OH) is however limited due to the fact that the plasma resistivity decreases with increasing temperature. Then, external heating sources need to be used. Amongst these, the most important ones are neutral beam injection (NBI), ion cyclotron resonance heating (ICRH) and electron cyclotron resonance heating (ECRH). NBI and ICRH systems rely on the generation of fast-ion populations which deposit their energy on the bulk plasma through Coulomb collisions, heating both ions and electrons. Finally, nuclear reactions produce high-energy ions which also contribute to the heating of the bulk plasma. Ultimately, the heating provided by fusion products should be enough to allow the self-sustained heating of the plasma. In the particular case of D-T reactions this is the so called *alpha particle heating*.

1.2.1 The role of fast-ions

Among the mechanisms described for the heating of the plasma, NBI, ICRH and α particle heating involve the presence of fast-ion populations in the plasma. A more detailed description on the NBI and ICRH systems will be given in 2. Although the border between thermal and fast-ions is not always sharp, the fast-ion population can be understood as that with energies $E >> E_{thermal}$ such that it deviates from the Maxwellian velocity distribution function expected for the bulk thermal plasma (in equilibrium).

As a consequence of their high energy, fast-ions exhibit some major differences with thermal ions:

- **Mean free path:** due to their higher energy, the collision frequency of fast-ions is smaller than that of thermal ions, leading to large values of the mean free path ($\geq$ 10 km). This allows to treat fast-ions as collisionless under some circumstances depending on the timescale of the phenomenon of interest.

- **Gyroradius:** the Larmor radius of an ion is given by:

$$r_L = \frac{m \cdot v_\perp}{Z \cdot e \cdot B} \tag{1.6}$$

  where m is the mass of the particle, $v_\perp$ is the velocity perpendicular to the magnetic field, Z is the atomic number, e is the electron charge and B is the magnetic field. Fast-ions have large gyroradii given their higher velocity. In some cases, this constitutes a limit to the guiding-centre approximation of the orbits. In a typical AUG plasma with on-axis magnetic field of 2.5 T, the thermal deuterium gyroradius ($T_i \sim 3$ keV) is of the order of $r_L \sim 0.45$ cm, while a fast-ion with $E \sim 90$ keV would have a gyroradius of $r_L \sim 2.45$ cm.

- **Drift orbits:** charged particle orbits are constrained to the magnetic flux surfaces within a distance which is proportional to the size of the poloidal gyroradius ($\rho_\theta = \frac{v_\phi}{\omega_{c\theta}}$). For thermal particles this implies that the orbits lie close to the magnetic flux surfaces, but fast-ion orbits can be shifted a non-negligible distance from the magnetic flux surface.

A good confinement of the fast-ion population is of great importance for several reasons [8]. First, in order to ensure the heating of the bulk plasma. Second, fast-ions provide a source of momentum which can be tailored to provide additional drive to the plasma current [9, 10]. Last but not least, fast-ion losses to the first wall of the vessel can be, if sufficiently intense and localized, a threat for the device integrity [11, 12].

Such a fast-ion transport and eventual losses can be provoked by different mechanisms [13] and have been experimentally observed in a wide range of machines worldwide, some of which are briefly described in the following:

- **Prompt losses:** these are due to fast-ion orbits which are born in non-confined orbits [14].
- **Charge exchange losses:** these are due to fast-ions in the plasma which undergo charge exchange reactions. They then become neutralized and are not confined by the magnetic fields anymore [15].
- **Coulomb collisions:** fast-ions deposit their energy in the bulk of the plasma through Coulomb collisions. At high energies, this process is dominated by collisions with thermal electrons, which effectively produce a drag force on fast-ions leading to their slowing down. Below a certain energy, collisions with thermal ions start to dominate and pitch-angle scattering process starts to play a role. Fast-ions are then subject to changes in their magnetic moment which can even lead to changes in their orbit topology. Increased losses may be caused through this mechanism.
- **Symmetry breaking 3D fields:** deviations from the axisymmetry of the magnetic configuration can occur in a tokamak. Some of these symmetry breaking 3D fields are inherent to the machine design such as error fields [16, 17] and toroidal field ripple [18], while others can be induced externally, such as edge localized mode control coils, also known as magnetic perturbation (MP) coils [15, 19–23].
- **MHD induced:** increased fast-ion transport and loss has been extensively reported due to different kind of magnetohydrodynamic (MHD) fluctuations such as: tearing modes (TMs) [20, 24–27]; fishbones [28–33]; a wide spectrum of Alfvén waves such as toroidicity induced Alfvén eigenmodes (TAEs) and reversed shear Alfvén eigenmodes (RSAEs) [34–46]; edge localized modes (ELMs) [19, 47]; and sawtooth crashes [48–53].

1.3 Motivation and scope of this thesis

The aim of this thesis is to gain a deeper insight into the interaction between fast-ions and MHD instabilities that can eventually lead to fast-ion losses. Understanding these transport mechanisms is key to develop control tools [54, 55] that can help to improve their confinement towards future burning plasma experiments such as ITER [56].

The work presented in this thesis focusses on the analysis of the experimental measurement of fast-ion losses with scintillator based fast-ion loss detectors (FILD)

in the ASDEX Upgrade (AUG) tokamak. In particular, the velocity space dependency of these losses can reveal valuable information about the underlying transport mechanisms. A comprehensive characterization of the response of scintillator based FILDs is performed for the first time. A model has been developed based on a weight function formalism. This improvement allows us to analyze FILD signals with unprecedented velocity-space resolution. The velocity-space of ICRH fast-ion losses in the presence of a tearing mode has been analyzed. The different loss channels have been estimated in absolute numbers for the first time, and the resonances responsible for the coherent losses are identified.

A detailed analysis of fast-ion losses induced by edge localized modes (ELMs) has been carried out. ELMs are MHD instabilities, located in the edge of fusion plasmas and inherent to the high-confinement regime (H-mode) [57]. They are thought to be driven by the steep pressure gradient and/or the plasma current and provoke the loss of confinement in the plasma edge in a cyclic fashion, flushing particles and energy to the first wall of the device [58, 59]. These transient heat-loads limit the lifetime of plasma facing components. Thus, a great effort is put on understanding the physics of ELMs in order to develop control mechanisms. The interaction between ELMs and fast-ions has not been extensively studied up to now. Although previous work had reported on the enhanced level of fast-ion losses during ELMs [19], no emphasis had been put into the velocity-space evolution of these, which has been found to reveal valuable information about the interaction between fast-ions and ELMs. An accelerated beam-ion population has been measured by means of FILD detectors during ELMs in AUG for the first time. A simple model which describes the phenomenon in terms of a resonant interaction is found to be consistent with the main experimental observations. The importance of a kinetic description of fast-particles in ELM models is highlighted.

This thesis is structured as follows: in Chapter 2 a brief theoretical background of fast-ions in tokamaks and MHD instabilities is given. In Chapter 3 the experimental setup at AUG is presented, focusing on the description of FILD detectors. In Chapter 4 a model which describes the response of scintillator-based FILD detectors is presented, together with the novel application of tomographic inversion techniques to FILD signal analysis. In Chapter 5 the experimental results are presented, which are divided into two parts. First, the velocity-space resolved absolute measurement of ICRH fast-ion losses in the presence of a tearing mode is presented. Then, the experimental measurement of fast-ion losses due to ELMs is shown, with emphasis on the observation of beam-ion acceleration. Finally, in Chapter 6 the main results of the thesis are summarized and discussed.

Chapter 2

Theoretical Background

In this chapter the physics principles which are imperative for the development of this work are described[1]. First the trajectories of charged particle in the presence of magnetic fields and the sources of fast-ions in tokamak plasmas are introduced. Then, upon the vast zoo of MHD instabilities that can be found in tokamak plasmas, we briefly describe only those that are relevant to this work. These are internal kink and tearing modes in the plasma core, and edge localized modes at the plasma edge. Finally, a flavour of the theory underlying to the resonant transport of fast-ions will be given.

2.1 Fast-ions in tokamaks

2.1.1 Single particle motion: drifts and orbits

The motion of charged particles will be described here in the single particle framework[2], this is, we neglect the interaction between particles and only consider their behaviour in the presence of preset magnetic, and eventually, electric fields.

We will first start with the most simple case, this is, the motion of charged particles in the presence of a constant magnetic field. This is governed by the Lorentz equation of motion:

$$m\frac{d\vec{v}}{dt} = q\vec{v} \times \vec{B} \tag{2.1}$$

where m and q are the particle mass and charge respectively, $\vec{v}$ is the particle velocity and $\vec{B}$ is the magnetic field. This equation can be decomposed into its parallel and perpendicular components with respect to the magnetic field:

$$m\frac{dv_{\parallel}}{dt} = 0 \tag{2.2}$$

$$m\frac{d\vec{v_{\perp}}}{dt} = q\vec{v_{\perp}} \times \vec{B} \tag{2.3}$$

From the first equation it can be concluded that the velocity in the direction parallel to the magnetic field remains constant, while the motion in the perpendicular plane is described by a simple harmonic oscillator which leads to a circular trajectory. Adding up these two components it is seen that the trajectory of the particle is a helix around the magnetic field lines. The axis of this helix is usually called *guiding*

[1] For an exhaustive description of the behaviour of fast-ions in tokamak plasmas the reader is referred to the review by Heidbrink and Sadler [13], while for the description of MHD instabilities the reader is referred to the textbook by J.P.Freidberg [60] and H.Zohm [61]

[2] For a more rigorous derivation of these equations the reader is referred to [62, 63]

centre. Thus, the particle is bounded to the magnetic field line. The radius of the circular motion of the helix, the so-called *Larmor radius* or *gyroradius* is given by:

$$r_L = \frac{mv_\perp}{|q|B} \tag{2.4}$$

while the frequency of gyration or *cyclotron frequency* is given by:

$$\omega_c = \frac{|q|B}{m} \tag{2.5}$$

Since the circular motion in the plane perpendicular to $\vec{B}$ is cyclic, it is sometimes convenient to decompose the particle position as the guiding center position $\vec{R}$ plus the rotating gyroradius vector $\vec{\rho}$:

$$\vec{r} = \vec{R} + \vec{\rho} \tag{2.6}$$

where $\vec{\rho} = \rho \cdot (\cos\xi \cdot \vec{u_{\perp 1}} + \sin\xi \cdot \vec{u_{\perp 2}})$, where $\vec{u_{\perp 1}}$ and $\vec{u_{\perp 2}}$ are unitary vectors perpendicular to the magnetic field direction, and ξ is the gyroangle.

In the presence of additional forces the motion of the particle guiding center is subject to drifts which, in general, can be expressed using the following equation [64]:

$$\vec{v} = \frac{1}{q}\frac{\vec{F} \times \vec{B}}{B^2} \tag{2.7}$$

The particle will experience a drift in the direction perpendicular to both the force direction and the local magnetic field direction.

$\mathbf{E} \times \mathbf{B}$ drift

If an electric field, in addition to the magnetic field, is present, the charged particle will then experience a force $\vec{F} = q\vec{E}$, and following Eq.2.7 it will lead to the so-called *E-cross-B drift*:

$$\vec{v} = \frac{\vec{E} \times \vec{B}}{B^2} \tag{2.8}$$

The electric field component perpendicular to the magnetic field increases the particle's Larmor radius during half of the period of its gyromotion, and it decreases it in the other half. The oscillation of the effective particle's gyroradius leads to the drift. It is worth mentioning that this drift is independent of the charge of the particle, i.e: the drift is in the same direction for ions and electrons, and therefore it will lead to net plasma flows.

∇B drift

Consider the case of a particle in the presence of inhomogeneous magnetic fields. First consider the case in which the magnetic field intensity changes along a certain direction. This means that there is a magnetic field gradient $\nabla B \neq 0$. From a heuristic point of view, it can be first noticed that the particle's gyroradius will be smaller when it explores the region of higher magnetic field than when it explores

the region of lower magnetic field. Similar to the E-cross-B drift, this oscillatory behaviour of the particle's gyroradius will also lead to a drift, which in this case will be perpendicular to the local magnetic field and to the direction of the gradient.

To evaluate this drift we consider the averaged effect of the magnetic field gradient ∇B on the current associated to the particle gyromotion $I = \frac{q\omega_c}{2\pi}$. In the presence of a magnetic field gradient, the force acting on a magnetic dipole can be expressed as:

$$\vec{F} = \mu \nabla B \tag{2.9}$$

where μ is the magnetic moment. Here, the magnetic moment can be defined as the product of the current associated to the particle gyromotion times the enclosed area:

$$\mu = I \cdot A = \frac{q\omega_c}{2\pi} \pi r_L^2 = \frac{m v_\perp^2}{2B} \tag{2.10}$$

Thus, putting Eq.2.9 into Eq.2.7:

$$v_{\vec{\nabla} B} = \frac{m v_\perp^2}{2q} \frac{\vec{B} \times \nabla B}{B^3} \tag{2.11}$$

As we noticed previously, the so-called *gradB drift*, is perpendicular to the direction of the magnetic field gradient and the local magnetic field. In this case there is an explicit dependence with the charge sign q. Thus, the direction of the drift will be different for ions and electrons. In practice, this can lead to a charge separation which can create electric fields.

Curvature drift

Consider the case in which the magnetic field lines are curved with a constant radius R_c. As the charged particles follow the magnetic field lines, they are subject to the centrifugal force owing to the curvature of the field lines:

$$\vec{F} = m v_\parallel^2 \frac{\vec{R}_c}{R_c^2} \tag{2.12}$$

Again, recalling Eq.2.7 we obtain the following expression for the particle drift:

$$\vec{v_c} = \frac{m v_\parallel^2}{qB^2} \frac{\vec{R}_c \times \vec{B}}{R_c^2} \tag{2.13}$$

where the vector $\vec{R}_c$ points from the center of the radius of curvature towards the outside. This is the so called *curvature drift*, and again shows an explicit dependency with the charge of the particle.

In practice, in order to fulfill Maxwell equations, a curved magnetic field will always appear together with the gradient of the magnetic field. Therefore, both ∇B and curvature drifts will also appear together. Consider the case of a toroidal magnetic field which fulfills the Maxwell equations. Then, a relation between the radius of curvature of the magnetic field and its gradient can be obtained [64]:

$$\frac{\vec{R}_c}{R_c^2} = -\frac{\nabla B}{B} \tag{2.14}$$

Here $\vec{R}_c$ points outside the center of curvature while ∇B points in the opposite direction. Therefore, putting together Eqs. 2.11 and 2.13:

$$\vec{v_c} + v_{\vec{\nabla} B} = \frac{m}{q}(v_{\parallel}^2 + \frac{1}{2}v_{\perp}^2)\frac{\vec{R_c} \times \vec{B}}{R_c^2 B^2} \tag{2.15}$$

This simple picture mimics the case of a tokamak without its poloidal magnetic field component. In such a case ∇B points towards the center of the torus. Then, following Eq.2.15 ions and electrons would drift vertically but in opposite direction, leading to a charge separation and giving rise to an electric field in the vertical direction. The resulting E-cross-B drift would push the plasma towards the walls of the device resulting in the loss of the confinement. This is the reason why a *poloidal* component is needed in magnetically confined fusion devices with toroidal symmetry.

Magnetic mirror

In order to understand particle orbits in tokamaks, the concept of magnetic mirror has to be introduced, which relies on the conservation of energy and the invariance of the magnetic moment μ under adiabaticity conditions [64], meaning that the spatial and temporal variation of the magnetic field are slow compared to the gyromotion of the particles, i.e: $\frac{B}{|\nabla B|} >> r_L$ and $\frac{\dot{B}}{B} << \omega_c$.

Consider a non-uniform magnetic field which exhibits regions of low and high magnetic field strength, and where the conditions of adiabaticity are fulfilled. As a result of the conservation of the magnetic moment $\mu = \frac{mv_{\perp}^2}{2B}$, when the particle moves from a region of low magnetic field to a region of high magnetic field, the perpendicular component of the velocity $v_{\perp}$ should increase accordingly. In the absence of external forces, the energy $E = \frac{1}{2}m(v_{\parallel}^2 + v_{\perp}^2)$ is conserved, and therefore, if $v_{\perp}$ increases $v_{\parallel}$ should decrease. If the magnetic field is strong enough, $v_{\parallel}$ will eventually decrease down to 0, and is then reversed back towards the region of low magnetic field, i.e: the particle is reflected from the region with high magnetic field towards the region of low magnetic field. The point in which $v_{\parallel} = 0$ is called *turning point* or *bounce point*.

The conditions for the bounce to happen can be easily derived from the invariance of the magnetic moment and depend on the initial conditions of the particle: $\mu_{initial} = \mu_{bounce}$. This leads to the following formula:

$$\frac{B_b}{B_i} = \frac{v_{\perp b}^2}{v_{\perp i}^2} = 1 + (\frac{v_{\parallel i}}{v_{\perp i}})^2 \tag{2.16}$$

where the subindices b and i stand for *bounce* and *initial*, respectively. At this point, it is useful to introduce the definition of *pitch angle*, which is the angle between the magnetic field and the velocity vectors. It can be expressed as[3]:

$$\eta = \cos\Lambda = \frac{v_{\parallel}}{v} \tag{2.17}$$

Using this definition, Eq.2.16 can be alternatively expressed as:

[3]The notation in the literature is ambiguous, calling indistinctly pitch angle to both Λ and $\cos\Lambda$

$$\frac{B_b}{B_i} = \frac{1}{1-\eta^2} \tag{2.18}$$

In a system with a maximum magnetic field B_{max}, the particle will be trapped in the low field side by the magnetic mirror if its initial parallel velocity $v_{\|}$ is low enough such that the condition $B_{max} > \frac{B_i}{1-\eta^2}$ is hold, i.e: $v_{\|} < v \cdot \sqrt{1 - B_i/B_{max}}$.

Particle orbits

A tokamak presents a magnetic configuration which is compatible with the existence of magnetic trapping. This is because there is a magnetic field gradient: due to the toroidal magnetic field variation as $1/R$, there is a high magnetic field region, or high-field side (HFS), close to the axis of the torus, and a low-field side (LFS) in the outer part of the torus. Owing to this criterion two main types of orbits can be found in a tokamak[4]: those that are reflected by the magnetic mirror at the HFS, or *trapped orbits*, and those which are not, or *passing orbits*.

An example of these two types of orbits is illustrated in Fig.2.1, which represents the projection of the orbits into the poloidal plane of AUG. These orbits correspond to deuterium ions started at the outer midplane, in the LFS, with an energy of 90 keV and pitch angle of $\Lambda = 45^o$ (in blue) and $\Lambda = 60^o$ (in red), corresponding to a passing and a trapped particle respectively. Trapped orbits are often called *banana orbits* too. The direction of the toroidal magnetic field and the plasma current is indicated in the upper left corner of the figure by a circle and a cross representing the ends of an arrow, meaning that the vector points from the plane of the paper towards the reader (circle) or viceversa (cross).

Fast-ion drift orbits

Figure 2.1 also reveals additional information about the orbit behaviour. It can be observed that the guiding center of the orbits is in fact not laying on a constant flux surface, but is rather oscillating around a central one. This is the so called *drift orbit* behaviour which defines the *orbit width*. This can be understood from the drift picture: the grad-B drift is continuously pushing the particle in the vertical direction (indicated in grey in Fig.2.1), displacing it through different flux surfaces. But since the magnetic field lines are twisted, the overall displacement is compensated and the orbit is closed. The effect is most clearly seen close to the banana tips, where $v_{\|} = 0$.

The magenta circle indicates the direction in which the orbits are closed in the poloidal plane, which is determined by the direction of the grad-B drift. This is an important fact to take into account for neutral beam injection. For example, in this configuration of B_t-I_p, the standard in AUG, ions in the outer banana leg are going in the co-current direction, while ions in the inner banana leg are going in the counter-current direction. If the NBI injects neutrals in the co-current direction, then the ions will be born in their outer banana leg. Along their orbit they will drift towards inner flux surfaces and will therefore be confined. However, if the injection is counter-current, then the ions will be born in their inner banana leg. Then, the ions

[4] Attending to their topological properties there is a wider variety of orbit types in tokamaks. Here we just present the two principal ones. For a more comprehensive description the reader is referred to [65, 66].

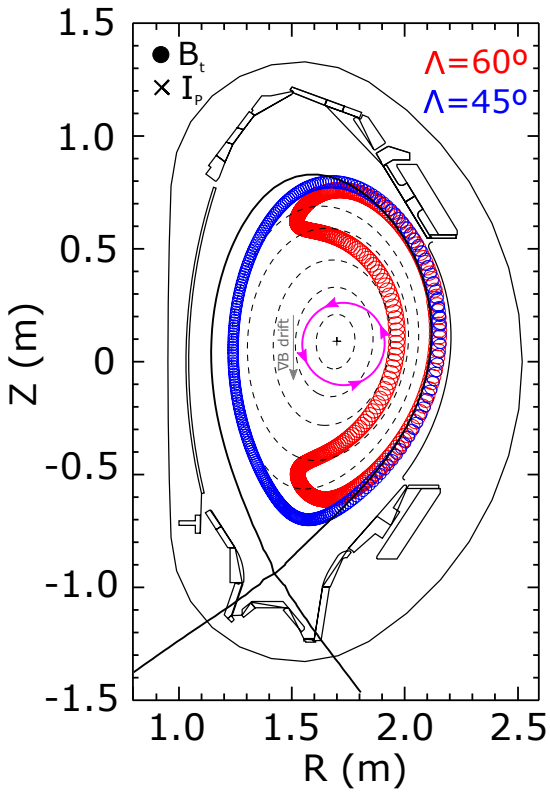

FIGURE 2.1: Poloidal representation of fast-ion orbits in AUG. In blue, a passing particle with pitch angle $\Lambda = 45^o$. In red, a trapped particle with pitch angle $\Lambda = 60^o$. Both orbits correspond to deuterium ions at 90 keV. The separatrix is indicated by the solid black line, while inner flux surfaces are represented by dotted black lines. The magnetic axis is indicated by the black cross at the center. The direction of the toroidal magnetic field and the plasma current is indicated in the upper left corner. In grey, the direction of the grad-B drift is also shown.

will be drifting towards outer flux surfaces, and therefore those ions that are born close to the plasma edge will likely be unconfined.

Alternatively, the displacement from the mean flux surface can be calculated from the conservation of toroidal canonical angular momentum. In an axisymmetric system, the toroidal canonical angular momentum is an invariant of motion [62]:

$$P_\phi = mRv_\phi + q\Psi \tag{2.19}$$

where m is the particle mass, R is the major radius, v_ϕ is the toroidal component of the particle velocity, q is the charge of the particle and Ψ is the poloidal magnetic flux. Along its orbit, as the particle moves towards lower values of R, due to the conservation of μ its parallel velocity $v_\parallel$ - and hence v_ϕ - decreases. Since P_ϕ is conserved, Ψ must increase, which means that the particle is drifting across different magnetic flux surfaces, in this case towards inner flux surfaces.

An estimation of the orbit displacement with respect to the mean flux surface can be obtained as follows:

$$e \cdot \delta\Psi = m \cdot \delta(Rv_\phi) \tag{2.20}$$

For a small displacement from the flux surface the change in the flux function can be expressed as $|\delta\Psi| = |\nabla\Psi| \cdot d$, where d is the displacement from the flux surface. An upper limit can then be estimated for this displacement [6]:

$$d \leq \left| \frac{v_\phi}{\omega_{c\theta}} \right| \tag{2.21}$$

where $\omega_{c\theta} = \frac{eB_\theta}{m}$. The displacement scales with the particle velocity v_ϕ. This effect is more important for the orbits of the fast-ions, since the faster the particle is, the larger the excursion from the mean flux surface will be, and therefore the wider the orbit will be. This also leads to the fact that there can actually be fast-ions outside the separatrix in the LFS which, due to their large drift orbits, are still well confined, as illustrated in Fig.2.1.

2.1.2 Sources

In tokamak plasmas fast-ions can be created by external heating systems such as neutral beam injection (NBI) or ion cyclotron resonance heating (ICRH), but also by fusion reactions in the plasma.

Neutral Beam Injection

The generation of fast-ions by means of NBI systems is first described here. In this system particles are first accelerated to high energies and then neutralized before being injected into the plasma. The need to neutralize the particles is to avoid deflections due to the magnetic fields. As the beam starts to penetrate the plasma, the neutral particles are ionized by means of different reactions such as electron and ion impact ionization or charge exchange processes.

Due to the charge state of the particles during their acceleration process, two different kind of NBI systems are found: the negative (N) and positive (P) NBI systems.

The first corresponds to systems in which the particles have negative charge during the acceleration process, while the second corresponds to systems in which the particles have positive charge. In the latter case, it happens that molecular species are also formed during the process. This leads to a certain population of ions with half or third fraction of the main injection energy after the neutralization process.

Once ionized, these fast-ions will transfer their energy to the bulk plasma by means of Coulomb collisions. At higher energies the collisions with electrons dominate leading to the slowing down of the distribution. At lower energies, the collisions with ions become relevant, which leads to additional pitch-angle scattering processes. There is an energy, the so-called *critical energy*, at which the NBI heating rate is equal for ions and electrons [6]:

$$E_c = \left(\frac{3\sqrt{\pi}}{4}\right)^{2/3} \left(\frac{m_i}{m_e}\right)^{1/3} \frac{m_b}{m_i} T_e = 14.8 \frac{A_b}{A_i^{2/3}} T_e \tag{2.22}$$

where the subscript b refers to the injected beam, the subscript i refers to the ions species in the plasma, and T_e is the electron temperature. In ASDEX Upgrade, where the NBI systems have a main NBI injection energy of 93 keV and 60 keV approximately, the critical energy is of the order of $\sim$56 keV.

The total heating fraction of bulk ions (and electrons correspondingly) can also be calculated as a function of the critical energy. It is observed that if $E_{inj} >> E_c$, a larger fraction of the power is transferred to electrons, and in the opposite case a larger fraction of the power is transferred to ions.

The slowing down time of the beam ions can be calculated by taking into account the power deposition into both ions and electrons. The following expression is obtained:

$$\tau = \frac{\tau_s}{3} \ln\left(1 + \left(\frac{E_{b0}}{E_c}\right)^{3/2}\right) \tag{2.23}$$

where

$$\tau_s = \frac{3\sqrt{(2\pi)} T_e^{3/2}}{\sqrt{(m_e)} m_b A_D} \tag{2.24}$$

$$A_D = \frac{n e^4 ln\Lambda}{2\pi\epsilon_0^2 m_b^2} \tag{2.25}$$

Taking typical parameters for AUG plasmas ($T_e = 3$ keV, $n_e = 5 \cdot 10^{19}\ m^{-3}$) we find that typical slowing down times for NBI ions of 90 keV are of the order of $\sim$90 ms [5].

The NBI birth distribution function (and the topology of these fast-ion orbits) is determined by the injection geometry of the beam and the magnetic equilibrium configuration. In general, an injection geometry which is *tangential* to the magnetic field lines will create larger populations of passing ions, while in the case of *perpendicular* injection a larger fraction of trapped particles in the LFS will be created. Not

[5] Typical energy confinement times in nowadays tokamaks are $\tau_e \leq 1$s [67]

only the orbit topology of the generated distribution is important, but also the spatial location. Then, it is possible to distinguish between *on-axis* and *off-axis* injection meaning that the deposition is located close to or far from the magnetic axis, and hence the plasma core.

For these reasons, i.e: the highly localized deposition of NBI ions in phase-space, the NBI distribution functions are typically very anisotropic. An example of NBI slowing down distributions is shown in Fig.2.2. These distributions have been calculated with the code TRANSP[6] [68], for a case with on-axis (a,b) and off-axis (c,d) beam injection at AUG. In this figure we can see how the spatial distribution varies depending on the NBI geometry. In the case of on-axis NBI (a) the distribution function peaks at the plasma core. In the case of off-axis NBI (c), the distribution function has its maximum displaced from the plasma core. This is an important fact to take into account since it is well known that gradients in the fast-ion distribution function can drive instabilities. If we now take a look at the volume averaged velocity space distribution for the case of on-axis NBI (b) we can see that there are several peaks at energies of approximately 90, 45, 30 and 20 keV, highlighted by black arrows. These correspond to the main, half and third energy components of the NBI. In this case two different NBI sources with main injection energies of 90 and 60 keV were simulated. These peaks are all centered at a pitch angle close to 0.5, which again is determined by the injection geometry. It can also be noticed that for energies above the critical energy, which is around 60 keV and indicated by a dashed grey line, there is almost no dispersion in pitch angle, while for energies below the critical energy, the pitch angle scattering processes take place and the dispersion in pitch angle of the distribution is increased. In the case of the off-axis NBI (d), the same features can be observed, although the dominant pitch angle of the distribution is shifted due to the different injection geometry. In this case two NBI sources, both with a main injection energy of 90 keV, were simulated.

Ion Cyclotron Resonance Heating

The ICRH mechanism relies on the capability of ions to gain energy via cyclotron resonance with an electromagnetic wave which is excited in the plasma by means of external antennae. For an ion to be able to gain energy, the following resonance condition must be fulfilled:

$$\omega - k_{\parallel} v_{\parallel} - n\omega_{ci} = 0 \tag{2.26}$$

where ω is the frequency of the wave, $k_{\parallel}$ is the wavenumber parallel to the magnetic field, $v_{\parallel}$ is the velocity component of the particle parallel to the magnetic field, ω_{ci} is the ion cyclotron frequency and n is an integer which corresponds to the different harmonics.

The dominant component of the magnetic field in a tokamak is the toroidal, which varies as 1/R. This defines the radial position at which the resonance condition can be fulfilled. Therefore, by tuning the frequency of the applied wave the resonance position in the plasma can be changed. The width of this resonance position or *layer* is subject to Doppler broadening due to the finite velocity of the particles

[6] TRANSP is a tokamak transport code widely used in the community. For more information visit: https://w3.pppl.gov/~pshare/help/transp.htm

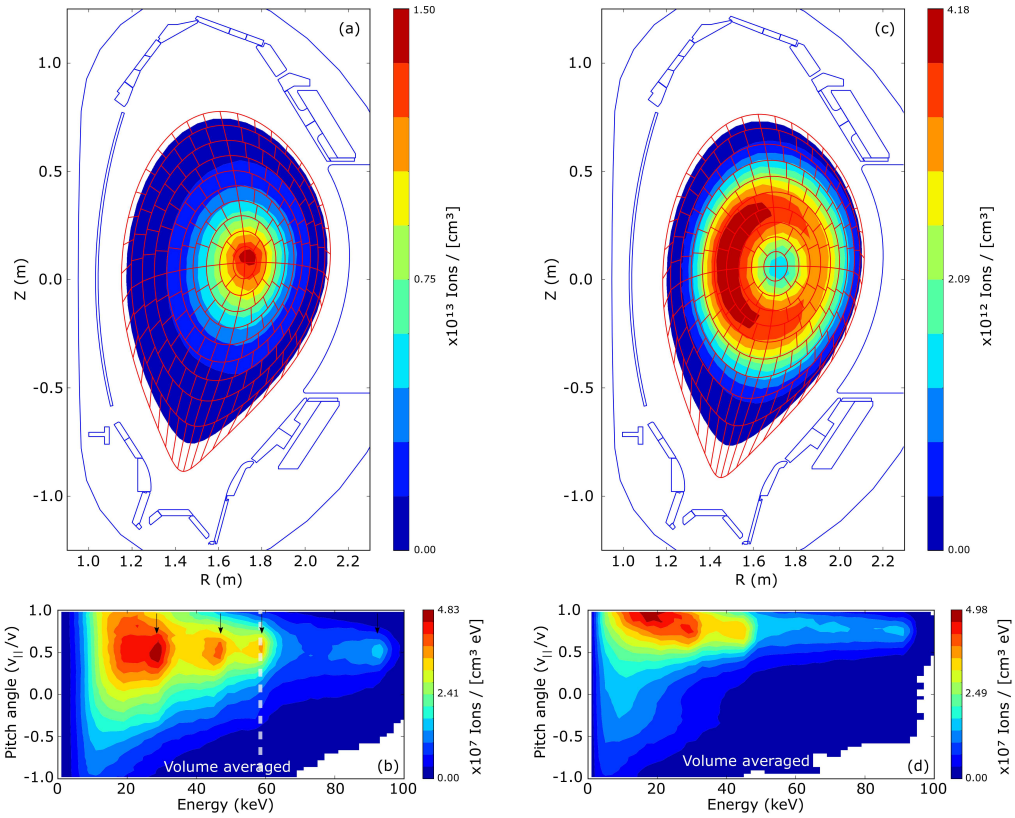

FIGURE 2.2: Simulated NBI distribution functions with TRANSP. (a) shows the projection of the distribution function in the poloidal plane, while (b) shows the volume averaged velocity space of the distribution, both for a case corresponding to on-axis NBI. (c) and (d) are the same for a case of off-axis NBI.

that interact with the wave.

The way ions are able to gain energy from the wave is schematically explained in the following: during its orbit, an ion will go through the resonance layer repeatedly. At each pass through the resonance layer, the ion will gain or lose energy depending on the relative phase between its gyromotion and the phase of the electric field of the wave. This process can be thought of as a *random walk* of the particle in velocity space, which corresponds to a diffusion in velocity space. Thus, opposite to the NBI birth distributions, ICRH fast-ion distributions need a certain time to fully develop. However, much higher energies are achievable with this system (up to the MeV range) [69].

Given a certain species in the plasma, by selecting the frequency of the applied wave we are choosing the harmonic that fulfills the resonant condition given by Eq.2.26. In principle, in the limit of small Larmor radius $k_\perp r_L \to 0$, only absorption of the left-circular polarized wave E_+ at the fundamental harmonic (n=1) is possible. Higher harmonics absorption is possible only if we consider *finite Larmor radius (FLR)* effects, which are applicable for the case of fast-ions (or at least a *hot* enough plasma). However, the polarization of the wave in the vicinity of the resonance is determined by the interaction between the wave and the plasma, i.e: it evolves as the wave propagates through the plasma. It is found that in a pure plasma this polarization at the resonance layer is unfavourable for the fundamental harmonic [70].

A common solution to this issue is to apply the so called *minority heating scheme* [71]. In this scheme, a second species with different A/Z ratio and with low concentration must be present in the plasma (which is usually the case in deuterium plasmas which contain some amount of residual hydrogen). The frequency of the wave is tuned to the fundamental harmonic frequency of the minority species, and in this case the favourable polarization of the wave can be obtained since this is determined by the bulk plasma species. Additional heating schemes in multi-ion plasmas are also of interest [72].

Fusion reactions

The last source of fast-ions that is described here are fusion reactions. As already mentioned in Chapter 1, fusion reactions deliver a great amount of energy which is shared by the products of the reaction, where there is always an ion. Although the foreseen reaction for a future fusion power plant is the D-T reaction described in Eq.1.1, the daily operation of present day tokamaks is done with deuterium (or hydrogen) plasmas, without tritium[7]. Therefore, the main nuclear reactions that can be found in a deuterium plasma are:

$$D + D \to^3 He + n + 3.27MeV \tag{2.27}$$

$$D + D \to T + p + 4.03MeV \tag{2.28}$$

The reaction rates can be evaluated through the density and velocity distribution of the reactants and taking into account the cross-section of the process:

[7] Tritium is radioactive, which limits the access to the machine for safety reasons, and this is usually needed during experiments (e.g: changing the setups of diagnostics)

$$R = \int_{Vol} \frac{1}{1+\delta_{ij}} n_i n_j < \sigma v > d\vec{r} \tag{2.29}$$

where n_i and n_j are the reactants densities, $< \sigma v >$ is the reactivity, and the factor $\frac{1}{1+\delta_{ij}}$ is included to avoid the double counting of the reactants in the case that these are from the same population, i.e: $i = j$.

The reactivity is evaluated in general as:

$$< \sigma v >= \int f(\vec{v}_i) \cdot f(\vec{v}_j) \cdot \sigma_{ij}(\vec{v}_i - \vec{v}_j) \cdot |\vec{v}_i - \vec{v}_j| d\vec{v}_i d\vec{v}_j \tag{2.30}$$

The fusion reactions mentioned in Eq.2.28 can come from three different channels:

- **Thermonuclear reactions:** those that happen between elements of the bulk plasma ion distribution.
- **Beam-target reactions:** those that happen between ions from the NBI systems (beam) and ions from the bulk plasma (target).
- **Beam-beam reactions:** those that happen between ions generated by the NBI system.

The birth profile distribution of fusion products generated from thermonuclear reactions will depend on the kinetic profiles of the plasma (n_e and T_e), while in the case of the other two, the spatial distribution of the fast-ion distribution generated by means of the external heating systems need to be considered. This is illustrated in Fig.2.3, where the beam-target neutron emmissivity profile is shown for the two cases discussed before, corresponding to an on-axis (Fig.2.3 (a)) and off-axis (Fig.2.3 (a)) beam injection.

2.2 Plasma instabilities

In general, the stability of a system can be understood as its capability of returning to equilibrium whenever a perturbation is applied. If under the application of a perturbation the system is not able to get back to the equilibrium, the system is called *unstable*. In the case of a fusion plasma, a general way of looking at the ideal MHD stability is through the variational energy principle. In its *intuitive* form it can be expressed as [61]:

$$\delta W_F = \frac{1}{2} \int \Big[\frac{|B_{1\perp}|^2}{2\mu_o} + \frac{B_{0\perp}^2}{2\mu_o} |\nabla \cdot \xi_\perp + 2\xi_\perp \cdot \vec{\kappa}| + \gamma p_0 |\nabla \cdot \xi|^2 - 2(\xi_\perp \cdot \nabla p_0)(\vec{\kappa} \cdot \xi_\perp^*) - \frac{j_{0\parallel}}{B_0} (\xi_\perp^* \times B_0) \cdot B_1 \Big] dV \tag{2.31}$$

If $\delta W > 0$ the system is stable, while if $\delta W < 0$ the system is unstable. Therefore, the positive terms are stabilizing terms while negative terms are destabilizing. The first term is the magnetic field energy associated to the perturbation. The second term is related to the compression of the magnetic field and plasma. The third term is related to the adiabatic compression of the plasma. These three terms are always positive and hence stabilizing. The other two terms can be either positive or

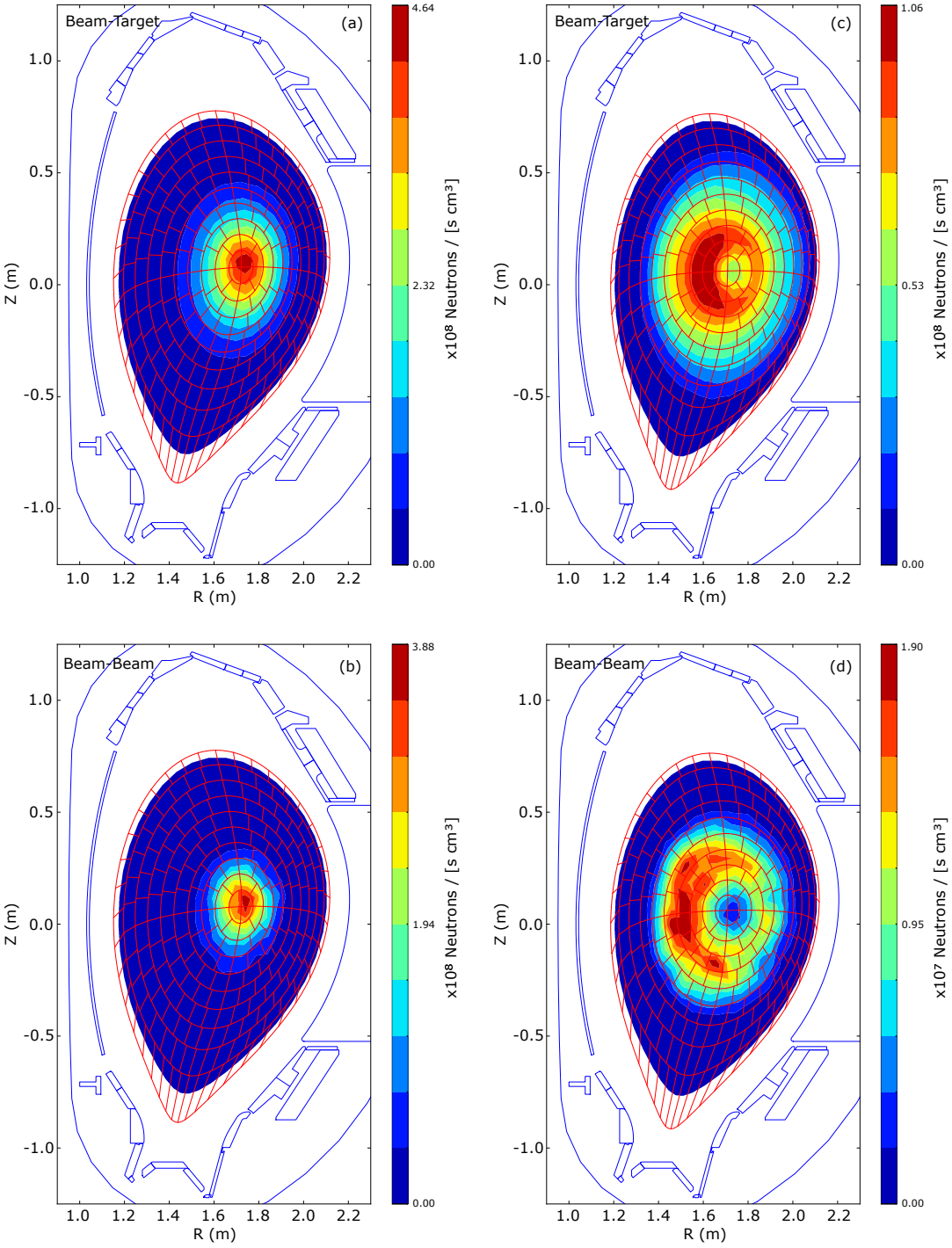

FIGURE 2.3: Neutron emission calculated by TRANSP corresponding to the beam-target (a and c) and beam-beam components(b and d). (a) and (b) correspond to a case with on-axis NBI, while (c) and (d) correspond to a case with off-axis NBI.

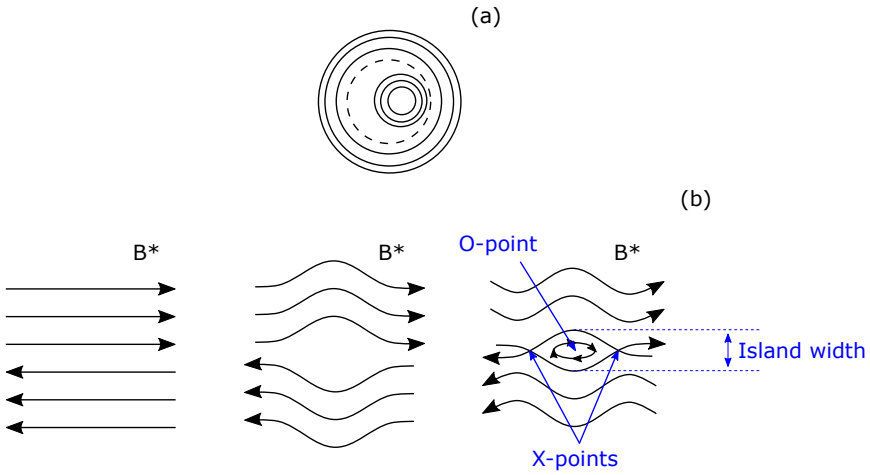

FIGURE 2.4: (a) Sketch of a kink mode, showing how magnetic field lines are displaced. (b) Sketch showing the formation of a magnetic island.

negative, and are therefore the source of instabilities. The fourth term refers to the destabilizing contribution of pressure gradients. Depending on the relative orientation of ∇p and κ the term will be positive or negative. The two possible situations - parallel or antiparallel- are often referred to as *good* and *bad* curvature of the magnetic field. The last term describes the contribution of the current density parallel to the magnetic field to the instability.

Owing to Eq.2.31, a vast zoo of MHD instabilities can be found in a tokamak. In the following we briefly describe only three of them.

2.2.1 Kink and tearing modes

Kink modes are ideal MHD instabilities characterized by a displacement or shift of the magnetic flux surfaces, as illustrated in Fig.2.4 (a). They are current-driven instabilities and, in general, they can be divided into external kink modes - if there is a displacement of the plasma boundary - and internal kink modes - if only internal magnetic flux surfaces are affected while the plasma boundary is not. Being ideal MHD instabilities, the magnetic topology of the tokamak is not altered by kink modes.

Tearing modes are resistive MHD instabilities which lead to a change in the magnetic topology of the system. They are characterized by the formation of magnetic islands in regions of magnetic fields with opposing direction, involving magnetic reconnection processes. The center of the magnetic island is called O point, while the point in which magnetic field lines cross is called X point. The width or size of the island is defined as the maximum radial distance between the two ends of the island separatrix. This is illustrated in Fig.2.4 (b).

In a tokamak, tearing modes connect different radial regions of the plasma along the magnetic field lines, thus breaking the structure of constant flux magnetic surfaces lying inside each other. Since the particle transport along field lines is very fast, tearing modes have a deleterious impact on the particle confinement. Experimentally, this is usually observed through the local flattening of density and temperature

profiles at the resonance location.

In a tokamak, the spatial structure of any 3D instability is generally defined by the toroidal (n) and poloidal (m) mode numbers. Kink and tearing modes can develop at magnetic surfaces characterized by rational values of the safety factor $q = \frac{m}{n}$, which is usually referred to as *rational surface*.

An important difference between kink and tearing modes is the typical timescale involved in the growth rate of the instability. Kink modes follow ideal MHD timescales - $\tau_{Alfven} \propto \frac{L}{v_A} \sim 10\ \mu s$, where L is the size of the system and v_A is the Alfvén velocity - while tearing modes follow resistive MHD timescales - $\tau_{res} = \frac{L^2}{D_{mag}} \sim 10\ ms$, where $D_{mag} = \frac{1}{\mu_0 \sigma}$ being μ_0 the magnetic permeability of vacuum and σ the electrical conductivity.

2.2.2 Edge localized modes

Edge localized modes are plasma instabilities inherent to the high confinement mode, also called H-mode. The H-mode was first discovered in ASDEX in 1982 [57] and is characterized by steep density and temperature - and therefore pressure - gradients in the plasma edge due to the formation of an edge transport barrier (ETB). This leads to increased temperature and density profiles across the whole plasma radius which improve the fusion performance.

However, a cyclic and transient loss of the confinement in the edge region of the plasma was already observed in these early experiments. This is typically observed through the increased emission of D-alpha light and spikes in the divertor shunt currents. This is identified as the so called edge localized modes (ELMs) [58, 59, 73, 74]. During ELMs, a sudden loss of particles and heat towards the plasma facing components (PFCs) takes place within a timescale of $\sim$ 1 ms. During the crash, the density and temperature gradients in the pedestal collapse. After the crash, the profiles slowly recover until the next ELM occurs, giving rise to the so-called *ELM cycle*. Despite the positive aspect of removing impurities from the plasma, the transient heat loads delivered to the PFCs are beyond the limit that current materials can withstand [75].

The current theoretical picture to explain ELMs is the peeling-balloning (PB) model [76, 77]. In this model, the ELM is a combination of peeling modes and ballooning modes driven by edge current density and pressure gradient. Whenever the PB stability boundary is crossed an ELM is triggered. Due to the incomplete understanding of the ELM instability, it is not possible to give a unified classification of ELMs. However, a phenomenological classification of ELMs can be made attending to their common characteristics observed experimentally [8]:

- Type-I ELMs: characterized by $\frac{d\nu_{ELM}}{dP_{sep}} > 0$, where ν_{ELM} is the ELM frequency and dP_{sep} is the power crossing the separatrix. These are the type of ELMs which exhibit the largest energy loss δW_{ELM}.
- Type-II ELMs: these type of ELMs do not show a clear correlation between ν_{ELM} and P_{sep}. They typically appear in highly shaped plasmas, close to double-null configuration.

[8] A more comprehensive classification of different ELM regimes is given in [59].

- Type-III ELMs: characterized by $\frac{dv_{ELM}}{dP_{sep}} < 0$. These are usually observed close to the L-H transition power. The variation of the ELM frequency rate with respect to the power crossing the separatrix is a common criterion to distinguish between Type-I and III ELMs.

As mentioned before, the expected heat-loads to the PFCs due to type-I ELMs is thought to be intolerable in future burning plasma experiments. Therefore, ELM control techniques have to be developed to either mitigate or suppress them. Some of these techniques can be highlighted such as the application of external magnetic perturbations (MPs) [78–81] or the injection of pellets [82, 83] among others. Alternatively, the development of intrinsically ELM-free regimes is also currently being investigated [84].

2.3 Fast-ion transport due to MHD instabilities

The transport of energetic ions due to MHD instabilities can be divided into two main categories: *resonant* and *non-resonant* transport [13, 85, 86].

Resonant transport

Due to the periodic nature of particle orbits and the periodic structure of the perturbation, the resonant transport relies on the capability of a particle to stay in phase with the mode perturbation. During this resonant interaction, the particles are able to exchange energy with the mode, and this can be eventually translated into a redistribution of the fast-ion distribution in phase-space.

A general theoretical framework for the wave-particle interaction in fusion plasmas can be found in [87]. Using a Hamiltonian formalism, the motion of the charged particles can be conveniently expressed in action-angle coordinates which define characteristic frequencies of the system. These pairs of action-angle coordinates are: (μ,α), where μ is the magnetic moment and α is the gyroangle; (P_ϕ, ϕ), where P_ϕ is the toroidal canonical angular momentum and ϕ is the toroidal angle; and (J,θ_c) where J is the second adiabatic invariant [64], and θ_c is the associated conjugate canonical angle:

$$J = \oint v_\parallel dl \tag{2.32}$$

$$\theta_c = \omega_b \int_\theta^0 d\theta' / \theta' \tag{2.33}$$

where ω_b represents the bounce and transit frequencies of trapped and passing orbits respectively:

$$\omega_b = \frac{2\pi}{\oint d\theta / \dot{\theta}} \tag{2.34}$$

This formalism allows to obtain general resonance conditions between charged particles and generic fluctuations taking the form:

$$f(r, \theta, \xi) = \sum_{m,n\in} \exp\left[in\xi - im\theta\right] f_{m,n}(r) \tag{2.35}$$

by carrying out a projection of the fluctuation along the particle motion in the magnetic equilibrium configuration. This leads to the following resonance conditions for trapped particles [87–90]:

$$\omega_{MHD} - n\omega_d - l\omega_b = 0 \tag{2.36}$$

and for passing particles:

$$\omega_{MHD} - n\omega_d - l\omega_b - (nq - m)\omega_b = 0 \tag{2.37}$$

where ω_{MHD} is the frequency of the mode, ω_d is the toroidal precession frequency and ω_b is the bounce or transit frequency, while n is the toroidal mode number, m the poloidal mode number and l the bounce harmonic. These *linear* resonant conditions can be eventually extended to the case in which the projection of the fluctuation is considered along the perturbed motion of the orbit, due to its interaction with the mode, leading to more complex *non-linear* resonance conditions.

Eqs.2.36 and 2.37 give the conditions for the particle to be in phase with the mode. If this is the case, then the particle and the mode are able to exchange energy. This energy exchange, as mentioned previously, can eventually be translated into a radial transport of the particle. This is given by the relation:

$$\Delta P_\phi = \frac{n}{\omega}\Delta E \tag{2.38}$$

which is derived from the fact that, in the presence of a perturbation, the energy and the toroidal canonical angular momentum are no longer conserved, but instead the variable $C = \omega P_\phi - nE$ is. In fact, this expression represents lines in the $P_\phi - E$ plane along which particles are displaced while in resonance [91].

However, the capability of the particle to stay in phase with the mode can be limited, due to the interaction between themselves. Mainly two mechanisms are responsible for this. During the mode-particle interaction the wave-particle phase can be shifted. This shift can accumulate up to the point in which the resonance condition does not hold anymore. This is called *resonance detuning*. On the other hand, the radial displacement of the particle orbit due to its interaction with the mode can move the particle apart from the mode location in real space. This is then called *radial decoupling*. Both of these mechanisms can limit the mode-particle interaction time and length. Therefore, what is needed for a particle to stay in resonance with the mode is that both, the wave-particle phase and the spatial radial overlap between these two is kept during the evolution of the system.

This resonant transport can eventually lead to a loss of the fast-ion confinement by different mechanisms:

- **Phase Locking:** if the conditions stated above are fulfilled and the wave-particle resonant interaction is sustained in time, then a secular radial displacement of the particles occurs [90]. These particles can then be lost by crossing a loss boundary in phase-space. This kind of transport mechanism typically occurs in the presence of energetic particle modes (EPMs), i.e: collective phenomena in which MHD instabilities are driven by the energetic particle population, since in these fluctuations the frequency of the mode is adjusted to the frequency of the particles as they are radially transported [88]. The character of this kind of transport mechanism is typically convective, scaling as $\propto \frac{\delta B}{B}$.

- **Orbit topology boundary crossing:** in this case, the resonant interaction can push a particle across a boundary in the particle phase-space, provoking a change in the topology of the orbit which can lead to the deconfinement of the particle. An example of such a case would be a change from counter-passing orbits to trapped orbits [44].

Non-resonant transport

Other mechanism that do not necessarily involve a resonant interaction between the mode and the particle can lead to enhanced fast-ion transport. Some of these are:

- **Loss boundary crossing:** an MHD instability can provoke a displacement of the magnetic field lines. Since the charged particles are following the field lines, this would lead to an equivalent displacement of the fast-ion trajectory, which could cause the orbit to cross a loss boundary in phase-space.
- **Field line ergodicity:** MHD instabilities can create ergodic field lines. Then, particles with large parallel velocities can be radially transported by the fact that they are following these magnetic field lines. An example of this could be the losses due to the application of external magnetic perturbations [92].
- **Multiple resonances:** in the presence of multiple resonances, an overlapping of islands in phase-space can occur, which can then lead to a stochastic motion of the particles [93–95], provided that the Chirikov criterion is fulfilled [96]. This mechanism is commonly observed in the presence of multiple MHD modes. The character of this kind of transport is typically diffusive, scaling as $\propto \left(\frac{\delta B}{B}\right)^2$.
- **Avalanches:** gradients in the fast-ion distribution function can drive EPMs [97]. A fast-ion population can be radially redistributed do to its interaction with the EPMs. Then, a gradient in the fast-ion distribution is established but at the new (different) radial position, which can then trigger new EPMs, repeating the process once again [88, 91].

Chapter 3

Experimental Setup

In the framework of this thesis the experiments have been carried out at the ASDEX Upgrade tokamak, at the Max Planck Institute for Plasma Physics in Garching (Germany). In this chapter the main characteristics of this device will be presented, together with a brief description of the main diagnostics which are used in the routine operation of the device and have been relevant for this work. More emphasis will be put on the description of fast-ion loss detectors.

3.1 ASDEX Upgrade

ASDEX Upgrade (AUG) [98] is a medium size tokamak with a plama major radius of $R_0 = 1.65$ m and minor radius $r = 0.5$ m. The toroidal magnetic field is up to 3.1 T and the plasma current 1.6 MA. The plasma discharges can last up to $\sim$ 10s and densities of the order of $10^{19} m^{-3}$ and electron temperatures up to $\sim$ 7 keV are obtained. Up to 30 MW of external heating power can be applied divided into three auxiliary heating systems:

- Neutral beam injectors (NBI): the system consists of two boxes with four injectors (Q1-Q4 and Q5-Q8) each operating at a maximum extraction voltage of 60 kV and 93 kV respectively for deuterium. A maximum power of 20 MW can be injected with this system.
- Ion cyclotron resonance heating: the system consists of 4 antennas which launch waves in the ion cyclotron frequency range, usually at 30 MHz and 36.5 MHz. A maximum power of around 4 MW can be injected with this system [99].
- Electron cyclotron resonance heating: the system consists of up to 8 gyrotrons which launch waves in the electron cyclotron frequency range from 105 to 140 GHz. A maximum power of 0.6 MW can be injected with each gyrotron [100].

In the following an overview is given of the main diagnostics which are used in the routine operation of AUG and are relevant for this work.

3.1.1 Density and temperature measurements

The two main magnitudes that characterize a plasma are the density and the temperature. Thus, the diagnostics measuring these two are of great importance during the operation of a tokamak. In AUG several diagnostics are used to measure the electron density.

DCN laser interferometry

One of them is a deuterium cyanide (DCN) interferometer [101]. This diagnostic measures the phase shift between two branches of a coherent electromagnetic wave (a laser), one going through the plasma and the other in vacuum. The phase shift is provoked by a different propagation of the light due to the refractive index of the plasma $N = \sqrt{1 - \frac{\omega_p^2}{\omega^2}}$. The phase shift is found to be proportional to the line integrated plasma density, which can then be recovered from the measurement:

$$\Delta\Phi = \frac{\omega_0 e^2}{2c\epsilon_0 m_e \omega_0^2} \int n_e(x) dx \tag{3.1}$$

At AUG, this system has a time resolution of $300\mu s$ and has 5 different lines of sight (LOS) through the plasma.

Thomson scattering

The Thomson scattering (TS) diagnostic is capable of measuring both, electron density and temperature. The measurement principle is the scattering of an incident wave by charged particles in the plasma. Due to the mass difference ($m_i >> m_e$) the scattering with free electrons dominates the process. These charged particles are moving relative to both, the incident and the scattered wave, and therefore the Doppler shift needs to be taken into account:

$$\Delta\omega = v \cdot (k_i - k_s) \tag{3.2}$$

where $\Delta\omega$ is the frequency shift of the scattered wave, v is the velocity of the charged particle, and k_i and k_s are the wave vectors of the incident and scattered wave. The measurement of the width of the scattered spectrum gives then information about the velocity distribution of the charged particles, which can be related to the temperature, while the intensity of the scattered radiation gives information about the density. The TS diagnostic is capable of providing simultaneous measurements of density and temperature.

The TS system at AUG [102] provides measurements at the edge and the core of the plasma using Nd-YAG lasers. It provides measurements with a spatial resolution of 25 mm in the core and 3 mm in the edge of the plasma, and a time resolution of 8 ms.

Lithium beam spectroscopy

In addition, a lithium beam emission spectroscopy system [103, 104]provides electron density measurements with high resolution in the plasma edge. This diagnostic injects a beam of neutral lithium atoms into the plasma with energies between 35 and 60 keV. As they penetrate in the plasma, the bounded electrons are excited into higher energy levels with the consequent emission of light during the transition back to the ground state. This light, with a wavelength of 670.8 nm corresponding to the transition Li $2p - 2s$, is imaged and its intensity can be related to the plasma density through a collisional-radiative model. In AUG this system has a temporal resolution of $50\mu s$ and a set of 35 channels, which provides a high spatial resolution for the recovery of radial profiles.

Electron cyclotron emission

The main diagnostic to measure the electron temperature in AUG, together with the Thomson scattering, is the electron cyclotron emission (ECE) system. In AUG there are multiple ECE diagnostics available which are described in [105]. This diagnostic is based on the radiation emitted by electrons gyrating in the presence of a magnetic field, with a frequency of $\omega_{ce} = \frac{eB}{m_e}$. If the plasma is optically thick, i.e: all of the emitted radiation is absorbed by the surrounding plasma, then Planck's law of black-body radiation prevails, which for high temperatures results in the Rayleigh-Jeans approximation:

$$I_\omega = \frac{\omega^2}{2\pi^2 c^2} k_B T_e \tag{3.3}$$

where I_ω is the spectral radiance at the frequency ω, and $k_B T_e$ is the electron temperature. The electron temperature can then be obtained by measuring the intensity at a given frequency. The measurement can be mapped through its cold resonance position given the relation between the frequency and the magnetic field, whose dependence with the radial coordinate is well known.

Under more complicated circumstances such as an optically thin plasma where the black-body radiation assumption is not valid, or if broadening effects need to be taken into account, in which the cold resonance approximation does not hold anymore, forward modelling of the radiation transport is needed for a correct interpretation of the measurement [106, 107].

It is worth to mention that a framework has been established in AUG by means of which the kinetic profiles can be retrieved combining the information provided by different diagnostics. This is the so-called integrated data analysis (IDA) tool which is based on a Bayesian probability approach [108].

Charge exchange recombination spectroscopy

The ion temperature can be measured with charge exchange recombination spectroscopy (CXRS) diagnostics [109]. In a charge exchange reaction between an impurity ion and a neutral particle, usually deuterium in AUG, an excited state of the impurity ion can be populated. The following decay to the ground state leads to the characteristic emission of light.

$$A^{Z+} + D^0 \rightarrow A^{(Z-1)+} + h\nu + D^+ \tag{3.4}$$

The spectrum provides information about the ion temperature (through the width of the peak), the ion velocity (through the Doppler shift of the peak) and density of the species (through the intensity of the peak). This allows to infer the radial electric field of the plasma from the force balance equation [110, 111]. In AUG there are multiple CXRS systems which use the spectral lines of different impurities such as boron, nitrogen or carbon [112, 113].

3.1.2 Magnetic measurements

In tokamaks, magnetic field perturbations can be measured by using the so-called magnetic pick-up coils. The working principle is based on the Faraday law:

$$\epsilon = -\frac{d\phi}{dt} = -\frac{d(\vec{B}\vec{A})}{dt} \tag{3.5}$$

Using a wire loop with surface A, an electromotive force ϵ is induced whenever a temporally varying magnetic field penetrates through it. Depending on the orientation of the loop, different components of the magnetic field can be measured: toroidal, poloidal or radial. In AUG a number of magnetic pick-up coil arrays are installed in both the low field side and the high field side of the tokamak [114]. They allow the detection of instabilities with frequencies up to 2 MHz and an analysis of their toroidal and poloidal mode numbers.

3.1.3 Thermography measurements

Thermography diagnostics measure the heat-flux distribution on different plasma facing components. They rely on the infrared (IR) emission of these to determine the surface temperature using Planck's law. The heat flux can then be retrieved by solving the heat diffusion equation [115]. In AUG several IR diagnostics are installed. The most relevant with respect to this work is the 2D system used to image the FILD1 probe which is mounted on the midplane manipulator.

3.2 Fast Ion Loss Detector

ASDEX Upgrade is well equipped with a comprehensive set of diagnostics for fast-ion studies, each of them conceived to measure different volumes of the phase-space of the fast-ion distribution function. Among the diagnostics used to measure confined fast-ion populations there are: fast-ion D-alpha (FIDA) spectroscopy [116], neutral particle analyzers (NPAs) [117], collective Thomson scattering (CTS) [118], ion cyclotron emission (ICE) [119]. Neutron measurements [120, 121], which rely on the occurrence of fusion reactions, provide a global measurement and are often used to complement direct fast-ion observations. On the other hand, scintillator based fast-ion loss detectors (FILD) [122] are used to diagnose the escaping fast-ion population. The basics of FILD diagnostics are described in the following.

With FILD detectors, the fast ions escaping from the plasma are collected by a scintillator plate, which emits light when irradiated by charged particles. They consist mainly of two different parts: a probe and a light acquisition system. The probe is placed near the plasma edge, in the far scrape-off layer (SOL), and the main elements are: a scintillator plate, which is the active component of the detector; a collimator, which only allows certain particle trajectories; and a head protection which shields these elements from radiation and thermal loads.

One could describe FILD detectors to work as magnetic spectrometers that take advantage of the tokamak magnetic field to disperse charged particles into different positions of a scintillator plate. A sketch of a typical setup of a FILD diagnostic is shown in Fig. 3.1. The working principle is the following: fast-ions are performing helical trajectories around the magnetic field lines. On their gyromotion, lost ions will eventually reach the collimator's pinhole. As will be described in Chapter 4, only certain trajectories are capable of making it through the collimator all the way into the scintillator, which will emit light. The particle will impinge on different positions of the scintillator depending on its gyroradius and pitch angle, thus allowing

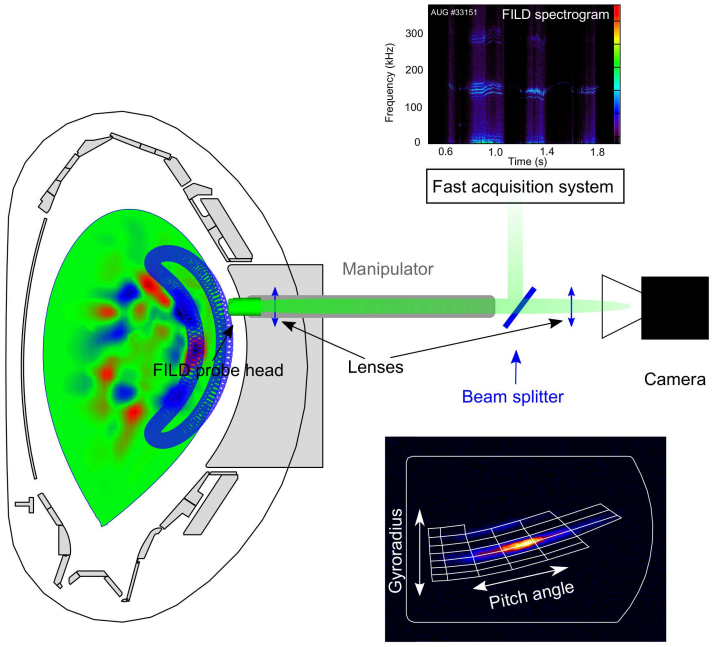

FIGURE 3.1: Schematic of a generic FILD diagnostic showing the most important elements: the probe head, the manipulator, the lenses, a camera and a fast acquisition system.

a direct measurement of the velocity-space of the fast-ion loss distribution. If the impinging species is known (or assumed) its energy can be easily retrieved given the magnetic field at the probe position. A more detailed description on how the velocity-space of the fast-ion losses can be retrieved from these measurements will be given in Chapter 4.

Understanding the light emission process of the scintillator is key for the analysis of fast-ion losses. A comprehensive characterization of scintillating materials [123–125] including the yield of the scintillator and its behaviour at different temperatures, the light spectrum, the decay time and the degradation as a function of the fluence, is needed for an optimum choice of the material. The emitted light goes to a light acquisition system which handles the imaging of the scintillator. This setup can change within different machines, but typically consist of a system which provides a good spatial resolution of the scintillator. This is translated into a good velocity-space resolution of the system, and a system which provides a good (fast) temporal resolution, which allows to measure fast-ion losses induced by high frequency instabilities.

In AUG a set of 3 FILDs were available at the beginning of this thesis. These were:

- FILD1: which is mounted by request temporarily on the midplane (retractable) manipulator, located in sector 7 at approximately $Z = 0.33$ m and $\Phi = 169^o$.
- FILD2: which is permanently mounted in sector 3 at approximately $Z = 0.33$ m and $\Phi = 55^o$.

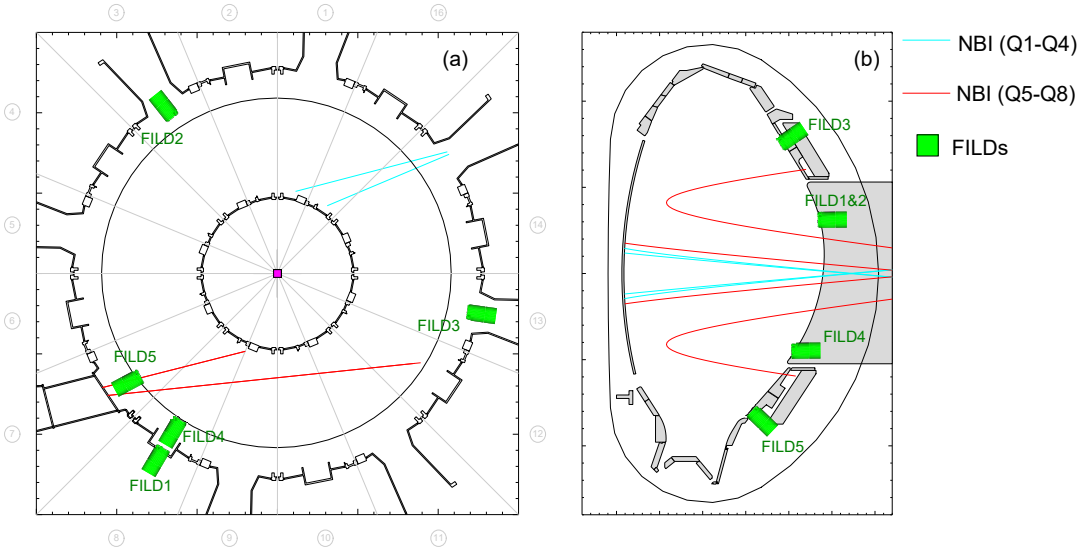

FIGURE 3.2: Overview of FILD systems at AUG. The injection geometry of the NBI systems is also shown.

- FILD3: which is permanently mounted in sector 13 at approximately $Z = 0.8$ m and $\Phi = 281^o$.

During this period two additional FILDs have been installed: FILD4 [126] which is located below the midplane in sector 8 and has a novel magnetic drive for its reciprocation; and FILD5 [127] which is located in sector 7 near the divertor. Figure 3.2 shows an overview of the FILD systems installed in AUG in the toroidal (a) and poloidal (b) planes, together with the injection geometries of the NBI systems.

In AUG, not all of the FILD systems have the same light acquisition system. FILD1 uses a fast CMOS camera (Phantom v710 from Vision Research[1]) for the high spatial resolution measurement which provides frame rates larger than 1 kHz, while for the fast measurements a set of 20 photomultiplier tubes (PMT) is used, each of them imaging a different region of the scintillator, with a time resolution of 1 MHz. FILD2, on the contrary, uses a charged coupled device (CCD) camera (pixelfly VGA from pco. imaging[2]) operated at a frame rate of 50 Hz, while a similar system of PMTs is used for the fast response signal. FILD3 lacks of such a fast response system, and its scintillator is only imaged by a CCD camera of the same model.

In addition to AUG [122], FILD detectors have been installed in a number of magnetically confined fusion devices such as TFTR [128], DIII-D [129] and KSTAR [47] among others. They have been demonstrated to be a unique diagnostic to study fundamental mechanisms leading to fast-ion transport and loss due to a wide variety of plasma instabilities such as Alfvén Eigenmodes [40–43, 130–132], tearing modes [26, 133], fishbones [29, 33, 134], edge localized modes [19] or externally applied magnetic perturbations [20–22].

[1] http://www.phantomhighspeed.com/Products/v-Series-Cameras
[2] https://www.pco.de/fileadmin/user_upload/db/products/datasheet/pixelfly_20090505_02.pdf

Chapter 4

FILDSIM: model for the instrument response

In chapter 3 the basic operational principles of scintillator based FILD detectors were presented. Although previous works have reported on some aspects of the resolution limitations of FILD diagnostics [122, 135–138] a comprehensive description of the FILD instrumental response and the velocity-space sensitivity is given here for the first time. To this end, a simple model based on a weight function formalism has been developed and implemented in a code called FILDSIM [139]. In this chapter a detailed description of the FILDSIM model is given and its capabilities and limitations are discussed.

4.1 Trajectory calculations in the FILD probe head

The first step in order to characterize the response of the FILD detector, is to carry out trajectory calculations of the ions in the detector's head probe. Fig.4.1 shows qualitatively how the probe head looks like and how the trajectories go through the collimator and hit the scintillator. The code computes the ion trajectories started at the detector pinhole and follows them on their way up to the scintillator. It detects any collisions between the ions and the realistic 3D detector geometry elements. The code assumes that the local magnetic field in the volume of the head probe is constant. This assumption is justified provided that the size of the FILD probe head, which is typically determined by the size of the gyroradius of the ions to be measured, is small compared to the size in which the spatial magnetic field variations of the equilibrium are relevant. The main parameters of the FILD1 probe head geometry in AUG are indicated in Table 4.1. In medium size tokamaks like ASDEX Upgrade the magnetic field variation in such a volume is found to be below 1%. The applicability of this assumption is illustrated in Fig.4.2, where the strike-points of a collection of ions in the scintillator has been calculated by solving the Lorentz equation of motion in the realistic spatially varying magnetic field (in blue) and using the approximation of constant magnetic field, taken at the center of the scintillator (in red). The difference in the strike-points on the scintillator is of the order of 300 μm, which is well below the resolution of the detector as will be shown later. Therefore, there is no need to solve the Lorentz equation of motion since the analytical solution of the ion orbits in a constant magnetic field are well known to be helixes. This reduces substantially the computational time.

A number N of ions with fixed gyroradius and pitch angle are started with random positions in the entrance plane of the pinhole and random gyrophases. The ions are followed until they collide with the scintillator or with any other geometry

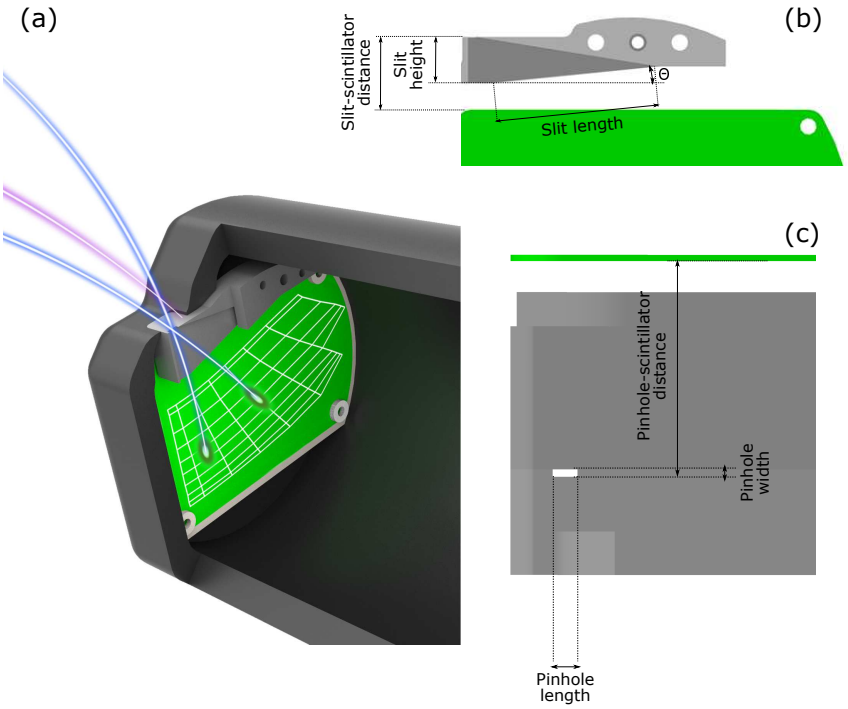

FIGURE 4.1: (a) 3D view of the FILD probe head (dark grey) and the scintillator (green). Fast-ion orbits are shown in purple (blocked by the collimator) and blue (not blocked by the collimator). The strike-map (in white) is overlayed on the scintillator. (b) and (c) show more detailed side views of the collimator highlighting the most important parameters. [139]

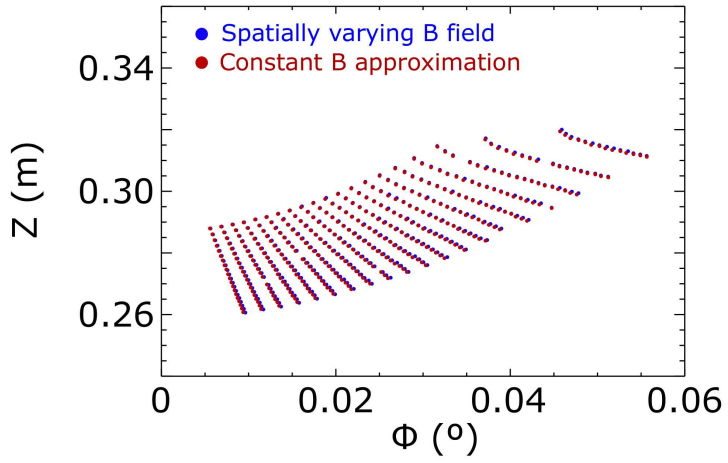

FIGURE 4.2: Strike points on the scintillator calculated in the realistic spatially varying magnetic field by solving the Lorentz equation of motion (blue) and by assuming a constant magnetic field (red). The difference in the strike-point position is of the order of 300 μm.

Geometry element	Dimensions
Pinhole length	2 mm
Pinhole width	0.5 mm
Slit height	10 mm
Pinhole - scintillator distance	5.75 mm
Probe head diameter	7.2 cm
Scintillator dimensions	3.3 x 4.8 cm^2

TABLE 4.1: Dimensions of the main elements shown in Fig.4.1 corresponding to the particular case of FILD1 at ASDEX Upgrade. [139]

element. This process is repeated for the relevant range of gyroradius and pitch angle values. It should be noticed that throughout this thesis the ion gyroradii will be referred rather than their energies. This is because the FILD diagnostic measures the Larmor radius of the particles regardless of what species the particle is. Given the magnetic field at the probe position, the energy can be calculated for any impinging ion species. The information that can be retrieved from this simulations is described in the following.

Ion trajectories started at the pinhole with a fixed value of gyroradius and pitch angle have a distribution of strike points in the scintillator due to the random initial positions and gyrophases of the ions. The centroid of such a distribution can be computed for all gyroradius and pitch angle values leading to a strike map, an example of which is shown in white in Fig.4.1(a). This strike map defines the velocity space of the ions measured in the scintillator, given by the gyroradius ρ'_L and the pitch angle Λ'.

The size and shape of these distributions give information about the resolution of the detector. The resolution in gyroradius is illustrated in Fig.4.3 (a), which shows the gyroradius distribution profiles obtained in the scintillator velocity space (ρ'_L) along a line of constant pitch angle (Λ'). The different colors correspond to different values of the particle gyroradius started at the detector pinhole. The strike-point distributions can be fairly well modelled as asymmetric Gaussians (skew Gaussians). The fit to this model is represented by the solid lines in Fig.4.3 (a). It can be seen that for small values of the ion gyroradius, the distributions do not overlap, and thus different spots in the scintillator can be easily identified. However, if two strike point distributions for different values of gyroradius and pitch angle overlap, no direct one-to-one mapping between the velocity-space in the pinhole and the velocity-space on the scintillator exists, and this is what happens for larger gyroradii values. Fig.4.3(b) shows one of these strike-point distributions in detail. It can be observed that the strike-points distribution fits better to a skew Gaussian function (red curve) than to a Gaussian function (black curve).

The resolution in pitch angle is illustrated in Fig.4.4 (a), which shows the pitch angle distribution profiles obtained in the scintillator velocity space (Λ') along a line of constant gyroradius (ρ'_L). In this case, the strike-point distributions are modelled by Gaussian functions. A similar resolution is obtained for all pitch angle values.

Some of the markers started at the pinhole will not impinge on the scintillator but will be blocked by the collimator. We define the collimator factor as the ratio

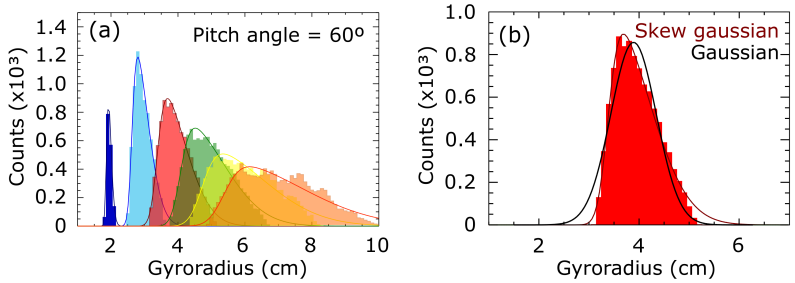

FIGURE 4.3: (a) Gyroradius distribution profiles in the scintillator velocity space along a line of constant pitch angle. Different colors correspond to different values of the particle gyroradii started at the FILD pinhole. The solid lines are the fit to the skew Gaussian model. (b) Zoom into a single distribution corresponding to $r_L = 4$ cm. The fit to a Gaussian distribution is shown in black, while the fit to a skew Gaussian function is shown in red. [139]

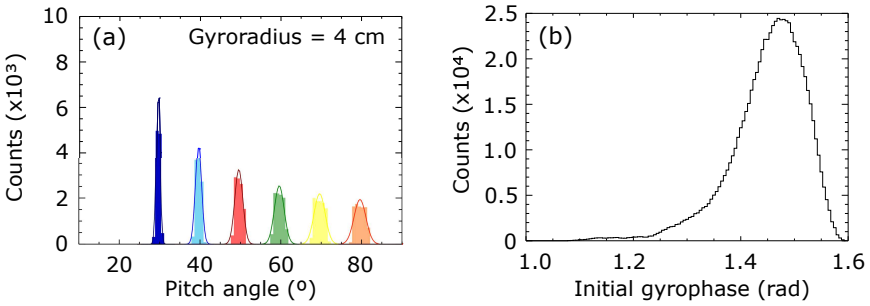

FIGURE 4.4: (a) Pitch angle distribution profiles in the scintillator velocity space along a line of constant gyroradius. Different colors correspond to different values of the particle pitch angle started at the FILD pinhole. The solid lines are the fit to the Gaussian model. (b) Histogram of the particles initial gyrophase which are not blocked by the detector collimator. [139]

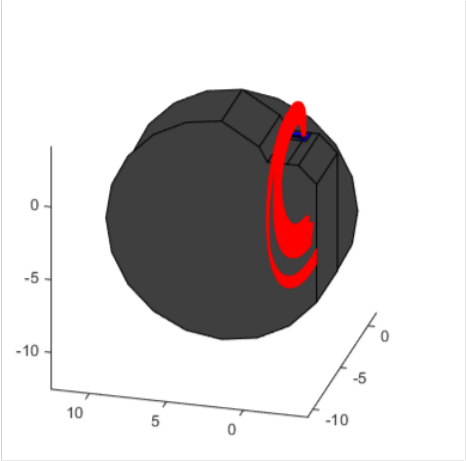

FIGURE 4.5: Ion trajectories calculated backwards from the pinhole.

between the number of markers reaching the scintillator and the number of markers started at the pinhole, $f_{col} = \frac{N_s}{N_p}$, for fixed values of gyroradius and pitch angle. The collimator factor is needed, for instance, to estimate the absolute flux of fast-ion losses at the FILD probe head. The ions that are not blocked by the collimator are those whose initial gyrophase lies inside an acceptance cone, which is determined by the collimator geometry, shown in Fig.4.4 (b). The code also allows to perform backward tracing of the trajectories. This is useful in order to discard self-shadowing effects of the detector probe head itself, which typically can happen for particles with low $\frac{v_{||}}{v}$. An example of such a case is illustrated in Fig.4.5.

The properties described above, as well as the range in the gyroradius and pitch angle coverage, are determined by the design of the collimator, whose main parameters are illustrated in Tab.4.1. For instance, a wider pinhole or a wider slit will generally lead to a larger collimator factor (this is, a smaller fraction of the incoming ions being blocked) at a cost of lower resolution in gyroradius, which will be described later. The resolution in pitch angle is mainly determined by the length of the pinhole, while the height and the angle of the slit determine the range in velocity-space that can be measured. A compromise between these properties must be made when designing the collimator.

4.2 Description of the model

In the previous section it was shown that the velocity-space measurement of fast-ion losses is based on the pattern that these ions leave on the scintillator plate: ions with different pitch-angle and gyroradius will impinge in different regions of the scintillator. However, the interpretation of these patterns is not always straightforward. The finite size of the collimator limits the resolution of the detector in both, pitch-angle and gyroradius. The distribution measured at the scintillator plate can then be thought of as a distortion of the velocity-space of the fast-ion loss distribution reaching the detector pinhole due to the limited resolution, which is inherent to any instrument in physics.

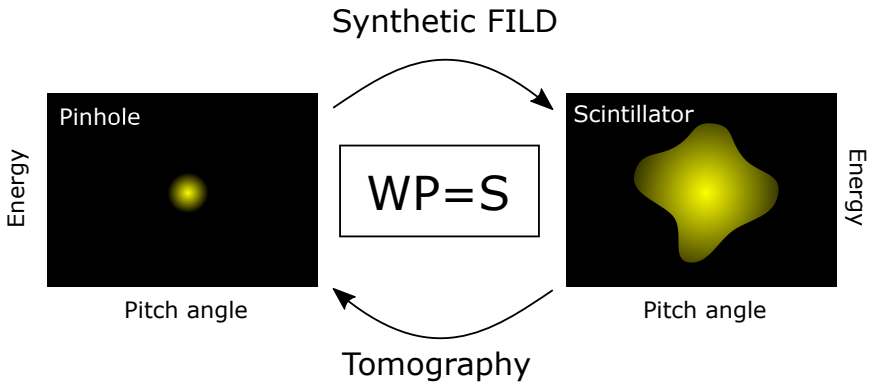

FIGURE 4.6: Cartoon illustrating the response of FILD detector. The velocity-space distribution measured at the scintillator (S) is a distortion of the velocity-space distribution reaching the detector pinhole (P). Both are related by a weight function (W).

With the information obtained in the trajectory simulations we propose a simple model to relate the velocity space of the ions reaching the FILD pinhole $\Gamma_P(\rho_L, \Lambda)$, to the pattern measured by the scintillator $\Gamma_S(\rho'_L, \Lambda')$, which can be understood as a distortion of the velocity space of the losses in the pinhole due to the finite resolution of the system. Notice that the $'$ is used to differentiate between the velocity space defined at the pinhole and the velocity space defined at the scintillator. This is illustrated by the cartoon in Fig.4.6. Even if the velocity-space distribution of ions reaching the detector pinhole is infinitely well defined (e.g: $\Gamma_P(\rho_L, \Lambda) = \delta(\rho_L - \rho_{L0}, \Lambda - \Lambda_0)$), a finite-sized pattern will be created in the scintillator plate. Using a weight function formalism similar to the formalism used in other fast-ion diagnostics such as FIDA, CTS or NPA [140–147], the signal measured at the scintillator can be expressed as:

$$\Gamma_S(\rho'_{L_1}, \rho'_{L_2}, \Lambda'_1, \Lambda'_2) = \int_0^{2\pi} \int_0^{\infty} w(\rho'_{L_1}, \rho'_{L_2}, \Lambda'_1, \Lambda'_2, \rho_L, \Lambda) \cdot \Gamma_P(\rho_L, \Lambda) d\rho_L d\Lambda \quad (4.1)$$

Γ_S is the measured signal in the gyroradius range $\rho'_{L_1} < \rho'_L < \rho'_{L_2}$ and pitch angle range $\Lambda'_1 < \Lambda' < \Lambda'_2$ in units of $[photons]$, which depends on the velocity space coordinates defined in the scintillator. Γ_P is the velocity space distribution of the lost ions in the pinhole in units of $[ions/(rad \cdot m)]$, and w is the instrument weight function, thus in units of $[photons/ion]$. The weight function in this case can be split into the product of a probability function $\text{prob}(\rho'_{L_1} < \rho'_L < \rho'_{L_2} \wedge \Lambda'_1 < \Lambda' < \Lambda'_2 | \rho_L, \Lambda)$, which maps the distribution in the pinhole to the distribution measured in the scintillator, and a function accounting for the yield of the scintillator $\epsilon(\rho_L)$ which is described later. The probability function can then be thought of as the probability that an ion reaching the pinhole with gyroradius ρ_L and pitch angle Λ has to impact the scintillator in a region such that $\rho'_{L_1} < \rho'_L < \rho'_{L_2}$ and $\Lambda'_1 < \Lambda' < \Lambda'_2$.

Formally the weight function $w(\rho'_{L_1}, \rho'_{L_2}, \Lambda'_1, \Lambda'_2, \rho_L, \Lambda)$ can be calculated by introducing a δ-function in Eq.4.1 and evaluating the expected pattern in the scintillator:

$$\Gamma_P(\rho_L, \Lambda) = N_f \cdot \delta(\rho_L - \rho_{L0}) \cdot \delta(\Lambda - \Lambda_0) \quad (4.2)$$

where N_f is the number of ions with a certain gyroradius ρ_{L0} and pitch angle Λ_0. This is effectively being done in the trajectory simulations described in the previous

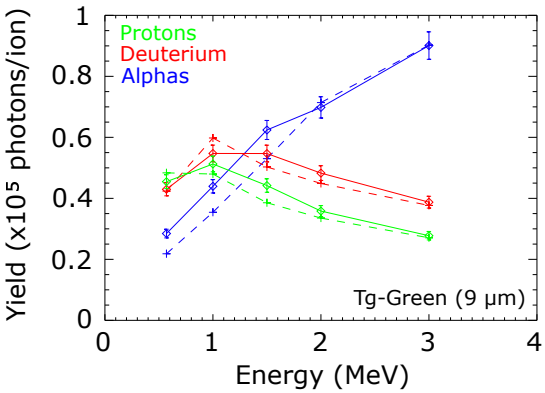

FIGURE 4.7: Yield of Tg-Green scintillator for the different species of interest. Full lines correspond to the experimental measurements, while dashed lines correspond to the theoretical values obtained from Birk's model. [139]

section. The amplitude of the weight function at the velocity space position ρ_{L0}, Λ_0 is then:

$$w(\rho'_{L_1}, \rho'_{L_2}, \Lambda'_1, \Lambda'_2, \rho_{L0}, \Lambda_0) =$$
$$\text{prob}(\rho'_{L_1} < \rho'_L < \rho'_{L_2} \wedge \Lambda'_1 < \Lambda' < \Lambda'_2 | \rho_L, \Lambda) \cdot \epsilon(\rho_{L0}) = \frac{\Gamma_S(\rho'_{L_1}, \rho'_{L_2}, \Lambda'_1, \Lambda'_2)}{N_f} \quad (4.3)$$

where $\epsilon(\rho_{L0})$ is the scintillator efficiency. The efficiency function ϵ contains the information about the yield of the scintillator, this is, the number of photons emmitted by the scintillator per incident ion, which is a function of the particle species and energy. The characterization of the scintillator material (TG-Green in this case)[124, 148] has been carried out in an accelerator facility. Fig.4.7 shows the experimental measurements of the scintillator yield as a function of energy for protons, deuterium and alpha particles. A good agreement is observed with the theoretical values obtained from the application of Birk's model[124]:

$$\frac{dY}{dx} = \frac{S \cdot \frac{dE}{dx}}{1 + k \cdot \frac{dE}{dx}} \quad (4.4)$$

where $\frac{dY}{dx}$ is the photon yield per unit length, $\frac{dE}{dx}$ is the stopping power of the incident particles, and S and k are constants inferred from the measurements which are related to the scintillator efficiency and the degree of quenching, respectively. This model is used to obtain the scintillator yield at lower energies, of interest for NBI generated fast ions.

By discretizing the velocity space, Eq.4.1 can be expressed in matrix form as:

$$\Gamma^S_{ij} = \sum_{k,l} W_{ijkl} \Gamma^P_{kl} = \sum_{k,l} T_{ijkl} \epsilon_k \Gamma^P_{kl} \quad (4.5)$$

where the separation between the probability function, labeled as T, and the scintillator efficiency function ϵ is explicitely highlighted.

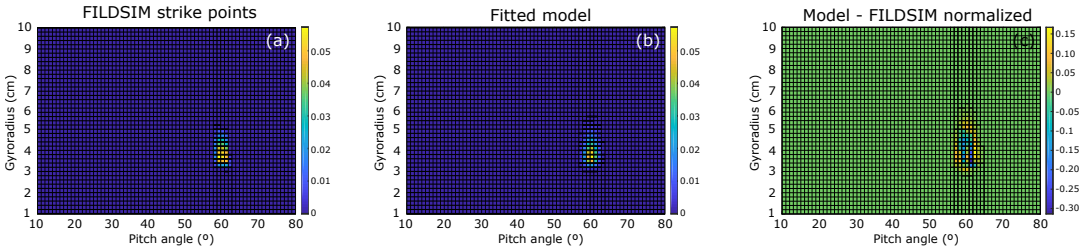

FIGURE 4.8: (a) 2D histogram of the strike-points obtained from the orbit calculations in the gyroradius-pitch angle space at the scintillator. (b) 2D histogram obtained from the fitted analytical model. (c) Difference between (a) and (b). [139]

In principle the probability matrix can be calculated numerically from the trajectory calculations. However, the velocity space of the FILD signals is typically discretized with $\Delta\rho \sim 0.1$ cm and $\Delta\Lambda \sim 1^\circ$, so that the details of the distribution can be resolved. This usually leads to a matrix size for Γ^P of 100×90 elements, which means that orbit trajectory calculations should be done for 9000 pairs of gyroradius and pitch angle values. In order to get good statistics typically 10^5 markers are simulated for each pair. To save computational time and as a useful tool to gain insight quickly, an analytical model for the shape of the probability functions was developed. As shown in the previous section in Fig.4.3 (a) and Fig.4.4 (a) , the projections of T_{ij} for a fixed k and l can be modelled as skewed Gaussians. Using this approximation the elements of the probability matrix T_{ijkl} can be written as:

$$T_{ijkl} = \frac{f_{col_{kl}}}{2\pi\sigma_{\Lambda,kl}\sigma_{\rho,kl}} \cdot \exp\left[-\frac{(\rho_i' - \rho_k)^2}{2\sigma_{\rho,kl}^2} - \frac{(\Lambda_j' - \Lambda_l)^2}{2\sigma_{\Lambda,kl}^2}\right] \cdot \left[1 + \mathrm{erf}\left(\alpha_{\rho,kl} \cdot \frac{\rho_i' - \rho_k}{\sqrt{2}\sigma_{\rho,kl}}\right)\right] \quad (4.6)$$

where f_{col} is the collimator factor, σ_ρ and σ_Λ are the parameters controlling the width of the distribution, erf is the error function and α_ρ is the parameter controlling the skewness of the distribution in the gyroradius direction.

Fig.4.8 shows the comparison between the 2D distributions obtained directly from the orbit calculations (a) and the fit to the analytical model (b), where the distributions have been normalized to unity. Slight differences can be observed as shown in Fig.4.8 (c). The main discrepancy is of the order of $\sim 15\%$ and is obtained in the edges of the distribution. This is due to the tails of the Gaussian functions, which do not fall to zero as sharply as the simulated distributions, meaning that the analytical model could be leading to an underestimation of the detector resolution. However, in general a good agreement is found between the fitted model and the results obtained from the orbit calculations. Further optimization of the analytical model towards a better fit to the numerical results of the strike-point distributions is left for future work.

This way, it is possible to perform the orbit trajectory calculations on a much coarser grid (i.e. 10×9), and build a finer grid by interpolation of the parameters in the model f_{col}, σ_ρ, σ_Λ and α, which are functions of the velocity space coordinates

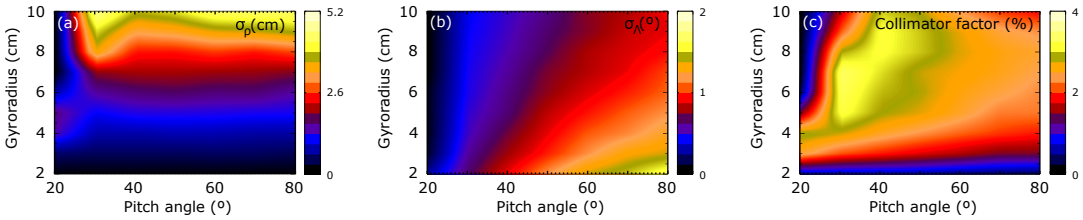

FIGURE 4.9: Contour plots of the main parameters of the model, defined in the pinhole space $\rho - \Lambda$. (a) σ_ρ, (b) σ_Λ and (c) f_{col}. [139]

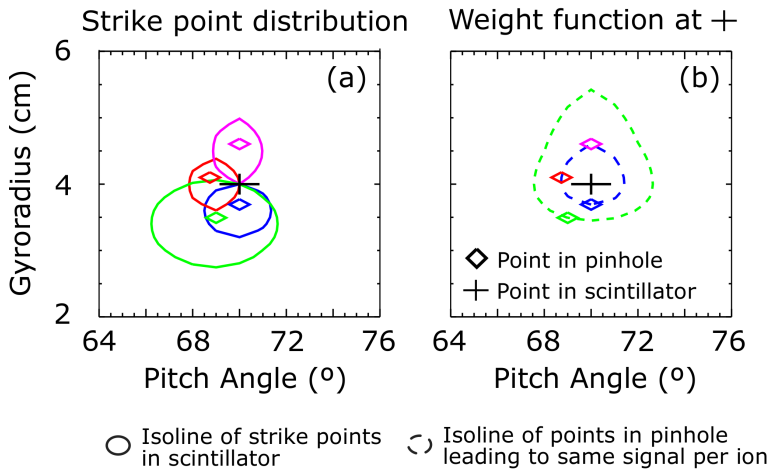

FIGURE 4.10: Cartoon illustrating the behaviour of the FILD weight function. Subfigure (a) shows the isolines of strike points in the scintillator for different points in the pinhole. Subfigure (b) shows the isolines of points in the pinhole leading to the same signal per ion in the scintillator. [139]

ρ and Λ defined in the pinhole and behave well in terms of continuity and differentiability, as shown in Fig.4.9. It can be seen that the collimator factor ranges from $0 - 4\%$. The resolution in gyroradius, approximated by σ_ρ, becomes lower for larger gyroradii as was previously described, while the resolution in pitch angle is similar throughout the whole velocity-space being approximately $\sim 1^\circ$, although a slight dependence with the pitch angle is observed.

The behaviour of the FILD weight function is schematically illustrated in Fig.4.10. In Fig.4.10 (a), different positions in the pinhole velocity space are represented by the empty diamonds. Associated to each of these points, isolines of the strike point distribution in the scintillator are represented by the solid lines. All of these lines go through the same point in the scintillator velocity space, represented by a black cross. Correspondingly, in Fig.4.10 (b) the dashed lines represent contour levels in the pinhole velocity space which would lead to the same signal per ion at the mentioned position in the scintillator velocity space. The blue line corresponds to a larger probability than the green line.

Fig.4.11 (a), (b) and (c) show the FILD weight functions for a fixed pixel of the scintillator velocity space. It shows the regions of the velocity space in the pinhole k, l (contour plot) which generate measurable signal in the scintillator velocity space

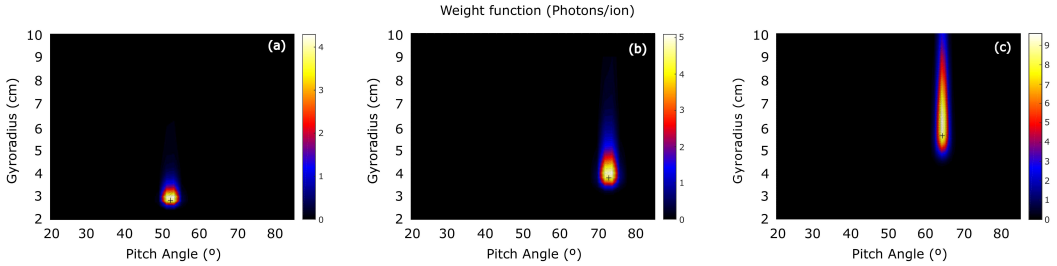

FIGURE 4.11: Examples of FILD weight function showing the region of the velocity space in the pinhole (contour) that can produce signal in a certain point of the velocity space in the scintillator (black cross). [139]

bin i, j (black cross), which is different for these three cases. The black regions do not generate any signal in that velocity-space bin. It can be noticed that the weight functions are well localized in the pitch angle direction, while they are rather extended in the gyroradius direction and not symmetrical with respect to the scintillator velocity space bin. This can be understood by looking at the skewed Gaussian distributions discussed previously, which are wider for larger gyroradii. It is therefore more likely for a bin in the scintillator velocity space to pick up signal from large gyroradii regions in the pinhole velocity space rather than from low gyroradii regions.

Using Eq.4.5, it is straightforward to obtain the velocity space distribution at the scintillator given a velocity space distribution of the losses at the FILD head probe. The latter can be provided by orbit following codes such as ASCOT[149] or OFMC[150]. This is of great utility to compare the experimental measurements with simulations[151]. Otherwise, the direct comparison can sometimes be misleading, in particular due to the limited resolution of the system at large gyroradii.

For comprehensive comparisons with the codes, the raw measurements need to be related to the velocity distribution on the scintillator plate. This is possible provided a full characterization of the scintillator response and a calibration of the optical system [123, 148]. The velocity distribution on the scintillator is obtained from the raw signal as follows:

$$\Gamma^S_{ij} = \sum_{p,q} R_{ijpq} C_{pq} \Xi^S_{pq} \tag{4.7}$$

where Ξ^S_{pq} is the raw measurement, i.e: the counts measured for each pixel p, q of the camera frame, C_{pq} is a calibration matrix, and R_{ijpq} is a matrix which maps the frame pixels to the velocity space coordinates.

The calibration matrix C_{pq} contains the information about the full calibration of the optical system, which consists basically of a set of lenses, a beam splitter and a bandpass filter. The calibration is performed using an integrating sphere which provides a well-known integrated photon flux. This light source is placed in the scintillator position and a calibration frame is recorded with the data acquisition system, in this case a camera. The calibration matrix takes the following form:

$$C_{pq} = \frac{1}{A_P \cdot \Delta t \cdot \xi_{pq}} = \frac{\Phi_{IS} \cdot S_\Omega \cdot \Delta t_{IS}}{A_P \cdot \Delta t \cdot I^{IS}_{pq}} \tag{4.8}$$

where Φ_{IS} is the photon flux provided by the integrating sphere, S_Ω is the area of the integrating sphere that a pixel of the camera is effectively viewing, Δt_{IS} is the exposure time of the camera for the calibration frame, A_P is the area of the pinhole, Δt is the camera exposure time, and I_{pq}^{IS} is the number of counts in each pixel for the calibration frame.

4.3 Velocity-space tomography

The inverse problem is also of interest: given a measurement of the velocity space distribution in the scintillator Γ^S, we would like to retrieve the undistorted velocity space distribution of the absolute flux of fast-ion losses reaching the FILD head probe Γ^P, which is the physically relevant information. Combining the matrices from equation 4.7 we recover the matrix equation:

$$\sum_{kl} W_{ijkl}\Gamma_{kl}^P = \Gamma_{ij}^S \tag{4.9}$$

where the unknown is the velocity distribution of the fast-ion flux at the pinhole Γ_{kl}^P, whereas the other two quantities are known: the absolutely calibrated velocity space distribution measured at the scintillator Γ_{ij}^S and the weight function W_{ijkl}, which is a combination of the probability function and the efficiency function. The solution for Γ_{kl}^P in eq.4.9 is mathematically an ill-posed problem, analogous to the problem faced by velocity space tomography for other fast-ion diagnostics[152–157]. Therefore, the same inversion techniques can be used to solve it such as those described in [155]. In particular, the 0^{th} order Tikhonov regularization method has been implemented. In general, the Tikhonov regularization methods solve a minimization problem which can be expressed as:

$$F^* = \arg\min_F \left\| \begin{pmatrix} W \\ \lambda L \end{pmatrix} F - \begin{pmatrix} S \\ 0 \end{pmatrix} \right\|_2 \tag{4.10}$$

where W is a matrix composed of weight functions, S is the measurement matrix and F is the solution we seek. The upper row minimizes the two-norm residual of $S = WF$, while the lower row penalizes large values of the two-norm of λLF. The definition of the L matrix can then be done based on the properties of the solution F that we want to penalize. The regularization parameter λ controls the balance between the strength of the regularization condition and the goodness-of-fit to the data. Therefore, an optimal value for λ must be found. Different choices of the L matrix give name to the different Tikhonov methods. In the 0^{th} order Tikhonov regularization method, large absolute values of the solution F are penalized by choosing $L = I$, the identity matrix. Additionally, adding a non-negativity constraint to the regularization method [156] showed to improve the results of the inversion. The non-negativity constraint is trivially justified, since we know that the velocity space distribution is not negative. Some examples are shown in the following section.

4.3.1 Sensitivity study

The method described in the previous section has the potential to counteract the distortion of the velocity space in the detector, which can help the interpretation of the measurements. In order to assess the capabilities and limits of the technique, we

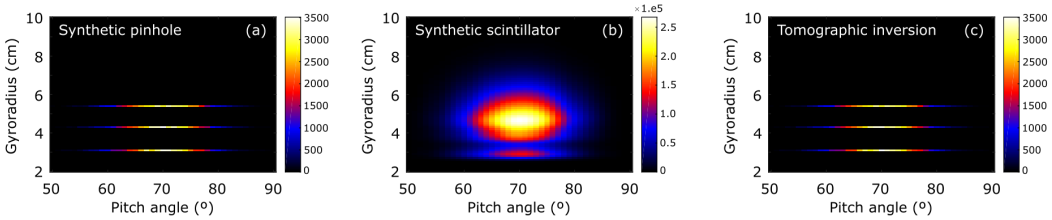

FIGURE 4.12: (a) Synthetic pinhole distribution used for the sensitivity study of the tomography. (b) Synthetic scintillator signal without noise. (c) Recovered pinhole distribution after applying the tomographic inversion. [139]

have carried out a sensitivity study by performing tomographic inversions to synthetic FILD data under different conditions.

For this study we will use a synthetic pinhole distribution consisting of three different mono-energetic distributions at $\rho_L = 3.1$, $\rho_L = 4.3$ and $\rho_L = 5.4$ cm with a certain spread in pitch angle. This is shown in Fig.4.12(a). Such a distribution mimics typical FILD data expected at AUG for the detection of first orbit NBI losses corresponding to the three energy components. As mentioned before, the 0^{th} order Tikhonov regularization method with non-negativity constraint will be used for the inversion.

As proof-of-principle, the synthetic FILD signal is first generated under idealized conditions, this is, without noise. The result is shown in Fig.4.12(b), where the expected synthetic signal in the scintillator is shown. It can be observed how the finite resolution of the instrument function smears out the signals corresponding to each of the different gyroradius components. Note also how the resolution in gyroradius becomes worse for larger gyroradii: the spot corresponding to $\rho_L = 3.1$ cm is clearly distinguishable, while the components $\rho_L = 4.3$ and $\rho_L = 5.4$ cm are not discernible and produce a single spot. After applying the tomographic inversion we are able to recover the undistorted velocity space at the pinhole, shown in Fig.4.12(c). This proof of principle test reveals the potential of the tomographic inversion technique to improve the energy resolution of the FILD measurements. However, the almost exact resemblance of the true solution and the inversion is only achieved in this idealized situation without noise.

We are now interested in evaluating the behaviour of the technique in a realistic case when considering noise in the signal. In FILD we can define the signal-to-noise ratio as $SNR = \frac{I_{max}}{<n>}$, where I_{max} is the maximum signal of a pixel in the measurement, and $< n >$ is the mean noise level, which in the FILD measurements is found to follow a Gaussian distribution due to the noise in the frames of the camera imaging the scintillator plate. Taking into account the dynamic range of the cameras used in the AUG FILD systems, the maximum SNR achievable, which would correspond to the limit case in which the center of the measured spot saturates, is of the order of $SNR \sim 200$. Following this estimate, different noise levels can be added to the synthetic FILD signal and to evaluate the tomographic inversions. This is shown in Fig.4.14, where the tomographic inversions for different noise levels corresponding to $SNR = 200, 100$ and 20 are shown. As the noise level is increased, the quality of the recovered pinhole distribution is lowered. However, the three different gyroradius distributions can be qualitatively observed in all the cases. It should be mentioned that in all of these inversions the selection of the optimal regularization

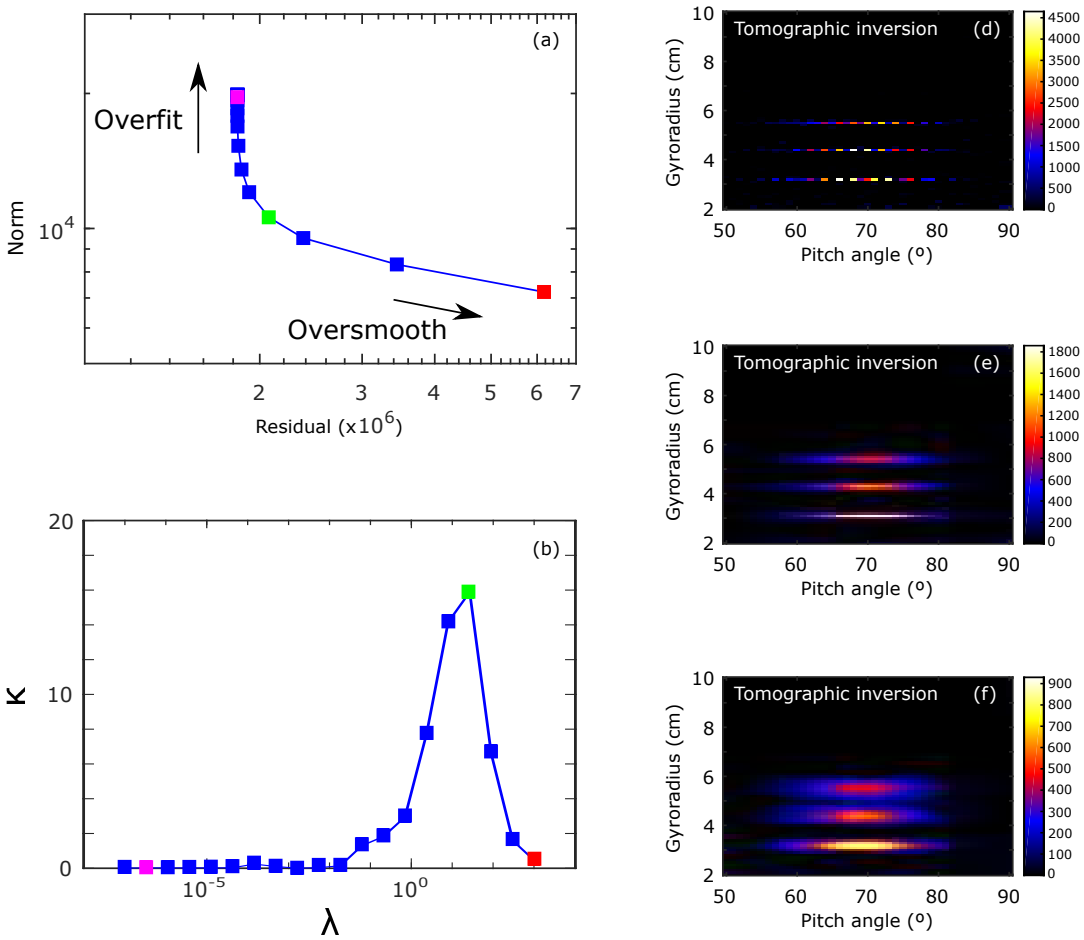

FIGURE 4.13: (a) L-curve plot representing the norm of the solution against the residuals. (b) Curvature of the L-curve as a function of the normalization parameter λ. (c), (d) and (e) show the tomographic inversion corresponding to the λ values indicated by the magenta, green and red squares respectively.

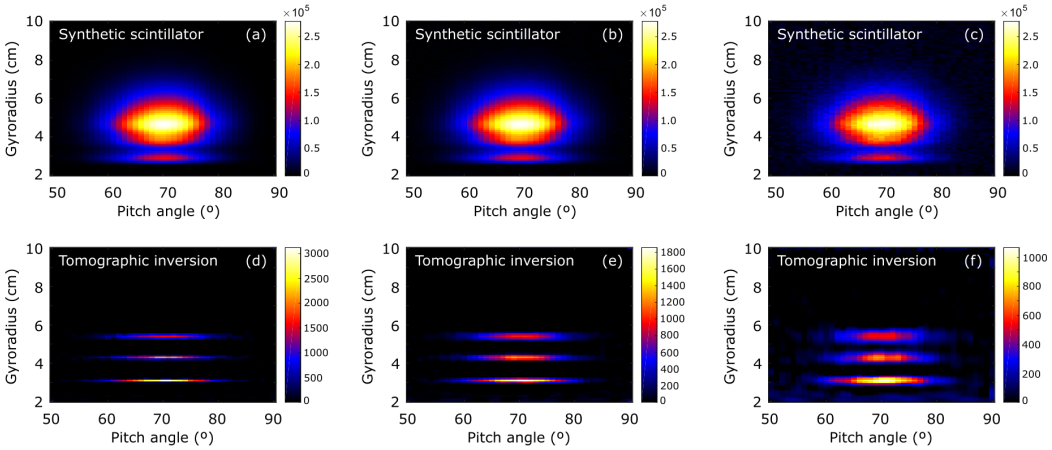

FIGURE 4.14: Synthetic scintillator signals with different noise levels of (a) $SNR = 200$, (b) $SNR = 100$ and (c) $SNR = 20$, and their corresponding tomographic inversions in (d), (e) and (f). [139]

parameter λ has been done through the L-curve method[155].

An example of such a method is shown in Fig.4.13, for the case corresponding to $SNR = 100$. Fig.4.13 (a) represents the norm of the solution against the norm of the residuals, for different values of the λ parameter. The solution is chosen to be the point at the maximum curvature of the L-curve, shown in Fig.4.13 (b), which represents a trade-off between an overfitting of the solution (left branch of the curve) and an oversmoothing of the solution (right branch of the curve). This is illustrated by Fig.4.13 (c), (d) and (e), which represent solutions of the tomographic inversion for different parameters of λ, corresponding to the magenta (overfit), green (optimal) and red (oversmooth) squares.

It is also of interest to evaluate if the inversion is able to distinguish between energy spread distributions and monoenergetic components. This is motivated by the fact that NBI first orbit losses are routinely measured by the FILD systems, which by definition are measured as monoenergetic distributions with energies corresponding to the NBI injection systems. To investigate this several simulations are performed in which the spot at $\rho_L = 5.4$ cm is changed and its spread in energy is increased, assuming deuterium ions and a local magnetic field of $B_{FILD} = 1.4$ T. The results are shown in Fig.4.15 in which a noise of $SNR = 200$ was set. Three different cases have been studied in which the energy spread of the population centered at around $\rho_L = 5.4cm$ was increased to $\sigma_e = 10\ keV$ (a,d,g), $\sigma_e = 20\ keV$ (b,e,h) and $\sigma_e = 50\ keV$ (c,f,i). The first row shows the input distributions at the pinhole. The second row shows the corresponding synthetic scintillator signals. By looking at these only slight differences can be noticed, which would not be enough to identify a difference in the energy distribution of the lost ions. The third row shows the results of the tomographic inversion. By looking at Figs.4.15 (g-i), one can clearly identify a difference in the energy distribution of the population centered at $\rho_L = 5.4$ cm. However, as the energy spread is increased, the inverted distribution loses its capability to localize the individual peaks in energy and the retrieved distribution is smoothened out. Thus, the tomography is in fact able to distinguish a (nearly) mono-energetic population from an energy-spread population.

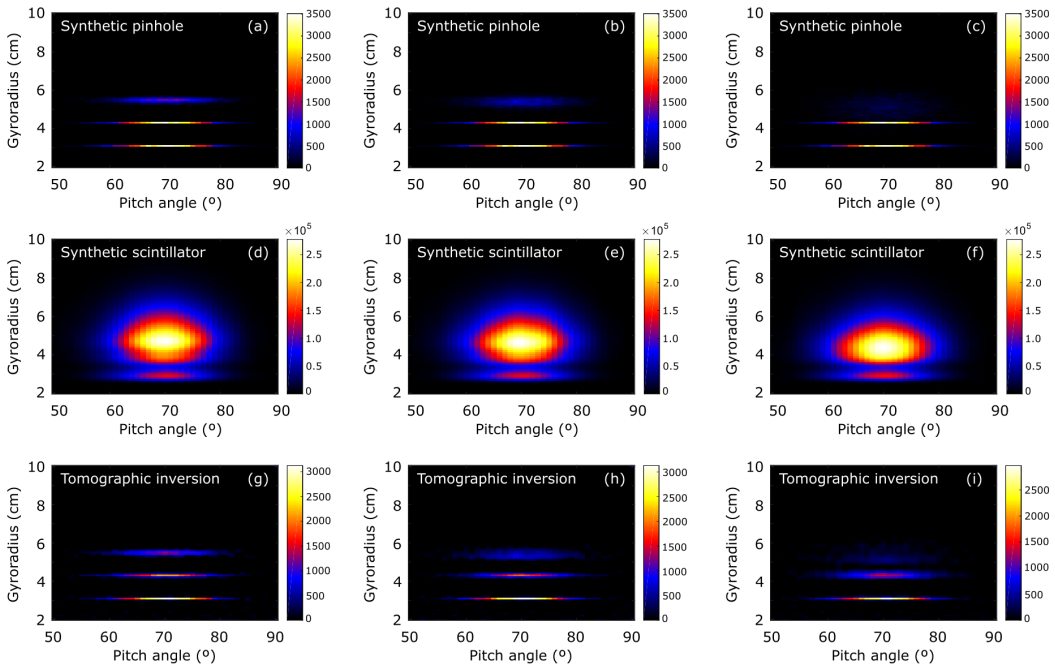

FIGURE 4.15: Tomographic inversion of synthetic FILD signals with different energy spreads of $\sigma_e = 10\ keV$ (a,d,g), $\sigma_e = 20\ keV$ (b,e,h) and $\sigma_e = 50\ keV$ (c,f,i), assuming deuterium ions and a local magnetic field of $B_{FILD} = 1.4$ T. (a-c) show the synthetic pinhole distribution. (d-f) show the synthetic scintillator signal. (g-i) show the tomographic inversion. [139]

The last check consists of evaluating the energy resolution of the tomography, i.e: the capability of the technique to disentangle different monoenergetic distributions. To this end, the distribution at $\rho_L = 5.4$ cm is moved closer to the distribution at $\rho_L = 4.3$ cm. A scan has been performed by positioning the distribution at $\rho_L = 4.5$ cm (a,d,g), $\rho_L = 4.7$ cm (b,e,h) and $\rho_L = 4.8$ cm (c,f,i), illustrated in Fig.4.16. Again, the first row shows the input distribution at the pinhole, the second row shows the synthetic scintillator signal, and the third row shows the tomographic inversions. By looking at the synthetic scintillator signals almost no difference can be appreciated between the three cases. However, the tomographic inversion of these signals does reveal these differences, although there is a limit in the gyroradius of the distribution that the tomography is able to fully disentangle.

4.4 Benchmark of the model

The model has been implemented in the FILDSIM code for the analysis of FILD signals and has been tested with data from the ASDEX Upgrade FILD detectors. The workflow of the code is shown in Fig.4.17, where the different functionalities previously described are schematically represented. The first module is used to carry out the trajectory calculations providing the relevant information needed to build the diagnostic probability function. A second module is used to build the full weight function, including the scintillator efficiency through the application of the Birk's model, which is needed for both building synthetic FILD signals and retrieving the

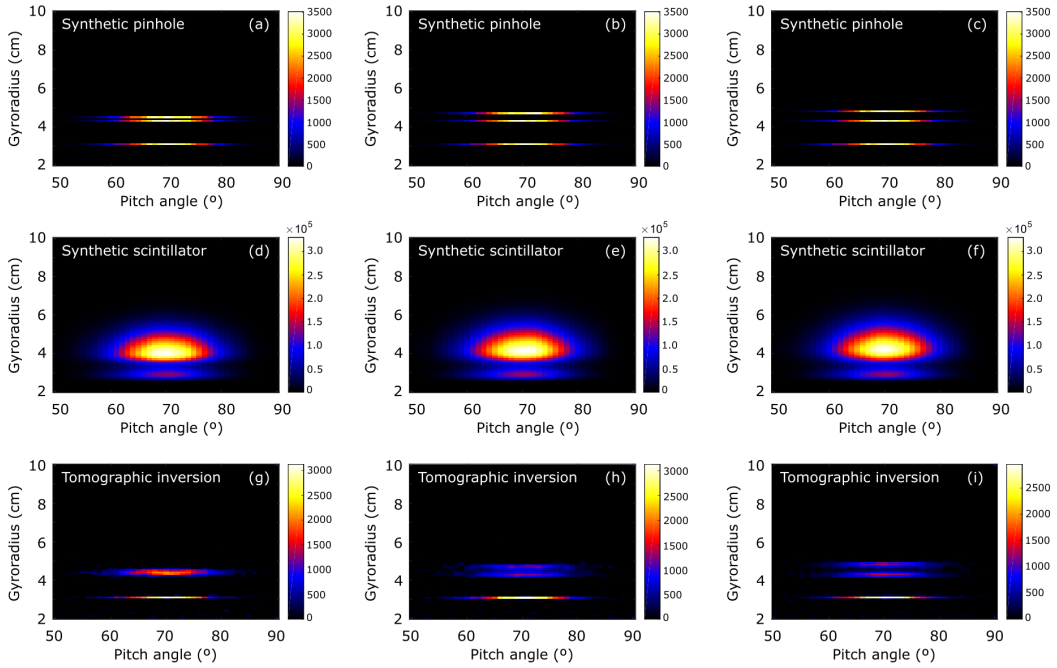

FIGURE 4.16: Tomographic inversion of synthetic FILD signals with different gyroradius separations of $\Delta\rho = 0.2$ *cm* (a,d,g), $\Delta\rho = 0.4$ *cm* (b,e,h) and $\Delta\rho = 0.5$ *cm* (c,f,i). (a-c) show the synthetic pinhole distribution. (d-f) show the synthetic scintillator signal. (g-i) show the tomographic inversion. [139]

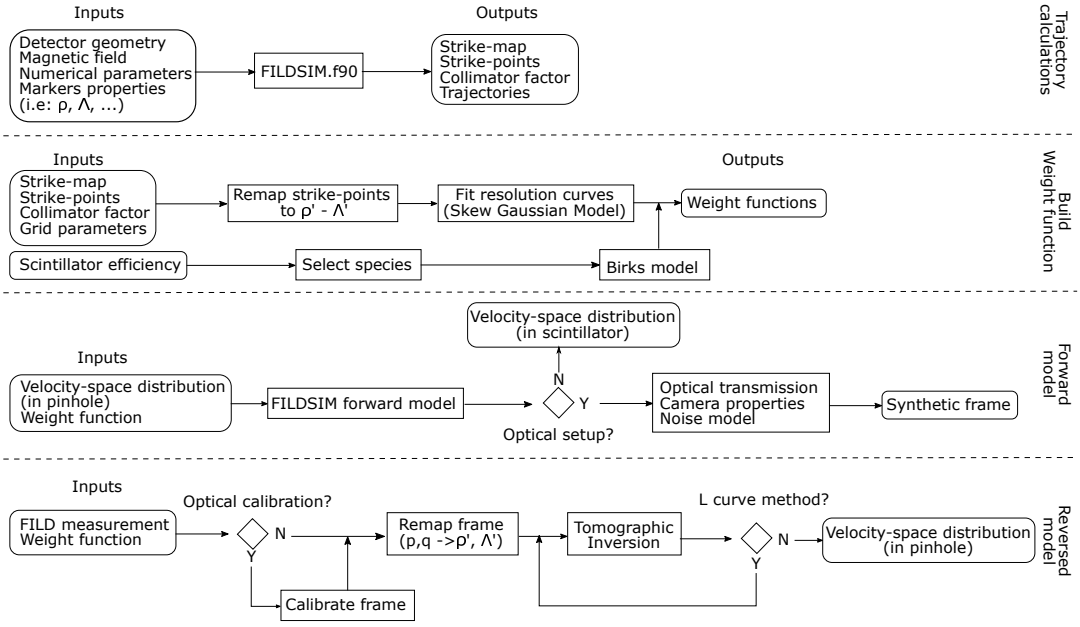

FIGURE 4.17: Workflow of the FILDSIM code. [139]

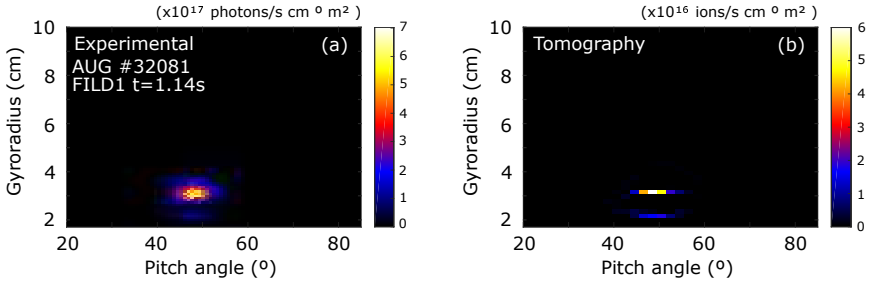

FIGURE 4.18: (a) Photon flux emitted by the scintillator revealing the velocity space of fast-ion losses measured by FILD1 in AUG #32081 at t=1.14s. (b) Retrieved velocity space of the losses at the FILD pinhole after applying the tomographic inversion to the FILD experimental signal. [139]

undistorted velocity-space distribution at the pinhole from experimental measurements.

We have selected the signal from FILD1 in AUG shot #32081 at t=1.14s for the benchmarking of the model. The FILD experimental signal is shown in Fig.4.18(a), where the velocity space of the losses measured in the scintillator can be observed. Two different spots at $r_L \sim 3.5$ cm and $r_L \sim 2.5$ cm are measured. These are identified as first orbit losses corresponding to the main and half energy component of the NBI source Q7 respectively. The one-third energy component of the NBI ions is blocked by the collimator due to its small gyroradius, and is therefore not measured. After applying the tomographic inversion to the experimental FILD signal, the undistorted velocity space of the fast-ion losses at the FILD pinhole is retrieved (Fig.4.18(b)). Two distributions are obtained with a spread in pitch angle ranging from 40° to 60° and very well defined gyroradii of 3.4 and 2.4 cm. It is worth noticing that these distributions are effectively single energy components and not slowed down energy distributions, as it is expected for the beam ion prompt losses. The deuterium NBI main and half energy components are 93 and 46.5 keV corresponding to gyroradii of 3.2 and 2.3 cm respectively, given the magnetic field at the FILD probe position of 1.93 T. This small discrepancy between the tomographic reconstruction and the expected values of Larmor radii can be due to a misalignment of the strike map. The measured absolute heat flux of these fast-ion losses is $\sim 1.45 kW/m^2$.

Thus, the use of the tomographic inversion technique has been demonstrated to improve the analysis and interpretation of FILD signals, by potentially revealing additional details of the velocity-space distribution of the lost ions, which is fundamental for the study of the velocity-space dynamics of fast-ion losses induced by MHD instabilities.

Chapter 5

Experimental results

In this chapter the main physics results of this thesis are described. These can be divided into two main investigations: first, the measurement of the velocity-space resolved absolute flux of ICRF accelerated fast-ion losses in the presence of a tearing mode. Second, the study of the velocity-space dependency of fast-ion losses during edge localized modes. This study has been possible due to the unprecedented characterization of the FILD detector, which has revealed the importance of mode-particle resonant transport mechanisms.

5.1 Velocity-space resolved absolute flux measurement of ICRF accelerated fast-ion losses due to a tearing mode

The experiment presented here has been performed in the ASDEX Upgrade tokamak with a plasma current $I_p = 1$ MA and a magnetic field $B_t = 2.36$ T. 2.5 MW of NBI heating with a main injection energy of 60 keV are applied in three different phases: 0.3-1.0 s, 2.0-3.0 and 4.0-4.7 s. 4 MW of ICRF-heating are applied at 4.5 s with a frequency of 30 MHz corresponding to the hydrogen minority heating and deuterium second harmonic heating. The hydrogen content in the deuterium plasma is around 5% as estimated by neutral particle analyzer (NPA) measurements. In Fig.5.1 an overview of the relevant phase of the discharge is shown. The plasma density increases up to $3 \cdot 10^{19} m^{-3}$ when the NBI is turned on at 4.0 s. When the ICRH is switched on at 4.5 s the FILD1 signal increases dramatically during a time window of 100 ms. The temperature in the FILD1 head probe, placed at 5 cm from the separatrix, is measured by an infra-red camera. It increases up to 1200 ^oC and is then damaged leading to the discharge termination due to radiative collapse.

Here, the focus is put on the measurements provided by the FILD1 detector located near the ASDEX Upgrade midplane at $z = 0.3$ m. An infra-red camera with a frame rate of 2 kHz measures the heat flux on different points of the FILD1 head (Fig.5.2) [115]. The temporal evolution of the heat load on the detector head at the approximate position of the collimator pinhole is shown in Fig.5.3. Before the ICRH phase the heat load stays below 5 MW/m^2. As soon as the ICRH is switched on, the heat load increases peaking at around 30 MW/m^2. At 4.63 s the FILD1 head probe is damaged as illustrated in Fig.5.2. A dramatic increase of the FILD1 signal is observed in Fig.5.3 (c).

A fast CMOS camera provides a good spatial resolution for the identification of the velocity-space of the losses with a time resolution of 1 ms. Fig.5.4 (a) shows the measurement shortly before the ICRH phase. A spot corresponding to particles with energy $E = 60keV$ and pitch angle $\Lambda = cos^{-1}(v_{\|}/v) \approx 60^{\circ}$ is identified as NBI

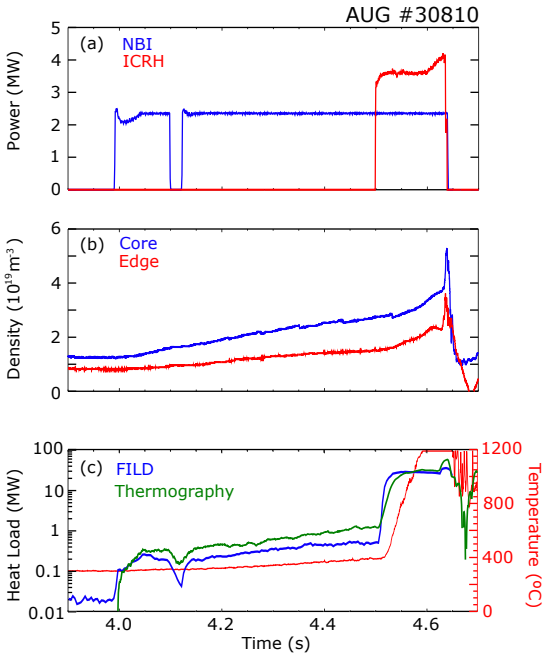

FIGURE 5.1: Timetraces of AUG shot #30810 during the time window of interest. (a) NBI power is shown in blue and ICRF power is shown in red. (b) Line integrated density in the core (blue) and in the edge (red). (c) Fast ion heat load measured with FILD1 is plotted in blue. The heat load measured by the thermography is plotted in green. The temperature in the head probe is plotted in red. [151]

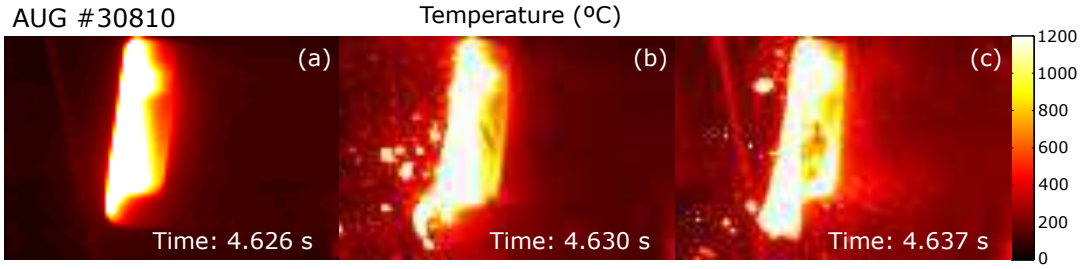

FIGURE 5.2: Infrarred camera frames showing the FILD1 head temperature at $t = 4.626\ s$ (a) just before the FILD1 head probe is damaged, and at $t = 4.630\ s$ (b) and $t = 637\ s$ (c) just after it. [151]

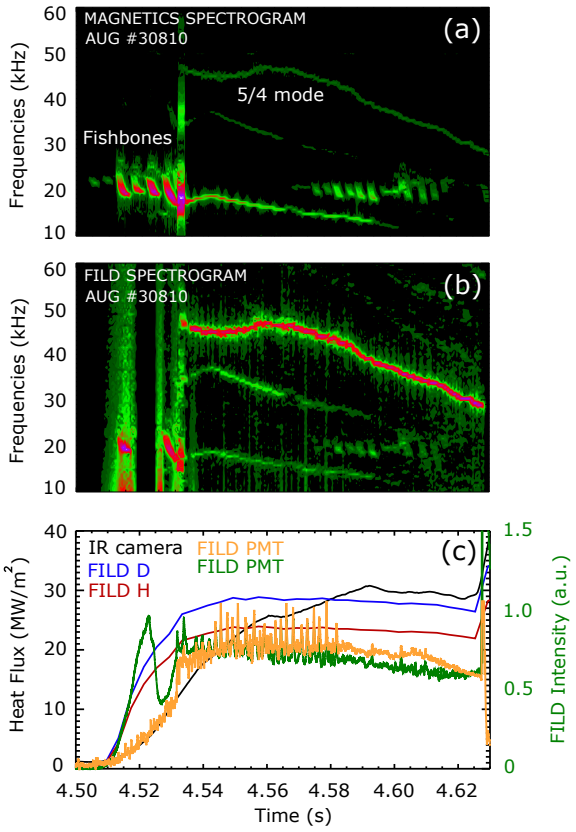

FIGURE 5.3: (a) Spectrogram of a magnetic pick-up signal at the time window corresponding to the ICRH phase. The spectrogram reveals the MHD activity in the plasma. (b) Spectrogram of FILD1 signal taken from a PMT. A clear correlation is observed with the MHD activity measured by the magnetic signal. (c) Time trace of the heat flux measured by the infrared camera (black), the fast-ion heat flux measured by the FILD1 detector from the CMOS camera signal assuming hydrogen ions (red) and deuterium ions (blue) and the FILD1 signal of two different photomultiplier channels (green and yellow). [151]

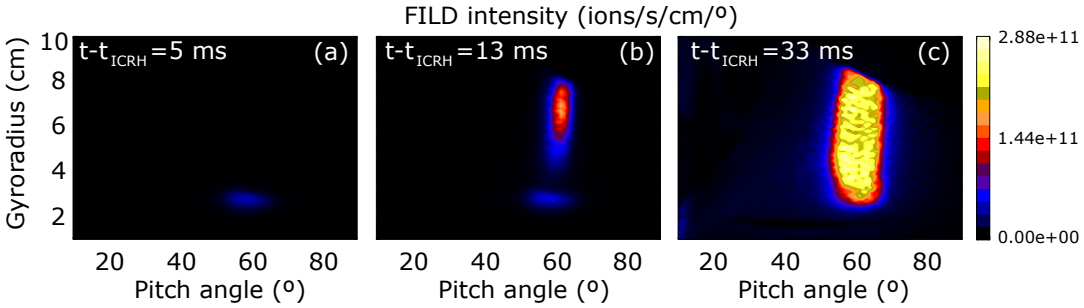

FIGURE 5.4: Time evolution of the velocity space resolved absolute flux of fast ion losses in the scintillator measured with FILD1 (i.e: without including the collimator factor). (a) Shows the velocity space 5 ms prior to the ICRH phase. A spot corresponding to the NBI prompt losses at $r_L = 3.0\ cm$ and $\Lambda = 60^o$ is observed. (b) Shows the velocity space 13 ms after the ICRH is turned on. A new spot corresponding to ICRH accelerated fast ions is observed with Larmor radius around 6 cm and $\Lambda = 60^o$. (c) Shows the velocity space 33 ms after the ICRH is turned on. The spot corresponding to ICRF accelerated ions has fully developed. [151]

prompt losses. In Fig.5.4 (b) the fast ion losses corresponding to ICRF heated ions start to be measured at larger gyroradii around 13 ms after the ICRH is turned on, with the spot centered at around $r_L = 6cm$. These correspond to energies of around 500 keV in the case of hydrogen ions and 250 keV in the case of deuterium ions. In Fig.5.4 (c), 33 ms after the ICRH is turned on, the velocity space distribution has evolved and the fast-ion losses have increased.

The absolute calibration of the FILD systems in AUG allows the estimation of the fast-ion flux at the collimator pinhole [148]. The full characterization of the scintillating material together with the calibration of the FILD1 light acquisition system permits to estimate the flux of ions striking in the scintillator plate based on the CMOS camera measurements. The collimator factor, i.e: the fraction of ions that are blocked by the collimator, is calculated using the FILDSIM code. This way, the absolute flux of fast-ions in the FILD1 pinhole can be calculated as $\Gamma_{pinhole} = \Gamma_{scintillator}/f_{col}$.

The fast-ion heat load measured by FILD1 (red and blue) is consistent with the infrared camera measurements (black) as shown in Fig.5.3 (c), indicating that the heat load is mostly coming from fast ion losses. The signal corresponding to two PMT channels (green and yellow) are plotted. The timetraces of these two signals are slightly different since they correspond to different regions of the velocity space of the losses. The FILD1 fast-ion heat load is obtained by integrating the CMOS camera signal in the whole velocity space of the losses. For $t > 4.53$ s some pixels of the CMOS camera in the region of interest saturate and therefore the fast-ion heat load measured by FILD represents only a lower boundary.

The FILD diagnostic by itself is not able to distinguish between different ion species. For this reason the fast-ion heat load measured with FILD1 has been evaluated assuming both, hydrogen (red) and deuterium (blue) ions. The estimated fast-ion heat load is similar in both cases, it is only around 20% smaller in the case of hydrogen ions. The reason for not having a large discrepancy is that the difference in the measured energy of both species is compensated by the difference in the light

yield of the scintillator. In other words, the fast-ion heat load measured with FILD can be expressed as:

$$P_{FILD} \propto \Gamma_{scint} \frac{E}{\xi} \tag{5.1}$$

where Γ_{scint} is the photon flux emitted by the scintillator, E is the energy of the ions and ξ is the scintillator yield, this is, the number of photons emitted per incident ion, which is a function of the particle energy and species. Despite the energy of the measured hydrogen (500 keV) being larger than the energy of the measured deuterium (250 keV), the scintillator yield for hydrogen at 500keV is also larger than the scintillator yield for deuterium at 250keV.

It can be noticed that the FILD1 signal increases faster than the IR camera signal. This can be explained in terms of the difference in response times for both diagnostics. The IR camera measurement is based on the temperature increase of the FILD1 head probe, which is naturally subject to some thermal inertia. On the other side, the FILD measurement is based on the scintillator light emission, which is a process with characteristic times of the order of 10^2 ns.

5.1.1 Fast-ion losses induced by MHD activity

An intense MHD activity in the plasma is observed in the spectrogram obtained with magnetic pick-up coils (Fig.5.3(a)). As soon as the ICRF is switched on at 4.5 s fishbone activity is observed, leaving its characteristic footprint in the spectrogram as a frequency chirp at around 20 kHz. At 4.53 s a sawtooth crash takes place which triggers several internal modes at a frequency of 45 kHz, 35 kHz and 20 kHz approximately. This kind of event has been already reported in AUG [158]. At 4.58 s fishbone activity is again observed. Looking at the FILD spectrogram in Fig. 5.3(b) a clear correlation with the MHD activity present in the plasma can be seen. This is indicative of an interaction between the MHD modes and the fast-ion population, leading to enhanced fast-ion radial transport and loss. The mode contributing most intensely to the fast-ion losses is the one starting with a frequency of 45 kHz and sweeping down to 33 kHz at 4.62 s. This mode is found to be a tearing type by means of the 1D standard electron cyclotron emission (ECE) diagnostic available in AUG, which consists of a 60 channels heterodyne radiometer with a sampling rate of 1 MHz and a spatial resolution of $\sim$ 12 mm [105]. The method described in [158] allows to discern between kink and tearing type modes by identifying phase shifts in the timetrace of the ECE signal measuring at the resonant surface. The poloidal and toroidal mode numbers have been identified as m=5 and n=4 respectively by means of the magnetic pick-up coils and the soft X-ray (SXR) diagnostic. The perturbation is localized near the q=1.25 surface which is in agreement with the 2D-tomographic SXR reconstruction of the mode, as shown in Fig.5.5. On the other hand, the mode starting at a frequency of $\sim$ 20 kHz and sweeping down to $\sim$ 15 kHz is found to be a core $m/n = 1/1$ mode by means of the magnetic pick-up coils and also in agreement with the SXR tomography, while the other coherent mode, sweeping in frequency from $\sim$ 35 to $\sim$ 30 kHz is a higher harmonic of the latter one.

The proposed mechanism underlying the enhanced fast-ion losses is a resonant interaction between the MHD and the fast particles. Particles fulfilling the resonant

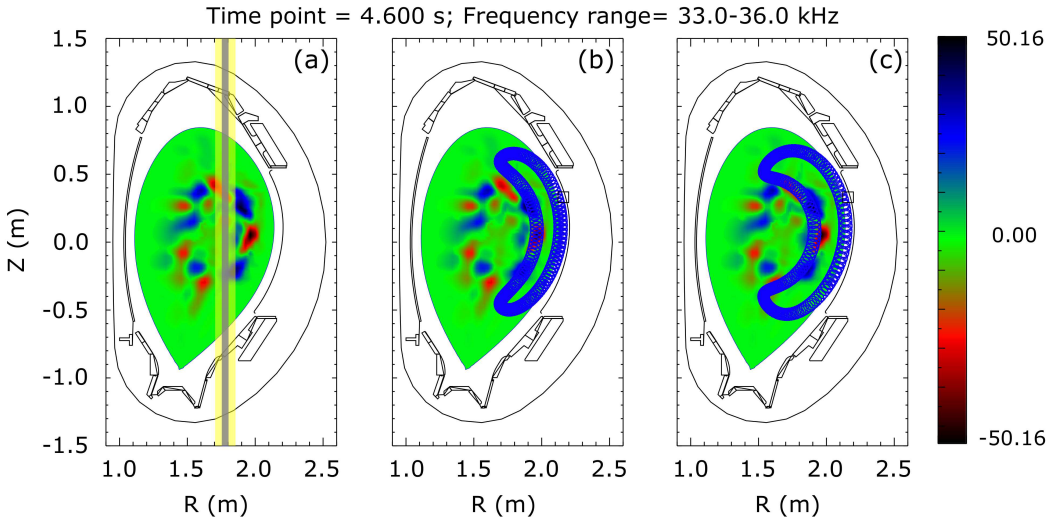

FIGURE 5.5: Poloidal view showing the tomographic reconstruction of the 5/4 tearing mode by means of the SXR diagnostic. In (a) the ICRF resonance layers for hydrogen and deuterium are overlayed in blue and yellow respectively. In (b) an orbit corresponding to a deuterium ion at 250 keV backtraced from the FILD1 detector is shown. In (c), the same for a hydrogen particle at 500 keV. It can be noticed that both trajectories overlap with the spatial structure of the mode. [151]

condition may experience an exchange of momentum and energy with the wave [41, 90]:

$$\Omega_{n,p} = n\omega_\phi - p\omega_\theta - \omega_{MHD} = 0 \tag{5.2}$$

Here, n is the toroidal mode number, p the poloidal harmonic, ω_ϕ the toroidal precession frequency, ω_θ the poloidal bounce frequency and ω_{MHD} the MHD mode frequency, where all the frequencies are considered in the laboratory frame. A more detailed analysis of the FILD1 photomultiplier signal imaging the region corresponding to the ICRF losses reveals a linear dependence between the intensity of the coherent fast-ion losses and the magnetic perturbation at the corresponding mode frequencies, shown in Fig.5.6. This is consistent with the fact that the wave-particle momentum exchange in the resonance is proportional to the perturbation amplitude δB, indicating the convective nature of this transport mechanism [41, 44]. The ratio between the amplitude of the FILD signal at the mode frequency and the total signal shows that the convective losses due to the 5/4 tearing mode constitute 9.3 ± 0.7 % of the measured fast-ion losses, which corresponds to approximately 3 MW/m^2. The other two coherent modes contribute to the total FILD signal by less than 2 %. However, in addition to the coherent fast ion losses, an overlapping of resonances in the particle phase space can lead to increased fast ion losses via stochastic diffusion [41]. Given the presence of multiple MHD modes and the size of the fast ion orbits shown in Fig.5.5, it is likely that the ICRH accelerated ions interact simultaneously with the multiple MHD modes, thus leading to orbit stochasticity and diffusion. Finite Larmor Radious (FLR) effects are, however, not discussed as they would require expensive simulations that are beyond the scope of this work. These stochastic losses appear in the FILD signal as an incoherent component which cannot be directly distinguished from the prompt fast-ion losses. An estimation for the

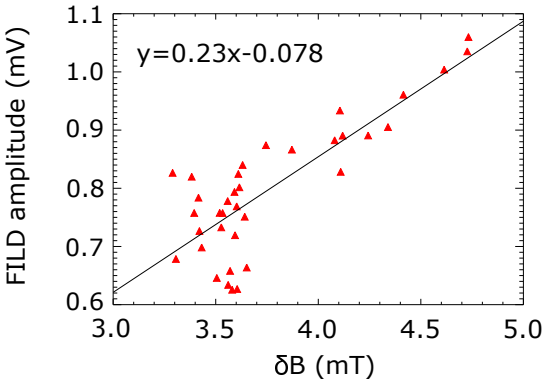

FIGURE 5.6: Amplitude of the FILD1 signal against the amplitude of the magnetics signal at the frequency corresponding to the 5/4 tearing mode. A linear correlation is observed. [151]

latter can be provided by modelling.

5.1.2 Modelling

In order to model the fast ion losses in the presence of ICRF heating, the power coupled to the plasma using the PION code [159] has been calculated. The power split obtained with PION shows that around 73% of the coupled power corresponds to hydrogen damping, 20% to second-harmonic deuterium damping and 7% to direct electron damping. This is in agreement with the ICRF coupled power calculated with TRANSP-TORIC as shown in Fig.5.7. To build the fast-ion distribution function, PION introduces a simple model [160] which reproduces the "rabbit-ear" feature typical for ICRH fast-ion distributions [161]:

$$f_0(v,\xi,\psi) = F(v,\psi)\cdot C(v,\psi)\cdot\left\{exp\left[-\left(\frac{\xi-\xi_R(\psi)}{\Delta\xi(v,\psi)}\right)^2\right]+ \right. \\ \left. + exp\left[-\left(\frac{\xi+\xi_R(\psi)}{\Delta\xi(v,\psi)}\right)^2\right]\right\} \quad (5.3)$$

where v is the particle velocity, ξ is the pitch angle of the particle orbit in the outer midplane and ψ is the poloidal magnetic flux function. $F(v,\psi)$ is the pitch angle averaged distribution function, $C(v,\psi)$ is a normalisation constant such that the flux surface averaged density is consistent with the pitch angle averaged distribution, ξ_R is the pitch angle in the outer midplane of a particle whose turning points are at the resonance layer, and $\Delta\xi$ is a parameter that controls the width of the "rabbit ears". In order to estimate $\Delta\xi$ we assume that:

$$\eta^2_{eff}(v) = \frac{1}{2}\int \eta^2 f_0(v,\xi(\eta,\psi,\theta_R),\psi)d\eta \quad (5.4)$$

where η is the pitch angle of the particle evaluated at the resonance point, meaning that θ_R corresponds to the position where $\omega = n\omega_{ci}(\psi,\theta_R)$. As a rough approximation we take η^2_{eff} to have the same functional form as μ^2_{eff} in Ref.[159].

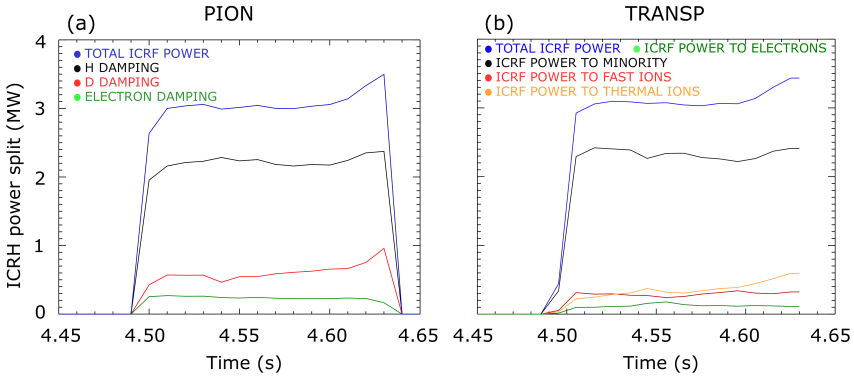

FIGURE 5.7: ICRF power coupled to the different species present in the plasma simulated with PION (a) and with TRANSP-TORIC (b). The results given by both codes are in good agreement. Most of the power (73%) is transferred to hydrogen ions, 20% is transferred to deuterium via second harmonic heating, and around 7% is transferred to electrons. In the PION simulation (a), the power transferred to deuterium ions is indicated in red. This includes both, the power transferred to thermal deuterium and to fast deuterium ions, which are present in the plasma due to neutral beam injection. In the TRANSP simulation (b), the power transferred to deuterium is explicitly separated into thermal species (orange) and fast ions (red). [151]

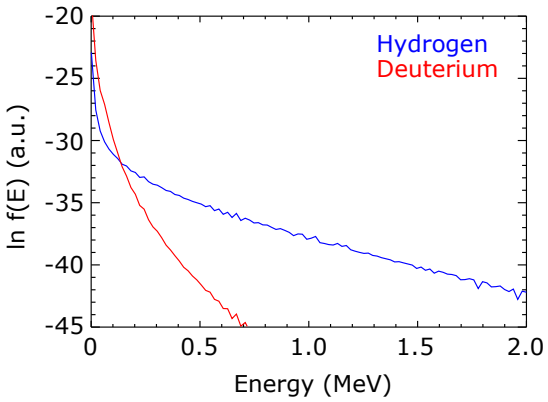

FIGURE 5.8: Energy spectrum of ICRF accelerated hydrogen (blue) and deuterium (red) calculated with PION. [151]

The energy spectra for both, hydrogen and deuterium species calculated with PION is shown in Fig.5.8. It can be seen that the amplitude of the high energy tail is larger for hydrogen ions than for deuterium ions. Since most of the power is coupled to the hydrogen ions, focus will be put on these in the modelling of the fast ion losses.

Provided the hydrogen fast-ion distribution calculated with PION, the orbit following code ASCOT [149] has been used to calculate the contribution to the fast-ion heat load in the FILD head probe due to prompt losses, as well as the velocity space of these. The computation of the fast-ion heat load with ASCOT has been validated for NBI prompt losses in previous works[148]. ASCOT includes a realistic 3D model for the vessel wall and the geometry of the FILD detector. In this case the simulations were carried out in full-orbit and 10^6 Monte Carlo markers were followed during 1 ms. The toroidal field ripple was included in the magnetic equilibrium, but no internal MHD perturbation was considered in the simulation.

For a direct comparison with the experimental measurements, a synthetic FILD signal is built by applying the FILDSIM code to the velocity space distribution of the losses given by ASCOT in the FILD1 head. The velocity space distribution of the ions reaching the FILD1 head simulated with ASCOT is shown in Fig.5.9 (a), while Fig.5.9 (b) shows the synthetic FILD1 signal after applying the FILDSIM model. The difference in the amplitude of the velocity space fast ion distribution between Figs.5.9 (a) and (b) is due to the effect of the collimator factor, which takes into account the ratio of particles that are blocked by the 3D collimator geometry. The simulated velocity space of the losses is in fairly good agreement with the FILD1 measurement (Fig.5.4 (c)). It can be observed that the calculated ASCOT distribution includes a set of ions with low energies ($\rho_L < 2\ cm$ and $60^o < \Lambda < 80^o$) which are not measured by FILD. This is reproduced by the synthetic signal since these particles are blocked by the collimator due to their small Larmor radius. On the other hand, the heat-load in the FILD1 head probe obtained with ASCOT due to prompt fast ion losses including the effect of the toroidal field ripple is around 2.5 MW/m^2. This is well below the total heat load measured experimentally. It should be noticed that the total fast ion heat load is a sum of different contributions: fast-ion prompt losses, convective losses due to a direct interaction between the fast-ions and individual MHD modes and diffusive losses due to the overlapping of phase space resonances in the presence of single or multiple MHD modes. The ASCOT simulation gives an estimate of the first of these terms, therefore highlighting the importance of the convective and diffusive losses induced by the MHD activity. The modelling of the fast-ion losses including the MHD activity of this discharge is left for future work.

The velocity space of the resonances between fast ions passing through the FILD1 detector and the 5/4 mode have been calculated by following the orbits backwards in time started at the FILD1 detector position. The resonance lines are shown in Fig.5.10, where the pitch angle and the gyroradius are evaluated at the FILD1 position. These represent the orbits fulfilling the resonant condition $\Omega_{n,p} = n\omega_\phi - p\omega_\theta - \omega_{MHD} = 0$. The different branches observed in the figure correspond to different values of the poloidal harmonic p. The resonance line associated to $p = -2$ overlaps with the FILD1 measurement.

The calculation has been performed for both, hydrogen and deuterium ions. The resonance lines are different for both species if plotted in the energy-pitch angle space. However, as it has been stated before, the FILD detector does not measure

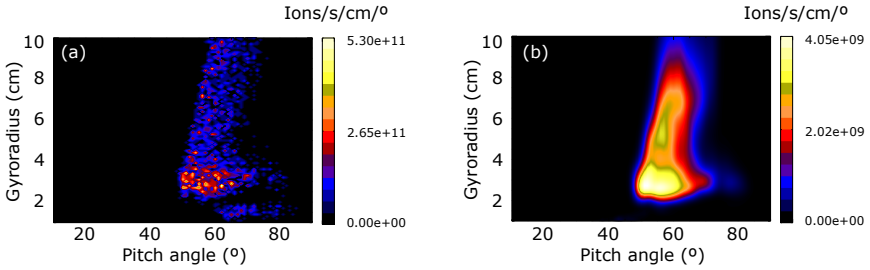

FIGURE 5.9: Simulated velocity space of the losses in the FILD1 detector. (a) Fast-ion distribution in the FILD1 head calculated with ASCOT using as input an ICRF distribution calculated with PION. (b) Synthetic FILD1 signal obtained after the application of the FILDSIM code. The result is in good qualitative agreement with the experimental measurement. [151]

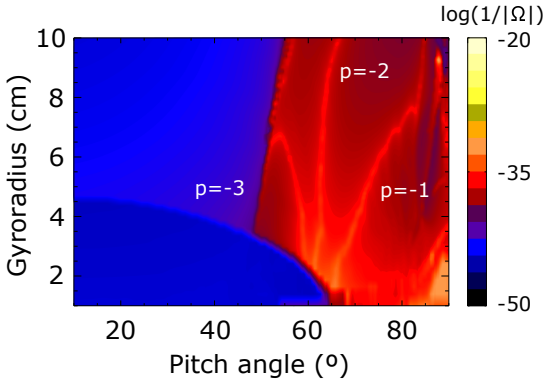

FIGURE 5.10: Velocity space of the resonances for fast-ion orbits at the FILD1 detector position. The different resonance lines correspond to different values of the poloidal harmonic p. [151]

the energy directly but the Larmor radius of the particle. Due to the mass difference between both species, the resonance lines overlap when mapping them from energy to Larmor radius, given the magnetic field at the FILD position.

5.2 Acceleration of beam-ions measured during ELMs

In this section time resolved velocity-space measurements of ELM induced fast-ion losses in the ASDEX Upgrade tokamak are presented. Previous works had reported on an increased level of fast-ion losses during ELMs [19], however, for the first time the intra-ELM velocity space evolution of these losses is presented.

The experiments used for this analysis were performed in deuterium plasmas with low density ($n_e \leq 6 \cdot 10^{19}\ m^{-3}$), low pedestal collisionality ($\nu^* \leq 0.4$) and $\beta_N = \beta \frac{aB_t}{I_p} \sim 2.5$, where β is the volume averaged toroidal plasma-to-magnetic pressure ratio (in %), a is the minor radius of the tokamak (in m), B_t is the toroidal magnetic field (in T) and I_p the plasma current (in MA). The experiments were performed in a variety of scenarios with a plasma current ranging from $0.6 - 1.0$ MA and a toroidal magnetic field ranging from $1.8 - 2.5$ T, in which the only external sources of fast-ions to the plasma were the neutral beam injection (NBI) systems.

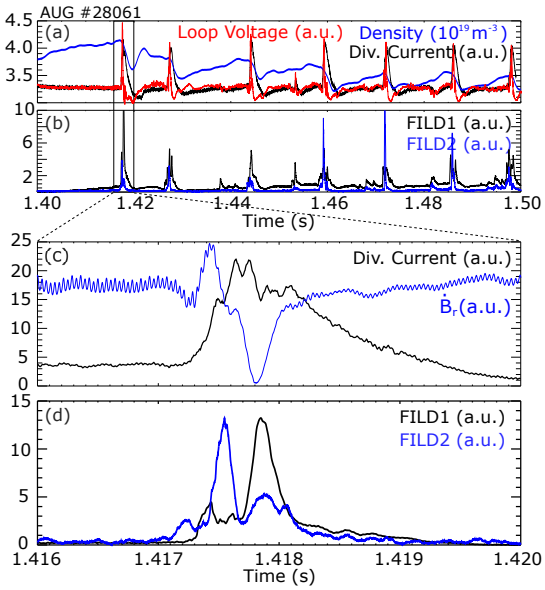

FIGURE 5.11: (a) Timetraces of the electron density (blue), the loop voltage (red) and the divertor current (black), which is used as an ELM monitor. (b) Timetraces of two different FILD detectors, located at the same poloidal position but toroidally displaced. (c) and (d) show a zoom into a single ELM. [162]

Fig.5.11(a) shows timetraces of the density (blue), the divertor current, which is used as an ELM monitor in AUG (black), and the loop voltage (red). Fig.5.11(b) shows the signal of FILD1 and FILD2 which are located at the same poloidal position ($z \sim 0.3$ m) but at different toroidal positions. Different ELM crashes with typical timescales of ~ 1 ms can be observed during which the divertor current increases rapidly, the density collapses and the fast-ion losses measured by both FILD systems increase. Spikes in the loop voltage signal are also observed during ELMs, which are indicative of the appearance of transient electric fields. A zoom into an individual ELM crash is shown in Figs.5.11(c) and (d), where the timetrace of the associated magnetic perturbation is also plotted. The first thing to notice is the filamentary-like behaviour of the FILD signals, in which multiple spikes with characteristic times on the order of $\sim 100\mu$s are observed within a single ELM crash. The second thing to notice is that the time evolution of these fast-ion filaments is different for the two FILD detectors, thus revealing the 3D nature of the phenomenon. Given that FILD measurements correspond to beam-ions which are born in the edge of the plasma, the deeper deposition in the NBI birth profile due to lower densities during the ELM crash [19] suggests that the increased fast-ion losses are likely to be produced by the perturbation fields associated with the ELM.

5.2.1 Velocity space of ELM induced fast-ion losses

The use of a fast CMOS camera, with a time resolution of ≥ 1 kHz, enabled the possibility of carrying out time-resolved velocity space measurements of fast-ion losses during the ELM crash. FILD measurements are shown in Fig.5.12, which corresponds to AUG FILD1 data during shot #33127at 4.354 s. Here a set of two populations can be observed at two main pitch angles of $\sim 45^\circ$ and $\sim 60^\circ$. These

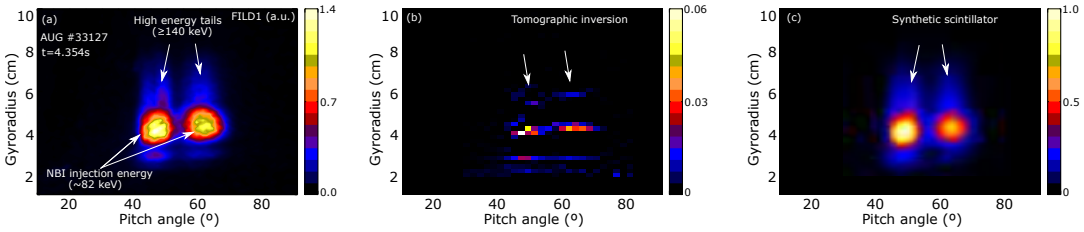

FIGURE 5.12: (a) Velocity space measurement of fast-ion losses performed with FILD1 during an ELM in AUG #33127. (b) Undistorted velocity space of the fast-ion losses reaching the detector pinhole, as a result of the application of the tomographic inversion. (c) Synthetic scintillator signal retrieved from the tomography. The location of the high-energy feature is indicated by white arrows. [163]

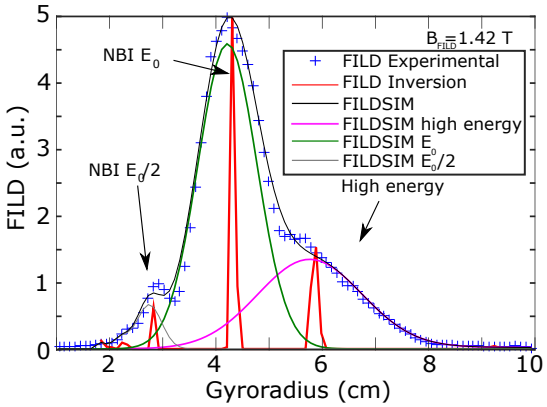

FIGURE 5.13: Gyroradius profile of the FILD intensity integrated in pitch angle between 58° and 65°. The blue crosses are the experimental measurements. The result of the tomographic inversion is shown in red. The recovered synthetic FILD signal is shown in black. The different colors correspond to the contribution of the different fast-ion populations: E_0 in green, $E_0/2$ in grey and the high-energy feature in magenta. [162]

two populations correspond to first orbit losses of NBI sources $Q7$ and $Q8$ respectively. A clear pattern is observed in the gyroradii of both populations: a main spot centered at $r_L \sim 4$ cm, which corresponds to the main NBI injection energy $E_0 = 82$ keV; a second spot centered at $r_L \sim 3$ cm, corresponding to the half energy component of the NBI; and an additional population at $r_L \geq 5$ cm, which corresponds to energies well above the main NBI injection and is only observed during the transient ELM crash. This population shall be referred to as the high-energy feature in the rest of the thesis. This observation is interpreted as the acceleration of beam ions in the presence of parallel electric fields arising during ELMs, when magnetic reconnection is believed to take place [59].

The signal shown in Fig.5.12(a) is directly obtained from the light pattern measured in the FILD scintillator. The finite size for the different spots is due to the finite resolution of the system in velocity space [122], and can be thought of as a distortion of the velocity-space of fast-ions reaching the detector pinhole, which is the quantity that aimed to be measured, as described in chapter 4. The undistorted velocity space distribution of the lost fast-ions reaching the detector pinhole can then be retrieved by the application of velocity-space tomographic techniques previously described. The result of this analysis is shown in Fig.5.12(b). It can be observed that the fast-ion populations giving rise to the main spots (NBI first orbit losses) in Fig.5.12(a) are well localized at the corresponding NBI injection energy. Furthermore, the population corresponding to the high-energy feature is surprisingly also well-localized in energy, rather than being an energy spread. The synthetic FILD signal retrieved from the tomographic inverted distribution is shown in Fig.5.12(c) which is in good agreement with the experimental measurement shown in Fig.5.12(a). A more detailed comparison is shown in Fig.5.13, where the gyroradius profile of the FILD signal integrated along the pitch angle interval between 58° and 65° is plotted. The blue crosses represent the experimental signal, which is smoothed due to the effect of the instrument resolution. The result of the tomographic inversion is plotted in red, where three peaks well defined in energy can be observed at $r_L = 4.1$ cm (corresponding to the main NBI injection energy $E_0 = 82$ keV), at $r_L = 2.9$ cm (corresponding to $E_0/2 = 41$ keV) and at $r_L = 5.8$ cm, which corresponds to an energy of ~ 160 keV. The synthetic signal is plotted in black, showing a good agreement with the experimental signal. The contributions to the synthetic signal from the different populations are plotted in magenta (for the high-energy feature), in green (for E_0) and grey (for $E_0/2$).

5.2.2 Correlation of high-energy population with ELMs

The observation of the high-energy feature is reproducible and well correlated with the NBI heating systems and the occurrence of ELMs. This is illustrated in Fig.5.14(a), where the evolution in time of the gyroradius profile measured by FILD is represented. The divertor current is plotted in white and the NBI power of the source contributing to the FILD signal is plotted in red. Before the NBI source is switched on, there is no signal in the FILD, despite an ELM occurring at 1.173 s. At 1.20 s the NBI is switched on and the FILD starts to measure the main and half NBI energy components, which are centered at $r_L = 4.1$ cm and $r_L = 2.9$ cm respectively. Then, everytime an ELM crash takes place, indicated by the spikes in the divertor current signal, the high-energy feature appears in FILD, as it can be seen in the four ELMs taking place between 1.2 and 1.28 s. The difference in the gyroradii profiles

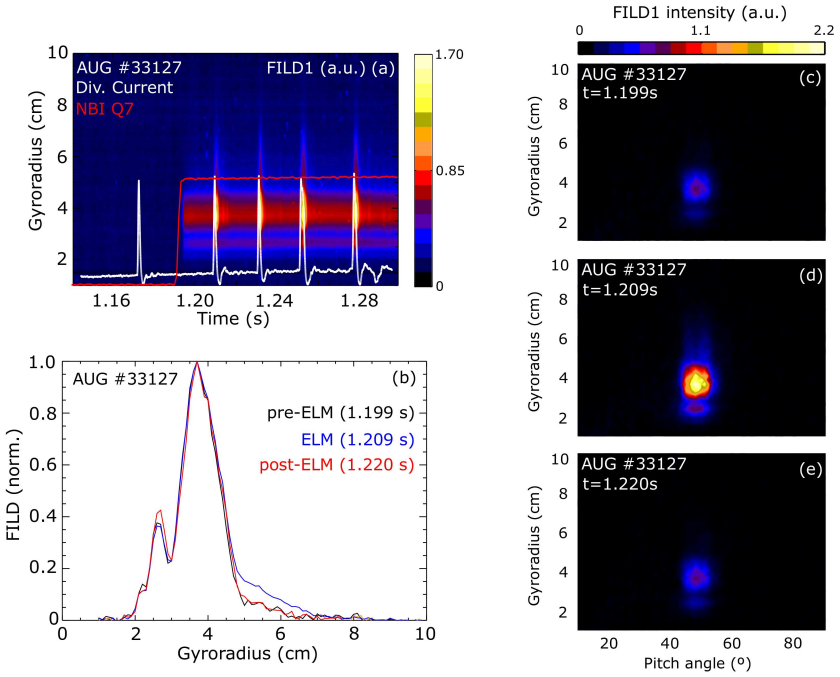

FIGURE 5.14: (a) Gyroradius profile evolution of the FILD signal at the relevant pitch angle in AUG shot #33127. The divertor current (white) is used as an ELM monitor. (b) Comparison between inter-ELM and intra-ELM gyroradii profiles obtained with FILD in shot #33127. (c), (d) and (e) show the complete velocity space measurement of FILD at these time points. [163]

between inter-ELM periods and during ELMs is illustrated in Fig.5.14(b), where the FILD signals have been normalized to unity in order to account for the difference in the intensity of the losses. The high-energy feature can clearly be observed during the ELM crash at 1.209 s (blue), where the FILD signal at $r_L > 5$ cm is above the level shown in the inter-ELM phases at 1.199 s and 1.220 s (black and red). The FILD signal showing the complete velocity space of the fast-ion losses before, during and after the ELM crash is shown in Fig.5.14(c), (d) and (e) respectively. It can be seen that the pitch angle distribution of the losses at the main and half energy injection components remains invariant during the ELM cycle.

Further evidence of the correlation between the high-energy feature measured by FILD and ELMs was found during operation in an ELM suppressed regime. In AUG, ELM suppression can be achieved by the application of external magnetic perturbations (MPs) [80, 164, 165] for certain values of q_{95}, which is the safety factor at 95% of the plasma minor radius, collisionality and differential phasing between the upper and lower sets of MP coils installed in AUG. Fig.5.15(a) shows the evolution of the FILD gyroradius profile measured during a whole shot in which MPs were applied, as indicated by the green box at the bottom of the figure. The divertor current is again plotted in white and used as an ELM monitor. Before the MP coils are switched on at 1.5 s, the high-energy feature can be seen in the FILD. At 1.5 s, the MPs are switched on, leading to an increased ELM frequency and decreased ELM amplitude. The high-energy feature can still be observed during this ELM mitigated regime. However, in the time interval between 2.5 and 5.2 s the ELM suppressed regime is established and the high-energy feature disappears from the FILD signal.

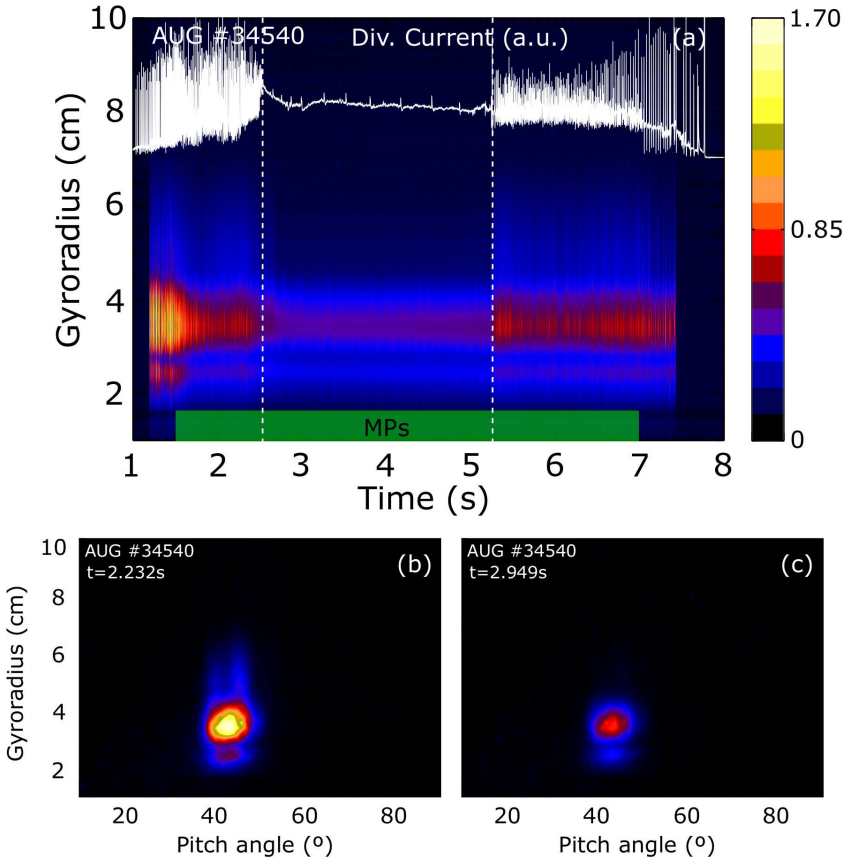

FIGURE 5.15: Evolution of the gyroradius profile of the FILD signal at the relevant pitch angle in AUG shot #34570, during which external MPs are applied (green box). The time window in which ELM suppression is achieved is indicated by two vertical dashed lines. The complete velocity space measured by FILD is shown at a time point before ELM suppression is achieved (b), and at a time point when ELMs are suppressed (c). [163]

At 5.2 s the ELM mitigated regime is recovered and thus, the high-energy feature reappears in the FILD signal during the ELM crashes. The complete velocity space measured by FILD is shown in Fig.5.15(b) and (c) before and during the ELM suppressed phase.

5.2.3 Variation of the pitch angle structure with q_{95}

While the pitch angle of the fast-ion losses at the main, half and third NBI energy components is not observed to change during the ELM crash, it was found that the high-energy feature exhibits a pitch angle structure that depends on the beam source and q_{95}. Scans in q_{95} were performed by ramping the toroidal magnetic field while keeping the plasma current constant. This is illustrated in Fig.5.16(a) which shows the pitch angle profile of the FILD signal for the main NBI injection energy (in black, for reference) and for the high-energy component (in colors). The different colors correspond to different time points (and therefore different q_{95} values) indicated in Fig.5.16(b). The profile at the main NBI injection energy shows two bumps at 45° and 60° corresponding to first orbit losses of beam sources Q7 and Q8 respectively. For the pitch angle interval between $40° - 50°$ corresponding to Q7 (passing orbits), two different spikes labelled as I and II can be observed. In order to observe the relative changes in the FILD intensity between these two spikes the FILD signal has been normalized at each time point. In the first time point (blue curve), the intensity of spike II is larger than that of spike I. However, as q_{95} is decreased during the discharge, the relative intensity of spike I increases with respect to spike II. In the second time point (red curve) the relative intensities are the same, while for the third and fourth time points (yellow and green curves) the relative intensity of spike I is larger than that of spike II. During the whole scan, however, no clear change in the pitch angle structure of the signals corresponding to beam ions from source Q8 (trapped particles) could be observed. Fig.5.16(c) and (d) show an additional scan in which q_{95} was ramped from 4.7 to 5.4. In this case, no clear dependence of the pitch angle structure was observed.

5.2.4 Electron cyclotron emission and soft X-ray bursts

In addition to the measurement of fast-ion losses, spikes in soft X-ray emission [166] and bursts in electron cyclotron emission (ECE) [105] signals have also been observed at the onset of some of these ELMs [167]. This is shown in Fig.5.17, where (a) shows the timetrace of the divertor current and the FILD signal during an ELM. Fig.5.17 shows the signal of the ECE diagnostic measured in the position indicated by the black circle in Fig.5.17(d), assuming that the emission corresponds to the local second electron cyclotron harmonic. Large spikes can be observed at around 3.1825 s. These bursts are localized in a small number of ECE channels indicating that the emission is constrained to a narrow frequency band, in this case between 110 and 112 GHz. Radiation transport modelling including broadening effects [107] has been carried out for the interpretation of these measurements. The emission is originated at $\rho_{pol} > 0.92$ and is likely produced by the build-up of a non-thermal electron population with energies up to 25 keV. In Fig.5.17(c) the signals of three different soft X-ray channels are shown. Their lines of sight near the edge of the plasma are indicated in Fig.5.17(d). The signals associated with the blue and green lines of sight, which are in the scrape-off layer and tangential to the separatrix, show bursts slightly after

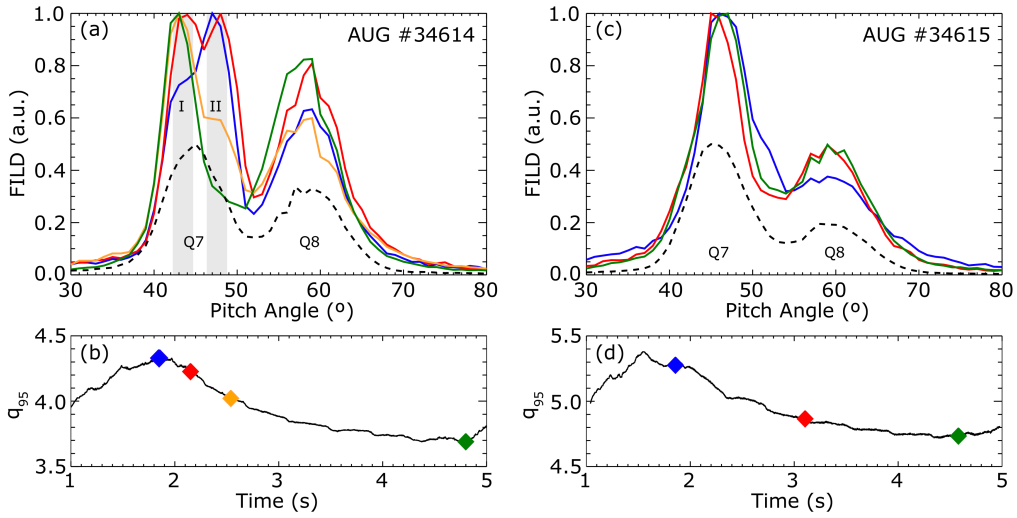

FIGURE 5.16: (a) and (c) show the pitch angle profile of the FILD signal for AUG #34614 and #34615 respectively. In black, the profile at the main NBI injection energy is plotted for reference (dashed line). The profile at the high-energy component is plotted in different colors for different timepoints indicated in (b) and (d), which shows the evolution of q_{95} with time. [163]

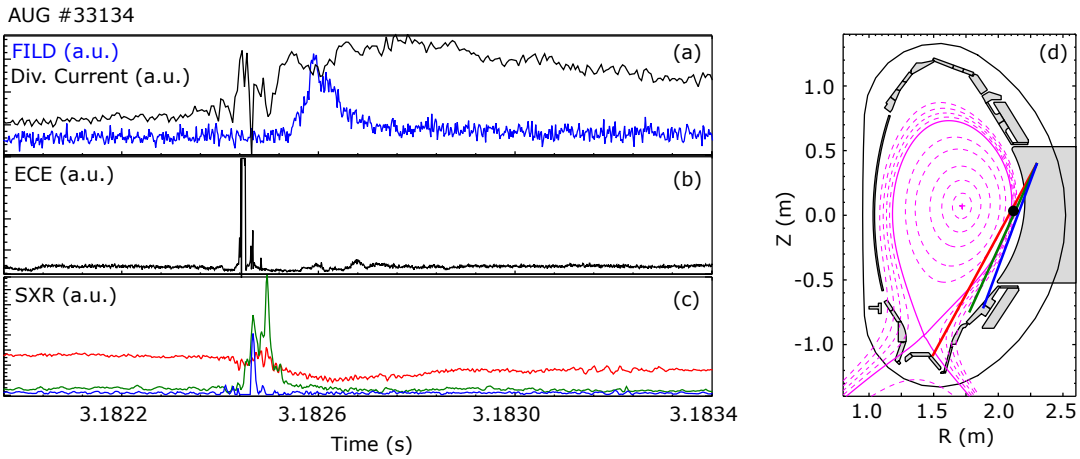

FIGURE 5.17: (a) Timetrace of the FILD signal (in blue) and the divertor current (in black) during an ELM in AUG. (b) Timetrace showing a burst in electron cyclotron emission from the plasma edge. (c) Timetraces of three different channels of the soft X-ray diagnostic with lines of sight near the plasma edge. (d) Poloidal plot of the AUG vessel showing in detail the soft X-ray lines of sight and the inferred location of the ECE emission. [163]

the ECE, while such behaviour is not observed for the line of sight passing through the separatrix. A similar observation of bursts in both the ECE and soft X-ray diagnostics was reported in MAST [168] to be indicative of electron acceleration, which further supports the hypothesis of the presence of electric fields. However, the detailed mechanism leading to the electron acceleration and subsequent ECE emission in AUG remains unclear and shall be investigated in detail in the future.

The results of the tomographic inversion together with the variation of the pitch angle structure of the high-energy feature with q_{95}, suggest a mechanism for the acceleration of the beam ions which is highly velocity-space dependent. Moreover, the characteristic times associated with the individual fast-ion filaments ($t \sim 100\mu$s) in comparison with the fast-ion slowing down time in these plasmas ($\tau_s = 100$ ms) indicate that the phenomenon is likely to be collisionless. In view of these observations, a resonant interaction between the beam ions and the parallel electric field emerging during the ELM crash, when magnetic reconnection is believed to take place [59], is proposed to be responsible for the acceleration process.

5.2.5 Modelling

The increased beam-ion losses and accelerated population measured during the ELM with the FILD systems are likely the result of a complex mechanism including a resonant interaction between the fast-ions and the induced 3D electromagnetic perturbation. Modelling efforts have been carried out in order to gain a deeper insight into this interaction, by performing simulations to investigate separately the effect of magnetic and electric perturbations on fast-ions. The aim of the simulations described here is to qualitatively reproduce the main features of the experimental observations.

Full-orbit following simulations of fast-ions have been performed during a complete ELM crash including realistic magnetic perturbation fields, which are obtained from simulations with the 3D non-linear resistive MHD code JOREK [169]. The associated electric fields have not been included at this stage. No collisions between the fast-ions and the bulk plasma have been considered in the simulations. In Fig.5.18 the magnetic perturbation associated with the ELM is plotted. As illustrated, the perturbation is located at the edge of the plasma. The orbits of the fast-ion losses measured by FILD, which are plotted in white (trapped) and green (passing), explore the region where the perturbation is located. The simulated fast-ion heat load pattern on the AUG wall is shown in Fig.5.19(a). The footprint located at $\theta = 50^\circ$ corresponds to the upper edge of the AUG limiters, while the footprint located at $\theta = -100^\circ$ corresponds to the lower divertor. The $n = 8$ toroidal mode number of the ELM can be observed in the pattern of the losses located around the midplane, which show diagonal structures tilted towards positive increase in the toroidal direction, thus again revealing the 3D nature of the phenomenon. The time evolution of the losses throughout the whole ELM crash is shown in Fig.5.19(b), where the losses in the entire vessel have been integrated. Several spikes can be observed resembling the filamentary-like pattern of the measured fast-ion losses shown in Fig.5.11. It should be mentioned that, for computational reasons, the resistivity used in this JOREK simulation is artificially increased, which might lead to a distortion of the

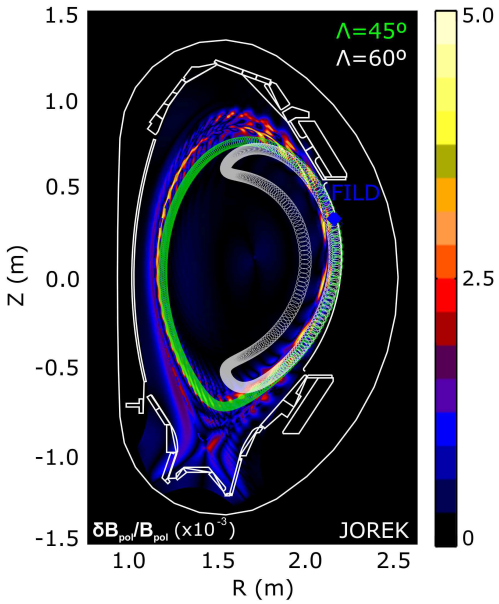

FIGURE 5.18: Poloidal contour of the magnetic perturbation of an ELM calculated with JOREK. Typical orbits measured by FILD are overlayed in green and white. [162]

timescale of these losses. The fast-ion loss level in the absence of the magnetic perturbation is indicated by a dashed red line for reference.

To further investigate the nature of the fast-ion transport induced by the ELM perturbation, calculations of the variation of the toroidal canonical momentum $P_\Phi = mRv_\Phi - Ze\psi$ have been carried out with the orbit following code ASCOT [149]. A set of $40 \cdot 10^3$ markers was followed for 500 μs in a perturbed magnetic configuration within the ELM crash, with a range of initial values in the radial coordinate R and pitch $\Lambda = \frac{v_\parallel}{v}$, defined with respect to the magnetic field, and with a fixed energy of 60 keV. In an axisymmetric magnetic configuration, P_Φ is a motion invariant. However, in the presence of 3D symmetry breaking magnetic fields, such as those imposed by the application of external MPs, the variation of the toroidal canonical

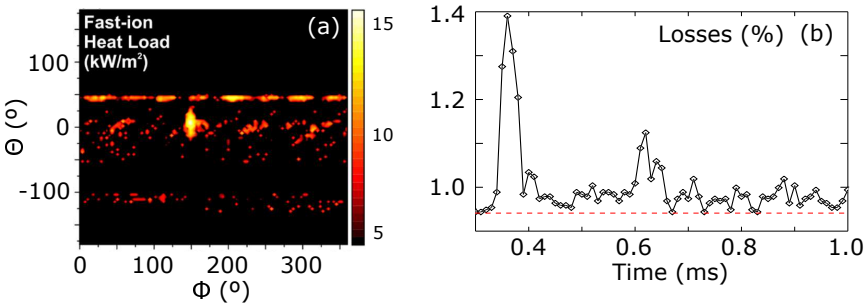

FIGURE 5.19: (a) Fast-ion heat load pattern on the AUG walls calculated during a simulated ELM crash with the full-orbit following code Gourdon. (b) Time evolution of the fast-ion losses on the walls during the ELM crash. The dashed red line indicates the level of fast-ion losses in the absence of the magnetic perturbation. [163]

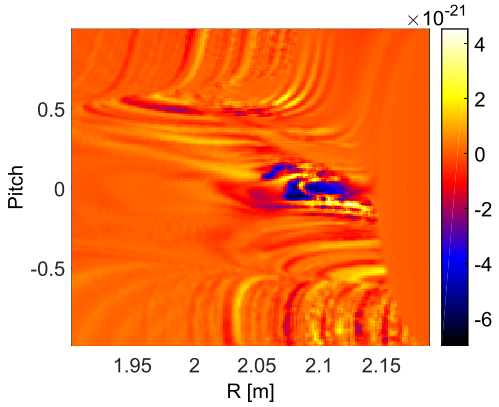

FIGURE 5.20: Variation of the toroidal canonical angular momentum calculated with ASCOT during an ELM crash. Positive variation (yellow regions) is interpreted as an outward transport while a negative variation is interpreted as an inward transport (blue regions). [163]

momentum is a measurement of the radial transport of the ions. Given that the sign convention used here is such that Ψ is negative and, in absolute values, larger at the magnetic axis than at the plasma edge, an increase in P_Φ implies a fall in ψ, which corresponds to outward transport of ions ($Ze > 0$). In contrast, a decrease in P_Φ corresponds to inward transport of ions. Fig.5.20 shows the results of such a simulation. The trapped-passing boundary region can be observed. In the region corresponding to the passing orbits, vertical resonant structures are observed, while in the trapped orbits region the resonances show a different pattern.

Simulations including the magnetic field perturbation associated with the ELM qualitatively reproduce the time evolution of the fast-ion losses. However, these cannot account for the observed particle acceleration, for which the presence of an electric field is needed. In order to explore the viability of the proposed acceleration mechanism for the beam ions during ELMs, full orbit particle simulations have been carried out in a realistic magnetic equilibrium for AUG. A simple test model for the parallel electric field, which was kept static during the simulation, was used:

$$\overrightarrow{E} = \overrightarrow{b_\parallel} \cdot A \cdot \exp \frac{(\rho - \rho_0)^2}{2\sigma^2} \cdot \cos(n\phi - m\theta^* + \alpha) \tag{5.5}$$

where $\overrightarrow{b_\parallel}$ is a unit vector parallel to the magnetic field, A is a parameter controlling the amplitude of the electric field, ρ_0 and σ are the centroid and width of the perturbation in ρ, and n and m are the toroidal and poloidal mode numbers respectively. ϕ is the toroidal angle coordinate, θ^* the poloidal angle coordinate and α is the phase of the perturbation.

This simple model reproduces the 3D character of the expected parallel electric field associated with the ELM, and its parametrization makes it possible to easily vary its spatial structure and amplitude to perform sensitivity studies. In these simulations a set of 10^5 markers have been followed during 50 μs, which is the time scale associated with a single fast-ion filament as illustrated in Fig 5.11. A scan was performed in R and Λ with a fixed energy of 90 keV corresponding to the NBI injection energy of box 2 in AUG.

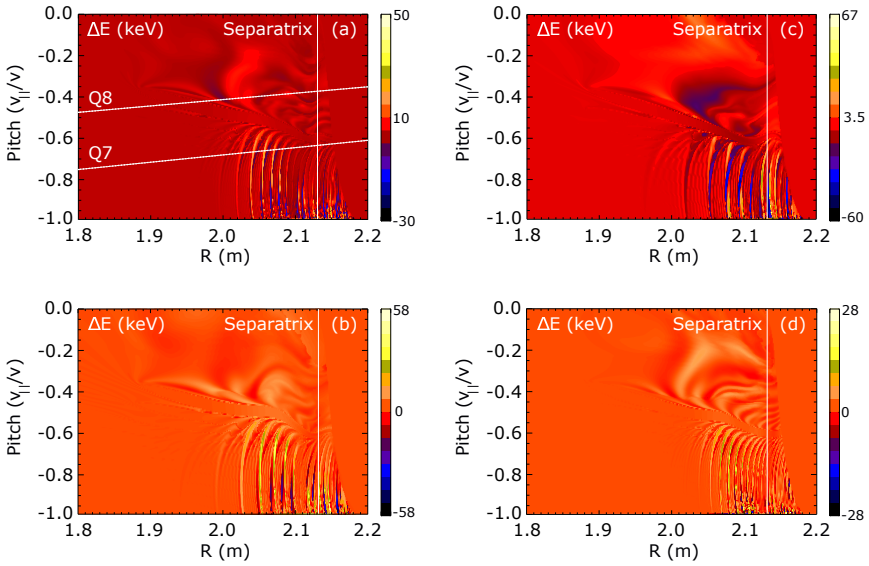

FIGURE 5.21: Simulated energy gain of the markers against the initial pitch angle and radial position in the presence of a parallel electric field. The separatrix position is indicated in white for reference. (a) Case with a toroidal mode number of $n = 10$, $\rho_0 = 0.9$ and $\sigma = 0.1$. The approximated deposition of beams Q7 and Q8 is indicated by the dotted white lines. Cases (b) and (c) are the same as case (a) but with a toroidal mode number $n = 7$ and $n = 5$ respectively. (d) Case with $\rho_{pol} = 0.95$ and $\sigma = 0.05$. In all cases similar structures can be observed in the trapped and passing orbit regions.

A sensitivity study on the different parameters has been performed by carrying out multiple sets of simulations. The toroidal mode number of the perturbation has been changed from $n = 3$ to $n = 10$, within the range expected for ELMs in AUG [170]. The poloidal number was set as $m = q \cdot n$. The centroid of the perturbation has been located in the edge region and its width has been set to values comparable to the pedestal width. Concerning the amplitude of the parallel electric fields, we have set values from 0.1 kV/m to a maximum of 2.0 kV/m, which is of the order of magnitude predicted by the modelling [168], and well above the Dreicer electric field for these plasmas.

The first results are shown in Fig.5.21(a). Here the perturbation was placed in $\rho_0 = 0.9$ and a width of $\sigma = 0.1$, the amplitude of the parallel electric field was set to $A = 2$ kV/m and the toroidal mode number to $n = 10$. It can be observed that only the ions exploring the edge region gain or lose energy. The maximum energy gain obtained is on the order of tens of keV, which is consistent with the experimental observation, and the trend indicates that larger energy gains are obtained for lower toroidal mode numbers. Furthermore, vertical structures can be observed for the ions in the region corresponding to passing orbits ($\Lambda \leq -0.5$) similar to what is observed in Fig.5.20. No such clear structures can be observed for the ions in the region corresponding to trapped orbits ($\Lambda \geq -0.5$). These structures might be explained by linear and non-linear resonances between the particles and the perturbation [87], similar to recent observations in plasmas with externally applied 3D perturbations [171].

The FILD experimental measurements are consistent with this picture. The pitch

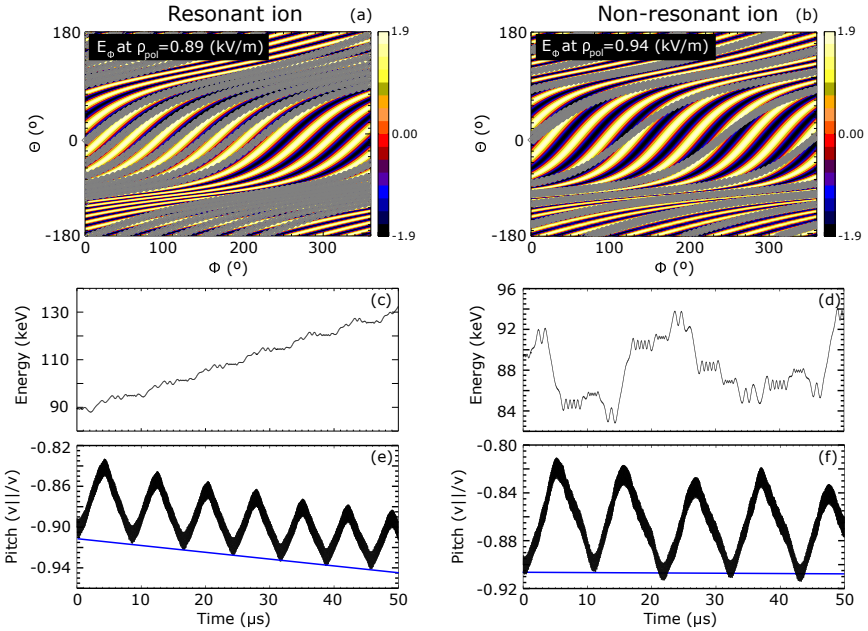

FIGURE 5.22: Trajectory (grey) of a resonant (a) and non-resonant (b) ion overplotted on top of the parallel electric field associated with the ELM perturbation. (c) and (d) show the energy evolution of the resonant and non-resonant markers respectively, while (e) and (f) show the corresponding pitch angle evolution. The blue lines show the evolution of the pitch angle at the outer midplane. [163]

angle structure dependence of the high-energy feature with q_{95} was found to be very clear for passing ions corresponding to beam source Q7, while a less clear dependence was observed for trapped ions corresponding to beam source Q8, as shown in Fig.5.16. The approximated deposition of beam sources Q7 and Q8 is indicated in Fig.5.21(a) by two white dashed lines. By ramping q_{95} in the experiment, FILD probes ions with different radial birth positions, and this is equivalent to moving horizontally in Fig.5.21. For orbits in the passing region, which are populated by NBI Q7, the structure of the resonances are vertical lines and one would then be jumping from one resonance to another, which is giving rise to the peaks at different pitch angles in the FILD signal. However, for orbits in the trapped region, which is populated by NBI Q8, the structure of the resonances is more complicated and therefore moving along the radial coordinate does not necessarily lead to a different resonance. In this picture, the change in the pitch angle structure of the FILD signal can be understood as the probing of different resonances for different q_{95} values.

The evolution of the velocity space of the markers in the simulation is shown in Fig.5.22. The plots in the left and right columns correspond to a resonant and non-resonant ion, with an initial pitch of $\Lambda = -0.9$ and initial radial position of $R = 2.055$ m and $R = 2.140$ m respectively. In Figs.5.22(a) and (b) the projection of the ion orbit into the poloidal (Θ) and toroidal (Φ) angles is overplotted in grey on top of the toroidal electric field at the magnetic surface where the orbit is laying, which is represented by the contour. It can be seen that for the case of the resonant ion (a) the orbit is better aligned with the perturbation than in the case of the non-resonant orbit. Additionally, the resonant ion shows a toroidal displacement every time a poloidal turn is completed. Fig.5.22(c) shows how the resonant ion gains energy continuously while the non-resonant ion (d) does not show a net energy gain.

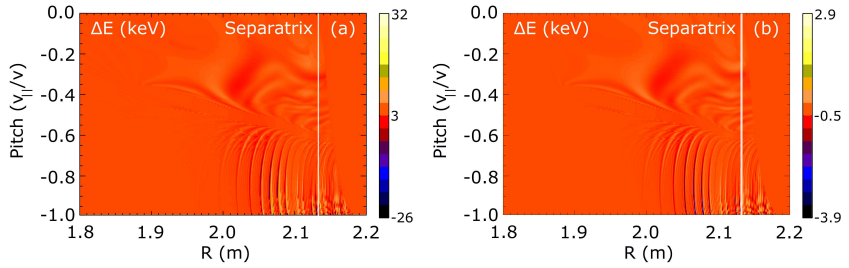

FIGURE 5.23: Energy gain of the markers in the presence of parallel electric fields with different amplitudes and $n = 10$, $\rho_{pol} = 0.9$ and $\sigma = 0.1$. (a) $A = 1$ kV/m. (b) $A = 0.1$ kV/m.

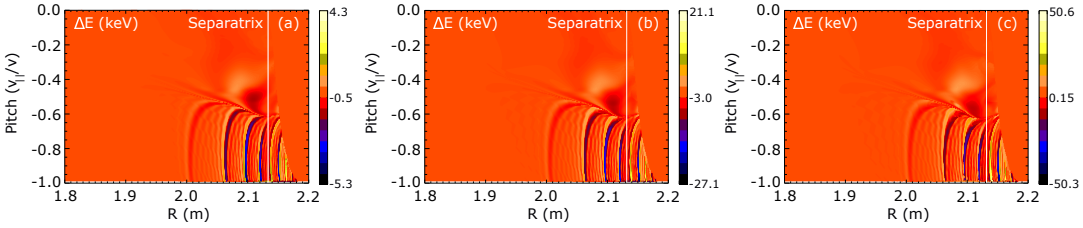

FIGURE 5.24: Energy gain of the markers in the presence of parallel electric fields with different amplitudes and $n = 3$, $\rho_{pol} = 0.9$ and $\sigma = 0.1$. (a) $A = 0.1$ kV/m. (b) $A = 0.5$ kV/m. (c) $A = 1.0$ kV/m

The pitch angle of the resonant ion increases in absolute value, this is, it gains parallel velocity as expected by an acceleration due to a parallel electric field. This is shown in Fig.5.22(e), where the blue line highlights the pitch angle of the ion at the outer midplane. On the other hand, it can be seen that the pitch angle barely changes for the non-resonant ion (f).

The topology of these resonances is reproduced over a wide range of parameters of the perturbation. A scan in the toroidal mode number is shown in Fig.5.21(a)-(c) where the n was set to 10, 7 and 5 respectively. The same kind of pattern is obtained. The trend shows that larger values of the maximum energy gain are obtained for lower toroidal mode numbers. Furthermore, the number of vertical structures in the passing region seems to decrease for lower toroidal mode numbers. A possible explanation could be the widening of the resonances as the degree of symmetry of the perturbation is decreased.

In Fig.5.21(d) the perturbation is centered at $\rho_{pol} = 0.95$ and has a width of $\sigma = 0.05$, showing again the same qualitative pattern. In Fig.5.23(a) and (b) the results of a scan in the amplitude of the parallel electric field are shown, where values of 1 kV/m and 0.1 kV/m respectively were set for a case with $n = 10$. The same patterns are obtained and the maximum energy gain is observed to decrease for lower amplitudes, as expected. The same scan in the amplitude of the parallel electric field was performed in the case of a toroidal mode of $n = 3$. The results are shown in Fig.5.23(a)-(c), with amplitudes of $A = 0.1$ kV/m, $A = 0.5$ kV/m and $A = 1.0$ kV/m respectively. Larger energy gains are obtained consistently with respect to the case of $n = 10$. Fig.5.25 shows a scan in the following time of the markers. The same structures are kept.

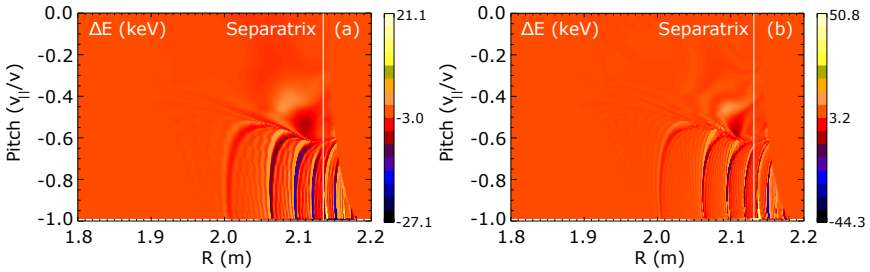

FIGURE 5.25: Energy gain of the markers in the presence of parallel electric fields with different following times and $n = 10$, $A = 2\,\mathrm{kV/m}$, $\rho_{pol} = 0.9$ and $\sigma = 0.1$. (a) $t = 50\mu$s. (b) $t = 100\mu$s.

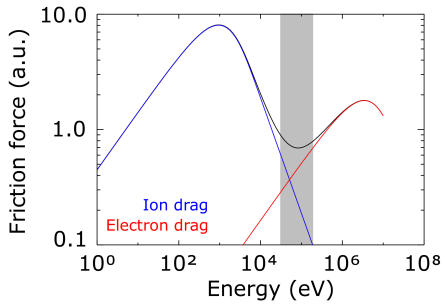

FIGURE 5.26: Friction force on ions calculated for typical AUG parameters as a function of energy. The local minimum is in the range of the NBI injection energies at AUG. The blue line represents the ion drag, the red line represents the electron drag, and the black curve is the sum of both.

In the case of the ELMs studied here, the expected parallel electric fields are well above the Dreicer value for these plasmas [172], and the interaction times are below the fast-ion slowing down times. Therefore the drag force on fast-ions can be neglected. However, in the presence of less intense parallel electric fields in tokamaks, particle acceleration is often explained in terms of runaway mechanisms. In the presence of a parallel electric field, charged particles are subject to two forces, the one due to the electric field, and the opposing drag force due to collisions with the bulk plasma particles [173]:

$$m\frac{d\vec{v}}{dt} = q\vec{E} - \vec{F}_{di} - \vec{F}_{de} \tag{5.6}$$

where $\vec{F}_{di}$ is the drag force due to thermal ions and $\vec{F}_{de}$ is the drag force due to thermal electrons. At AUG, the minimum of the drag force on ions happens to be at energies close to the NBI injection energy, as illustrated in Fig.5.26. This suggests that, if ion runaway shall happen at all, beam-ions would be more sensitive to it. The improved capabilities of the FILD detectors in terms of energy resolution could be used in search of possible ion acceleration in events such as disruptions, the formation of tearing modes or sawtooth crashes, where resistive MHD effects lead to the appearance of parallel electric fields.

Chapter 6

Summary and conclusions

This thesis contributes to the study of the impact of MHD phenomena on fast-ions in tokamak plasmas. A good confinement of the fast-ion population is mandatory to assess an optimal plasma heating and current drive. Therefore, understanding the physical mechanisms underlying the interaction between fast-ions and MHD is of paramount importance to, ultimately, develop tools that allow to control the fast-ion distribution via external actuators. This study is based on velocity-space resolved measurements of fast-ion losses carried out with scintillator based FILDs, which are capable to provide valuable information on the interaction between modes and particles.

A comprehensive characterization of the response of scintillator based FILDs has been carried out for the first time. A model based on a weight function formalism has been developed, which relates the velocity-space distribution of ions reaching the detector pinhole, to the velocity-space distribution effectively measured at the scintillator plate. The latter can be understood as a distortion of the former due to the finite resolution of the system. The model has been included in a code called FILDSIM, and allows the investigation of fast-ion losses with an unprecedented velocity-space resolution.

The forward model allows to generate synthetic FILD signals, which can be used for a better comparison between experiments and modelling. Furthermore, this tool can be used in the design phase of FILD detectors to evaluate the expected resolution of the system or signal levels among others [174, 175]. On the other hand, the tomographic inversion of FILD signals allows to recover the undistorted velocity-space distribution of fast-ions reaching the detector pinhole, potentially unraveling details of the velocity-space dynamics of fast-ion losses. Future work will focus on the development of alternative tomographic inversion methods which can improve the time performance, with the goal of a routine application of this technique to FILD signals. This tool constitutes a first step towards the integration of FILD measurements in a common framework including other confined fast-ion diagnostics, with the ultimate goal of achieving the tomographic reconstruction of the full fast-ion distribution function. The combination of different diagnostics in velocity-space tomography is a general problem which has been discussed in previous works [153, 157]. The main challenge is to combine velocity-space measurements which are performed in different volumes of the configuration space. This is of particular importance in the case of FILD, whose probing volume is in the far SOL, very distant from the plasma volumes - inside the separatrix - probed by confined fast-ion diagnostics. Thus, the gradients in the fast-ion distribution function play an important role in the combination of the information which can be retrieved by the different systems. In this sense, the so-called orbit tomography method [176] could be a good framework

to combine the information provided by diagnostics measuring the confined and escaping fast-ion populations.

These improved capabilities have been used in the study of ICRH accelerated fast-ion losses induced by a tearing mode in the ASDEX Upgrade tokamak. For the first time, velocity-space resolved absolute measurements of fast-ion heat loads have been provided, and an estimation of the contribution of different loss channels (prompt, convective and diffusive) has been given. The modelling results suggest that the contribution of MHD induced fast-ion losses is dominant with respect to the prompt losses. A good agreement was found between the experimental measurement of the velocity-space of the fast-ion losses and the synthetic FILD signal, built through the combination of orbit following simulations carried out with ASCOT, and FILDSIM. The resonances responsible for these losses were identified. The damage provoked to the FILD1 detector is a strong evidence of how MHD instabilities can degrade the fast-ion confinement and how undesirable this is.

For the first time, the velocity-space of ELM induced fast-ion losses has been studied. This revealed the existence of an accelerated beam-ion population. This population is observed to correlate with the application of the NBI systems and the occurrence of ELMs. Multiple pitch angle structures are observed, which depend on the q_{95} value and the topology of the fast-ion orbits. Such accelerated beam-ion population is also observed in ELM mitigated regimes, but not in ELM suppressed regimes. Motivated by the detailed experimental observations, a mechanism responsible for the ion acceleration is proposed: a resonant interaction between the beam ion orbits and the parallel electric fields associated with the ELMs. Numerical simulations of fast-ions in a realistic magnetic equilibrium and including a static parallel electric field, implemented through an analytical model which resembles the 3D structure of the perturbation, qualitatively reproduce the experimental observations. This calls for a kinetic treatment of energetic particles in ELM modelling, in line with previous work [168]. Additionally, the impact that the accelerated population of fast-ions may have on the stability of the ELM should be evaluated, as well as its contribution to the heat-load deposition on the wall of the machine. Future work will focus on the experimental evaluation of the energy gain as a function of q_{95}, NBI injection energy and collisionality. From the modelling point of view, the proposed acceleration mechanism should be assessed in the presence of simultaneous time-evolving electric and magnetic perturbation fields during the ELM, such as those that can be provided by non-linear resistive MHD codes like JOREK.

Although previous investigations had reported ion acceleration in magnetically confined plasmas during internal reconnection events [173, 177] and merging compression during plasma start-up [15], this is the first experimental indication of ion acceleration during ELMs in a tokamak. Furthermore, particle acceleration in the presence of magnetic reconnection is ubiquitous in space and astrophysical plasmas [178, 179], and measurements provided by laboratory experiments like these - with improved diagnostics capabilities - may help to shed light on the fundamental physics underlying these phenomena [180], which may be of interest not only to the fusion but also to the astrophysics community. The observation of beam-ion acceleration during ELMs may be of particular interest due to the similarities often highlighted between these and solar flares [181]: in both phenomena particles are explosively expelled with potentially harmful effects and magnetic reconnection is thought to play a role.

The investigations carried out in this thesis highlight the relevance of resonant interactions between fast-ions and MHD perturbations in tokamak plasmas, and their impact in both the configuration space and the momentum space of the fast-ions, evidenced through an enhanced radial transport and an acceleration of the fast-ions respectively.

Appendix A

List of publications

List of publications relevant for this thesis as main author:

1. J. Galdon-Quiroga et al. "Velocity space resolved absolute measurement of fast ion losses induced by a tearing mode in the ASDEX Upgrade tokamak". In: *Nucl. Fusion* 58.3 (Mar. 2018), p. 036005. ISSN: 0029-5515. DOI: 10.1088/1741-4326/aaa33b. URL: http://stacks.iop.org/0029-5515/58/i=3/a=036005?key=crossref.355c77134e045b8ad6e90f9a5266b0c4

2. J. Galdon-Quiroga et al. "Beam-Ion Acceleration during Edge Localized Modes in the ASDEX Upgrade Tokamak". In: *Phys. Rev. Lett.* 121.2 (July 2018), p. 025002. ISSN: 10797114. DOI: 10.1103/PhysRevLett.121.025002. URL: https://link.aps.org/doi/10.1103/PhysRevLett.121.025002

3. J Galdon-Quiroga et al. "Velocity-space sensitivity and tomography of scintillator-based fast-ion loss detectors". In: *Plasma Phys. Control. Fusion* 60.10 (Oct. 2018), p. 105005. ISSN: 0741-3335. DOI: 10.1088/1361-6587/aad76e. URL: http://stacks.iop.org/0741-3335/60/i=10/a=105005?key=crossref.b42633c5760bd48362347bf45a33e689

4. J Galdon-Quiroga et al. "Observation of accelerated beam ion population during edge localized modes in the ASDEX Upgrade tokamak". In: *submitted to Nucl. Fusion* (2018)

List of additional publications:

1. J Galdon-Quiroga et al. "Conceptual design of a scintillator based Imaging Heavy Ion Beam Probe for the ASDEX Upgrade tokamak ." In: *J. Instrum.* 12 (Aug. 2017), p. C08023. ISSN: 17480221. DOI: 10.1088/1748-0221/12/08/C08023. URL: http://stacks.iop.org/1748-0221/12/i=08/a=C08023?key=crossref.4b102dbd8a84aa8fc72437a5c1f917b5

2. J. Rasmussen et al. "Collective Thomson scattering measurements of fast-ion transport due to sawtooth crashes in ASDEX Upgrade". In: *Nucl. Fusion* 56.11 (Nov. 2016), p. 112014. ISSN: 0029-5515. DOI: 10.1088/0029-5515/56/11/112014. URL: http://stacks.iop.org/0029-5515/56/i=11/a=112014?key=crossref.0d61d374bc57804b4e76724c2e8f86fb%20http://stacks.iop.org/0029-5515/56/i=11/a=112014

3. J. Ayllon-Guerola et al. "A fast feedback controlled magnetic drive for the ASDEX Upgrade fast-ion loss detectors". In: *Rev. Sci. Instrum.* 87.11 (Nov. 2016), 11E705. ISSN: 10897623. DOI: 10.1063/1.4959913. URL: http://aip.scitation.org/doi/10.1063/1.4959913

4. M. Garcia-Munoz et al. "Conceptual design of the ITER fast-ion loss detector". In: *Rev. Sci. Instrum.* 87.11 (Nov. 2016), p. 11D829. ISSN: 0034-6748. DOI: 10.1063/1.4961295. URL: http://aip.scitation.org/doi/10.1063/1.4961295

5. M Rodriguez-Ramos et al. "First absolute measurements of fast-ion losses in the ASDEX Upgrade tokamak". In: *Control. Fusion* 59.10 (Oct. 2017), p. 105009. ISSN: 13616587. DOI: 10.1088/1361-6587/aa7e5f. URL: http://stacks.iop.org/0741-3335/59/i=10/a=105009?key=crossref.ae062acc34583cda326a1eae26f6dd69%20http://iopscience.iop.org/article/10.1088/1361-6587/aa7e5f/pdf

6. H. Meyer et al. "Overview of progress in European medium sized tokamaks towards an integrated plasma-edge/wall solution". In: *Nucl. Fusion* 57.10 (Oct. 2017), p. 102014. ISSN: 0029-5515. DOI: 10.1088/1741-4326/aa6084. URL: http://stacks.iop.org/0029-5515/57/i=10/a=102014?key=crossref.2017887bb6c99f0f75fed0a4997e0542

7. J. Ayllon-Guerola. "Dynamic and thermal simulations of a fast-ion loss detector for ITER". in: *Fusion Eng. Des.* 123 (Nov. 2017), pp. 807–810. ISSN: 0920-3796. DOI: 10.1016/J.FUSENGDES.2017.04.071. URL: http://www.sciencedirect.com/science/article/pii/S092037961730474X?via%7B%5C%%7D3Dihub

8. Ye. O. Kazakov et al. "Efficient generation of energetic ions in multi-ion plasmas by radio-frequency heating". In: *Nat. Phys.* 13.10 (June 2017), pp. 973–978. ISSN: 1745-2473. DOI: 10.1038/nphys4167. URL: http://www.nature.com/doifinder/10.1038/nphys4167

9. G. Giruzzi et al. "Physics and operation oriented activities in preparation of the JT-60SA tokamak exploitation". In: *Nucl. Fusion* 57.8 (Aug. 2017), p. 085001. ISSN: 0029-5515. DOI: 10.1088/1741-4326/aa7962. URL: http://stacks.iop.org/0029-5515/57/i=8/a=085001?key=crossref.41409c0230d45f9adf24102fa22159e1

10. E Viezzer et al. "Ion heat transport dynamics during edge localized mode cycles at ASDEX Upgrade". In: *Nucl. Fusion* 58.2 (Feb. 2018), p. 026031. ISSN: 17414326. DOI: 10.1088/1741-4326/aaa22f. URL: http://stacks.iop.org/0029-5515/58/i=2/a=026031?key=crossref.ded908319292b5944e4d7c0059067322

11. S E Sharapov et al. "The effects of electron cyclotron heating and current drive on toroidal Alfvén eigenmodes in tokamak plasmas". In: *Plasma Phys. Control. Fusion Plasma Phys. Control. Fusion* 60.1 (Jan. 2018), pp. 14026–10. ISSN: 0741-3335. DOI: 10.1088/1361-6587/aa90ee. URL: http://stacks.iop.org/0741-3335/60/i=1/a=014026?key=crossref.870796797bb44fb7cc78fc032f333fbd%20https://doi.org/10.1088/1361-6587/aa90ee

12. J. Gonzalez-Martin et al. "First measurements of a scintillator based fast-ion loss detector near the ASDEX Upgrade divertor". In: *Rev. Sci. Instrum.* 89.10 (Oct. 2018), p. 10I106. ISSN: 10897623. DOI: 10.1063/1.5038968. URL: http://aip.scitation.org/doi/10.1063/1.5038968

13. Matthias Willensdorfer et al. "Dynamics of ideal modes and subsequent ELM crashes in 3D tokamak geometry from external magnetic perturbations". In: *Plasma Phys. Control. Fusion* (Aug. 2018). ISSN: 0741-3335. DOI: 10.1088/1361-6587/aadc39. URL: http://iopscience.iop.org/article/10.1088/1361-6587/aadc39

14. J. F. Rivero-Rodriguez et al. "A rotary and reciprocating scintillator based fast-ion loss detector for the MAST-U tokamak". In: *Rev. Sci. Instrum.* 89.10 (Oct.

2018), p. 10I112. ISSN: 0034-6748. DOI: 10.1063/1.5039311. URL: http://aip.scitation.org/doi/10.1063/1.5039311

15. L Sanchis-Sanchez et al. "Main Parametric Dependencies of the Fast-Ion Edge Resonant Transport Layer Induced by 3D Perturbative Fields in the ASDEX Upgrade Tokamak". In: *Submitt. to Plasma Phys. Control. Fusion* (2018)

16. M Garcia-Muñoz et al. "Active Control of Alfvén Eigenmodes in Magnetically Confined Toroidal Plasmas". In: *Submitt. to Plasma Phys. Control. Fusion* (2018)

Appendix B

Contribution to conferences

List of contributions to conferences relevant for this thesis as main author:

1. J. Galdon-Quiroga et al. "The synthetic fast-ion loss detector (Poster)". In: *1st European Conference on Plasma Diagnostics*. Frascati. 2015
2. J. Galdon-Quiroga et al. "Analysis of fast-ion heat load induced by tearing fluctuations in the ASDEX Upgrade tokamak (Poster)". In: *14th IAEA Technical Meeting on Energetic Particles in Magnetic Confinement Systems*. Vienna. 2015
3. J. Galdon-Quiroga et al. "Experimental evidence of beam ion acceleration during ELMs in the ASDEX Upgrade tokamak (Oral)". In: *15th IAEA Technical Meeting on Energetic Particles in Magnetic Confinement Systems*. Princeton. 2017
4. J. Galdon-Quiroga et al. "Acceleration of beam ions during edge localized modes in the ASDEX Upgrade tokamak (Poster)". In: *45th EPS Conference on Plasma Physics*. Prague. 2018
5. J. Galdon-Quiroga et al. "Impact of an edge resonant transport layer on fast-ion confinement in the ASDEX Upgrade tokamak (Poster)". In: *27th IAEA Fusion Energy Conference*. Gandhinagar. 2018

Bibliography

[1] International Nuclear Safety Advisory Group. *The Chernobyl Accident: Updating of INSAG-1*. Tech. rep. Vienna: International Atomic Energy Agency, 1992. URL: https://www-pub.iaea.org/MTCD/publications/PDF/Pub913e%7B%5C_%7Dweb.pdf.

[2] International Atomic Energy Agency. *THE FUKUSHIMA DAIICHI ACCIDENT REPORT BY THE DIRECTOR GENERAL*. Tech. rep. Vienna: International Atomic Energy Agency, 2015. URL: https://www-pub.iaea.org/MTCD/Publications/PDF/Pub1710-ReportByTheDG-Web.pdf.

[3] BP. *BP Statistical Review of World Energy*. Tech. rep. 2018, p. 11.

[4] H. S. Bosch and G. M. Hale. "Improved formulas for fusion cross-sections and thermal reactivities". In: *Nucl. Fusion* 32.4 (Apr. 1992), pp. 611–631. ISSN: 00295515. DOI: 10.1088/0029-5515/32/4/I07. URL: http://stacks.iop.org/0029-5515/32/i=4/a=I07?key=crossref.499a5e49f8dde53d266bf4090e2da6c1.

[5] J. Jacquinot. "Fifty years in fusion and the way forward". In: *Nucl. Fusion* 50.1 (Jan. 2010), p. 014001. ISSN: 0029-5515. DOI: 10.1088/0029-5515/50/1/014001. URL: http://stacks.iop.org/0029-5515/50/i=1/a=014001?key=crossref.9d8f57492997c4fd4a0bf9c0be35feaf.

[6] J. Wesson and D.J Campbell. *Tokamaks*. 3rd. Oxford University Press, 2004. ISBN: 0198509227.

[7] A Bock et al. "Advanced tokamak investigations in full-tungsten ASDEX Upgrade". In: *Phys. Plasmas* 25.5 (2018), p. 56115. ISSN: 10897674. DOI: 10.1063/1.5024320. URL: https://doi.org/10.1063/1.5024320.

[8] A Fasoli et al. "Chapter 5: Physics of energetic ions". In: *Nucl. Fusion* 47.6 (June 2007), S264–S284. ISSN: 0029-5515. DOI: 10.1088/0029-5515/47/6/S05. URL: http://stacks.iop.org/0029-5515/47/i=6/a=S05?key=crossref.0211ef97d9fd92169f235b70c5486348.

[9] Nathaniel J. Fisch. "Theory of current drive in plasmas". In: *Rev. Mod. Phys.* 59.1 (Jan. 1987), pp. 175–234. ISSN: 00346861. DOI: 10.1103/RevModPhys.59.175. arXiv: 0002114v2 [arXiv:hep-ph]. URL: https://link.aps.org/doi/10.1103/RevModPhys.59.175.

[10] B. Geiger et al. "Fast-ion transport and neutral beam current drive in ASDEX upgrade". In: *Nucl. Fusion* 55.8 (Aug. 2015), p. 083001. ISSN: 17414326. DOI: 10.1088/0029-5515/55/8/083001. URL: http://stacks.iop.org/0029-5515/55/i=8/a=083001?key=crossref.42600d0204dd9ece053d87c95587e37b.

[11] H.H Duong and W.W Heidbrink. "Confinement of fusion produced MeV ions in the DIII-D tokamak". In: *Nucl. Fusion* 33.2 (Feb. 1993), pp. 211–224. ISSN: 0029-5515. DOI: 10.1088/0029-5515/33/2/I03. URL: http://stacks.iop.org/0029-5515/33/i=2/a=I03?key=crossref.e9ee53bfb0e34f7de05de9559726b002.

[12] R. B. White et al. "Toroidal Alfvén eigenmode-induced ripple trapping". In: *Phys. Plasmas* 2.8 (Aug. 1995), pp. 2871–2873. ISSN: 1070-664X. DOI: 10.1063/1.871452. URL: http://aip.scitation.org/doi/10.1063/1.871452.

[13] W.W Heidbrink and G.J Sadler. "The behaviour of fast ions in tokamak experiments". In: *Nucl. Fusion* 34.4 (Apr. 1994), pp. 535–615. ISSN: 0029-5515. DOI: 10.1088/0029-5515/34/4/I07. URL: http://stacks.iop.org/0029-5515/34/i=4/a=I07?key=crossref.de645c8956300de674223188c1dc905c.

[14] Jun Young Kim et al. "Prompt loss of beam ions in KSTAR plasmas". In: *AIP Adv.* 6.10 (Oct. 2016), p. 105013. ISSN: 21583226. DOI: 10.1063/1.4966588. URL: http://aip.scitation.org/doi/10.1063/1.4966588.

[15] K. G. McClements et al. "Particle acceleration during merging-compression plasma start-up in the Mega Amp Spherical Tokamak". In: *Plasma Phys. Control. Fusion* 60.2 (2018), p. 025013. ISSN: 13616587. DOI: 10.1088/1361-6587/aa98fa.

[16] G.J. Kramer et al. "Fast-ion effects during test blanket module simulation experiments in DIII-D". In: *Nucl. Fusion* 51.10 (Oct. 2011), p. 103029. ISSN: 0029-5515. DOI: 10.1088/0029-5515/51/10/103029. URL: http://stacks.iop.org/0029-5515/51/i=10/a=103029?key=crossref.c42d325154bd128a41714f841ee7b5b1.

[17] W. W. Heidbrink et al. "Synergy between fast-ion transport by core MHD and test blanket module fields in DIII-D experiments". In: *Nucl. Fusion* 55.8 (Aug. 2015), p. 083023. ISSN: 17414326. DOI: 10.1088/0029-5515/55/8/083023. URL: http://stacks.iop.org/0029-5515/55/i=8/a=083023?key=crossref.06e6417ab9923e42ee926c7f965ac908.

[18] R. J. Goldston and H. H. Towner. "Effects of toroidal field ripple on suprathermal ions in tokamak plasmas". In: *J. Plasma Phys.* 26.2 (Oct. 1981), pp. 283–307. ISSN: 14697807. DOI: 10.1017/S0022377800010680. URL: http://www.journals.cambridge.org/abstract%7B%5C_%7DS0022377800010680.

[19] M Garcia-Munoz et al. "Fast-ion losses induced by ELMs and externally applied magnetic perturbations in the ASDEX Upgrade tokamak". In: *Plasma Phys. Control. Fusion* 55.12 (Dec. 2013), p. 124014. ISSN: 07413335. DOI: 10.1088/0741-3335/55/12/124014. URL: http://stacks.iop.org/0741-3335/55/i=12/a=124014?key=crossref.32e2b489206d7345014a60b85c9f2bd0.

[20] M. Garcia-Munoz et al. "Fast-ion redistribution and loss due to edge perturbations in the ASDEX Upgrade, DIII-D and KSTAR tokamaks". In: *Nucl. Fusion* 53.12 (Dec. 2013), p. 123008. ISSN: 00295515. DOI: 10.1088/0029-5515/53/12/123008. URL: http://stacks.iop.org/0029-5515/53/i=12/a=123008?key=crossref.92c0ce15bdbe231038a67aafdda30133.

[21] M A Van Zeeland et al. "Modulation of prompt fast-ion loss by applied n = 2 fields in the DIII-D tokamak". In: *Plasma Phys. Control. Fusion* 56.1 (Jan. 2014), p. 015009. ISSN: 07413335. DOI: 10.1088/0741-3335/56/1/015009. URL: http://stacks.iop.org/0741-3335/56/i=1/a=015009?key=crossref.3ceb1eb5e8b70974f5d49a3b28dd37d0.

[22] M.A. Van Zeeland et al. "Fast ion transport during applied 3D magnetic perturbations on DIII-D". In: *Nucl. Fusion* 55.7 (July 2015), p. 073028. ISSN: 0029-5515. DOI: 10.1088/0029-5515/55/7/073028. URL: http://stacks.iop.org/0029-5515/55/i=7/a=073028?key=crossref.eec860dd19985557a4bd023b9510aa62.

[23] K G McClements et al. "The effects of resonant magnetic perturbations on fast ion confinement in the Mega Amp Spherical Tokamak". In: *Plasma Phys. Control. Fusion* 57.7 (July 2015), p. 075003. ISSN: 13616587. DOI: 10.1088/0741-3335/57/7/075003. URL: http://stacks.iop.org/0741-3335/57/i=7/a=075003?key=crossref.f0eccf182145c5c64d7ba544342f9960.

[24] C. B. Forest et al. "Reduction in neutral beam driven current in a tokamak by tearing modes". In: *Phys. Rev. Lett.* 79.3 (July 1997), pp. 427–430. ISSN: 10797114. DOI: 10.1103/PhysRevLett.79.427. URL: https://link.aps.org/doi/10.1103/PhysRevLett.79.427.

[25] E. M. Carolipio et al. "Simulations of beam ion transport during tearing modes in the DIII-D tokamak". In: *Nucl. Fusion* 42.7 (July 2002), pp. 853–862. ISSN: 00295515. DOI: 10.1088/0029-5515/42/7/308. URL: http://stacks.iop.org/0029-5515/42/i=7/a=308?key=crossref.ec96508567e4ff022d17782310cfc214.

[26] M García-Muñoz et al. "NTM induced fast ion losses in ASDEX Upgrade". In: *Nucl. Fusion* 47.7 (July 2007), pp. L10–L15. ISSN: 0029-5515. DOI: 10.1088/0029-5515/47/7/L03. URL: http://stacks.iop.org/0029-5515/47/i=7/a=L03?key=crossref.29d6e674862ab0d2cbfa239e091d5ec5.

[27] W W Heidbrink et al. "The phase-space dependence of fast-ion interaction with tearing modes a". In: *Nucl. Fusion* 58.8 (Aug. 2018), p. 082027. ISSN: 0029-5515. DOI: 10.1088/1741-4326/aab7b6. URL: http://stacks.iop.org/0029-5515/58/i=8/a=082027?key=crossref.fed471c4073c7bd7f368e0c539f50757.

[28] K. McGuire et al. "Study of high-beta magnetohydrodynamic modes and fast-ion losses in PDX". In: *Phys. Rev. Lett.* 50.12 (Mar. 1983), pp. 891–895. ISSN: 00319007. DOI: 10.1103/PhysRevLett.50.891. URL: https://link.aps.org/doi/10.1103/PhysRevLett.50.891.

[29] C. Perez von Thun et al. "MeV-range fast ion losses induced by fishbones on JET". In: *Nucl. Fusion* 50.8 (Aug. 2010), p. 084009. ISSN: 00295515. DOI: 10.1088/0029-5515/50/8/084009. URL: http://stacks.iop.org/0029-5515/50/i=8/a=084009?key=crossref.d5d1b2751fcadec95ac7bd9ffc1ed5f8.

[30] C. Perez Von Thun et al. "Study of fast-ion transport induced by fishbones on JET". In: *Nucl. Fusion* 52.9 (Sept. 2012), p. 094010. ISSN: 00295515. DOI: 10.1088/0029-5515/52/9/094010. URL: http://stacks.iop.org/0029-5515/52/i=9/a=094010?key=crossref.8a1238c1078c71f328a24968ce2825b8.

[31] C. M. Muscatello et al. "Measurements of fast-ion transport by mode-particle resonances on DIII-D". In: *Nucl. Fusion* 52.10 (Oct. 2012), p. 103022. ISSN: 00295515. DOI: 10.1088/0029-5515/52/10/103022. URL: http://stacks.iop.org/0029-5515/52/i=10/a=103022?key=crossref.f230918eaf76408b30a186bc9a429050.

[32] B Geiger et al. "Quantification of the impact of large and small-scale instabilities on the fast-ion confinement in ASDEX Upgrade". In: *Plasma Phys. Control. Fusion* 57.1 (Jan. 2015), p. 014018. ISSN: 13616587. DOI: 10.1088/0741-3335/57/1/014018. URL: http://stacks.iop.org/0741-3335/57/i=1/a=014018?key=crossref.52e619017038e6e3fa09852b624d84f9.

[33] V.G. Kiptily et al. "Fusion product losses due to fishbone instabilities in deuterium JET plasmas". In: *Nucl. Fusion* 58.1 (Jan. 2018), p. 014003. ISSN: 0029-5515. DOI: 10.1088/1741-4326/aa9340. URL: http://stacks.iop.org/0029-5515/58/i=1/a=014003?key=crossref.f2b8aab371a0ac58584cf5d35d2425b6.

[34] D. S. Darrow et al. "Observations of neutral beam and ICRF tail ion losses due to Alfvén modes in TFTR". In: *Nucl. Fusion* 37.7 (July 1997), pp. 939–954. ISSN: 00295515. DOI: 10.1088/0029-5515/37/7/I03. URL: http://stacks.iop.org/0029-5515/37/i=7/a=I03?key=crossref.fe5295a0e95e66b6cec5be36c968835a.

[35] K. Shinohara et al. "Recent progress of Alfvén eigenmode experiments using N-NB in JT-60U tokamak". In: *Nucl. Fusion*. Vol. 42. 8. IOP Publishing, Aug. 2002, pp. 942–948. DOI: 10.1088/0029-5515/42/8/302. URL: http://stacks.iop.org/0029-5515/42/i=8/a=302?key=crossref.0e450569d7820de3e5af3a2cb62a562f.

[36] M Ishikawa et al. "Energetic ion transport by abrupt large-amplitude event induced by negative-ion-based neutral beam injection in the JT-60U". In: *Nucl. Fusion* 45.12 (Dec. 2005), pp. 1474–1480. ISSN: 00295515. DOI: 10.1088/0029-5515/45/12/002. URL: http://stacks.iop.org/0029-5515/45/i=12/a=002?key=crossref.01a62be7f6979b65667506c219877e87.

[37] S D Pinches et al. "Observation and modelling of fast ion loss in JET and ASDEX Upgrade". In: *Nucl. Fusion* 46.46 (Oct. 2006), pp. 904–910. ISSN: 0029-5515. DOI: 10.1088/0029-5515/46/10/S06. URL: http://stacks.iop.org/0029-5515/46/i=10/a=S06?key=crossref.f49582b1469361929ac2faeda2626185%20http://iopscience.iop.org/0029-5515/46/10/S06.

[38] E. D. Fredrickson et al. "Collective fast ion instability-induced losses in National Spherical Tokamak Experiment". In: *Phys. Plasmas*. Vol. 13. 5. American Institute of Physics, May 2006, p. 056109. DOI: 10.1063/1.2178788. URL: http://aip.scitation.org/doi/10.1063/1.2178788.

[39] M. Podest et al. "Experimental studies on fast-ion transport by Alfvén wave avalanches on the National Spherical Torus Experiment". In: *Phys. Plasmas*. Vol. 16. 5. American Institute of Physics, May 2009, p. 056104. ISBN: 1070-664X. DOI: 10.1063/1.3080724. URL: http://aip.scitation.org/doi/10.1063/1.3080724.

[40] M. García-Muñoz et al. "Fast-ion losses induced by ACs and TAEs in the ASDEX Upgrade tokamak". In: *Nucl. Fusion* 50.8 (2010), 084004(7). ISSN: 0029-5515. DOI: 10.1088/0029-5515/50/8/084004. URL: http://stacks.iop.org/0029-5515/50/i=8/a=084004?key=crossref.c66ed64022095254651a211843d2f140.

[41] M. García-Muñoz et al. "Convective and diffusive energetic particle losses induced by shear alfvén waves in the ASDEX upgrade tokamak". In: *Phys. Rev. Lett.* 104.18 (May 2010), p. 185002. ISSN: 00319007. DOI: 10.1103/PhysRevLett.104.185002. URL: https://link.aps.org/doi/10.1103/PhysRevLett.104.185002.

[42] M. A. Van Zeeland et al. "Measurements and modeling of Alfvén eigenmode induced fast ion transport and loss in DIII-D and ASDEX Upgrade". In: *Phys. Plasmas* 18.5 (May 2011), p. 056114. ISSN: 1070-664X. DOI: 10.1063/1.3574663. URL: http://aip.scitation.org/doi/10.1063/1.3574663.

[43] M. Garcia-Munoz et al. "Fast-ion transport induced by Alfvén eigenmodes in the ASDEX Upgrade tokamak". In: *Nucl. Fusion* 51.10 (Oct. 2011), p. 103013. ISSN: 00295515. DOI: 10.1088/0029-5515/51/10/103013. URL: http://stacks.iop.org/0029-5515/51/i=10/a=103013?key=crossref.0b9f41b61f624108ad28b34d9c1dbe83.

[44] D C Pace et al. "Convective beam ion losses due to Alfv??n eigenmodes in DIII-D reversed-shear plasmas". In: *Plasma Phys. Control. Fusion* 53.6 (June 2011), p. 062001. ISSN: 07413335. DOI: 10.1088/0741-3335/53/6/062001. URL: http://stacks.iop.org/0741-3335/53/i=6/a=062001?key=crossref.eda6938f0feac3546b132fe4bac54232.

[45] R. Jiménez-Gómez et al. "Alfvén eigenmodes measured in the TJ-II stellarator". In: *Nucl. Fusion* 51.3 (Mar. 2011), p. 033001. ISSN: 00295515. DOI: 10.1088/0029-5515/51/3/033001. URL: http://stacks.iop.org/0029-5515/51/i=3/a=033001?key=crossref.5891fa1e3952d6e35d19a61301da9594.

[46] S.E. Sharapov et al. "Energetic particle instabilities in fusion plasmas". In: *Nucl. Fusion* 53.10 (Oct. 2013), p. 104022. ISSN: 0029-5515. DOI: 10.1088/0029-5515/53/10/104022. URL: http://stacks.iop.org/0029-5515/53/i=10/a=104022?key=crossref.d91885d872cff7e9a518ef24ec4bebfa.

[47] Junghee Kim et al. "Initial measurements of fast ion loss in KSTAR". In: *Rev. Sci. Instrum.* Vol. 83. 10. American Institute of Physics, Oct. 2012, p. 10D305. DOI: 10.1063/1.4733550. URL: http://aip.scitation.org/doi/10.1063/1.4733550.

[48] S K Nielsen et al. "Fast-ion redistribution due to sawtooth crash in the TEXTOR tokamak measured by collective Thomson scattering". In: *Plasma Phys. Control. Fusion* 52.9 (Sept. 2010), p. 092001. ISSN: 13616587. DOI: 10.1088/0741-3335/52/9/092001. URL: http://stacks.iop.org/0741-3335/52/i=9/a=092001?key=crossref.e1e15ce8b2a4d955fc022ebfc56189d8.

[49] C M Muscatello et al. "Velocity-space studies of fast-ion transport at a sawtooth crash in neutral-beam heated plasmas". In: *Plasma Phys. Control. Fusion* 54.2 (Feb. 2012), p. 025006. ISSN: 07413335. DOI: 10.1088/0741-3335/54/2/025006. URL: http://stacks.iop.org/0741-3335/54/i=2/a=025006?key=crossref.e7965da376f525de38dec6488c52df12.

[50] B. Geiger et al. "Fast-ion transport in the presence of magnetic reconnection induced by sawtooth oscillations in ASDEX Upgrade". In: *Nucl. Fusion* 54.2 (Feb. 2014), p. 022005. ISSN: 00295515. DOI: 10.1088/0029-5515/54/2/022005. URL: http://stacks.iop.org/0029-5515/54/i=2/a=022005?key=crossref.fb25a85759a79859092c513634a06ead.

[51] J. Rasmussen et al. "Collective Thomson scattering measurements of fast-ion transport due to sawtooth crashes in ASDEX Upgrade". In: *Nucl. Fusion* 56.11 (Nov. 2016), p. 112014. ISSN: 0029-5515. DOI: 10.1088/0029-5515/56/11/112014. URL: http://stacks.iop.org/0029-5515/56/i=11/a=112014?key=crossref.0d61d374bc57804b4e76724c2e8f86fb%20http://stacks.iop.org/0029-5515/56/i=11/a=112014.

[52] D. Liu et al. "Effect of sawtooth crashes on fast ion distribution in NSTX-U". In: *Nucl. Fusion* 58.8 (Aug. 2018), p. 082028. ISSN: 0029-5515. DOI: 10.1088/1741-4326/aac64f. URL: http://stacks.iop.org/0029-5515/58/i=8/a=082028?key=crossref.c85665c3661f4606a17847865bd08901.

[53] M Cecconello and A Sperduti. "Study of the effect of sawteeth on fast ions and neutron emission in MAST using a neutron camera". In: *Plasma Phys. Control. Fusion* 60.5 (May 2018), p. 055008. ISSN: 13616587. DOI: 10.1088/1361-6587/aab6cc. URL: http://stacks.iop.org/0741-3335/60/i=5/a=055008?key=crossref.e45f2df1d451027523a2138bba8836bd.

[54] J. P. Graves et al. "Control of magnetohydrodynamic stability by phase space engineering of energetic ions in tokamak plasmas". In: *Nat. Commun.* 3 (Jan. 2012), p. 624. ISSN: 20411723. DOI: 10.1038/ncomms1622. URL: http://www.nature.com/doifinder/10.1038/ncomms1622.

[55] M. Garcia-Muñoz. "Active Control of Alfvén Eigenmodes in Magnetically Confined Toroidal Plasmas". In: *Submitt. to Plasma Phys. Control. Fusion* (2018).

[56] K. Ikeda. "Progress in the ITER Physics Basis". In: *Nucl. Fusion* 47.6 (June 2007). ISSN: 00295515. DOI: 10.1088/0029-5515/47/6/E01. URL: http://stacks.iop.org/0029-5515/47/i=6/a=E01?key=crossref.3391a8dabcfa415ae345d3defa8b1c9f.

[57] F. Wagner et al. "Regime of improved confinement and high beta in neutral-beam-heated divertor discharges of the ASDEX tokamak". In: *Phys. Rev. Lett.* 49.19 (Nov. 1982), pp. 1408–1412. ISSN: 00319007. DOI: 10.1103/PhysRevLett.49.1408. URL: https://link.aps.org/doi/10.1103/PhysRevLett.49.1408.

[58] H Zohm. "Edge localized modes (ELMs)". In: *Plasma Phys. Control. Fusion* 38.2 (Feb. 1996), pp. 105–128. ISSN: 0741-3335. DOI: 10.1088/0741-3335/38/2/001. URL: http://stacks.iop.org/0741-3335/38/i=2/a=001?key=crossref.f28892e44e8eadadb5c7b755b5fc53e6.

[59] A. W. Leonard. "Edge-localized-modes in tokamaks". In: *Phys. Plasmas* 21.9 (Sept. 2014), p. 090501. ISSN: 10897674. DOI: 10.1063/1.4894742. URL: http://aip.scitation.org/doi/10.1063/1.4894742.

[60] J.P.Freidberg. *Ideal MHD*. 1987.

[61] H. Zohm. *Magnetohydrodynamic Stability of Tokamaks*. Ed. by WILEY-VCH Verlag GmbH & Co. and KGaA. 2015. ISBN: 978-3-527-41232-7.

[62] R.B.White. "The Theory of Toroidally Confined Plasmas". In: (2001).

[63] Robert G Littlejohn. "Variational Principles of Guiding Centre Motion". In: *J. Plasma Phys.* 29.1 (1983), pp. 111–125. ISSN: 14697807. DOI: 10.1017/S002237780000060X. URL: https://doi.org/10.1017/S002237780000060X.

[64] Francis F. Chen. *Introduction to Plasma Physics and Controlled Fusion*. 1984.

[65] James A. Rome and Y. K M Peng. "The topology of tokamak orbits". In: *Nucl. Fusion* 19.9 (Sept. 1979), pp. 1205–1293. ISSN: 17414326. DOI: 10.1088/0029-5515/19/9/003. URL: http://stacks.iop.org/0029-5515/19/i=9/a=003?key=crossref.dc7aa476be9f7470549f1007675dad34.

[66] J Egedal. "Drift orbit topology of fast ions in tokamaks". In: *Nucl. Fusion* 40.9 (Sept. 2000), pp. 1597–1610. ISSN: 00295515. DOI: 10.1088/0029-5515/40/9/304. URL: http://stacks.iop.org/0029-5515/40/i=9/a=304?key=crossref.87e20cad4f2c4707a206c25ccdad2fa8.

[67] O. Sauter and Y. Martin. "Considerations on energy confinement time scalings using present tokamak databases and prediction for ITER size experiments". In: *Nucl. Fusion* 40.5 (2000), pp. 955–964. ISSN: 00295515. DOI: 10.1088/0029-5515/40/5/308. URL: http://iopscience.iop.org/article/10.1088/0029-5515/40/5/308/pdf.

[68] R.J. Hawryluk. "AN EMPIRICAL APPROACH TO TOKAMAK TRANSPORT". In: *Phys. Plasmas Close to Thermonucl. Cond.* Pergamon, Jan. 1981, pp. 19–46. ISBN: 9781483283852. DOI: 10.1016/B978-1-4832-8385-2.50009-1. URL: https://www.sciencedirect.com/science/article/pii/B9781483283852500091%20http://linkinghub.elsevier.com/retrieve/pii/B9781483283852500091.

[69] M. J. Mantsinen et al. "Analysis of ICRF-accelerated ions in ASDEX upgrade". In: *AIP Conf. Proc.* Vol. 933. 1. AIP, Oct. 2007, pp. 99–102. ISBN: 0735404445. DOI: 10.1063/1.2800558. URL: http://aip.scitation.org/doi/abs/10.1063/1.2800558.

[70] T. H. Stix. "Fast-Wave Heating of a Two-Component Plasma". In: *Nucl. Fusion* 15.5 (Oct. 1975), pp. 737–754. ISSN: 17414326. DOI: 10.1088/0029-5515/15/5/003. URL: http://stacks.iop.org/0029-5515/15/i=5/a=003?key=crossref.0c798d6602faeb8fbdd5f25a49e16be4.

[71] M Porkolab et al. "Recent progress in ICRF physics". In: *Plasma Phys. Control. Fusion* 40.8A (Aug. 1998), A35–A52. ISSN: 07413335. DOI: 10.1088/0741-3335/40/8A/004. URL: http://stacks.iop.org/0741-3335/40/i=8A/a=004?key=crossref.434a85ce021638018408e10c654eba99.

[72] Ye. O. Kazakov et al. "Efficient generation of energetic ions in multi-ion plasmas by radio-frequency heating". In: *Nat. Phys.* 13.10 (June 2017), pp. 973–978. ISSN: 1745-2473. DOI: 10.1038/nphys4167. URL: http://www.nature.com/doifinder/10.1038/nphys4167.

[73] J W Connor. *A review of models for ELMs*. Feb. 1998. DOI: 10.1088/0741-3335/40/2/003. URL: http://stacks.iop.org/0741-3335/40/i=2/a=003?key=crossref.a24ead57b16345927cf2038df6d303f1.

[74] J. W. Connor et al. "Edge Localised Modes (ELMs): Experiments and Theory". In: *AIP Conf. Proc.* Vol. 1013. 1. AIP, May 2008, pp. 174–190. DOI: 10.1063/1.2939030. URL: http://aip.scitation.org/doi/abs/10.1063/1.2939030.

[75] T. Eich et al. "ELM divertor peak energy fluence scaling to ITER with data from JET, MAST and ASDEX upgrade". In: *Nucl. Mater. Energy* 12 (Aug. 2017), pp. 84–90. ISSN: 23521791. DOI: 10.1016/j.nme.2017.04.014. URL: https://www.sciencedirect.com/science/article/pii/S2352179116302927.

[76] P. B. Snyder et al. "Edge localized modes and the pedestal: A model based on coupled peeling-ballooning modes". In: *Phys. Plasmas*. Vol. 9. 5. American Institute of Physics, May 2002, pp. 2037–2043. ISBN: 1070664X. DOI: 10.1063/1.1449463. URL: http://aip.scitation.org/doi/10.1063/1.1449463.

[77] P. B. Snyder, H. R. Wilson, and X. Q. Xu. "Progress in the peeling-ballooning model of edge localized modes: Numerical studies of nonlinear dynamics". In: *Phys. Plasmas*. Vol. 12. 5. American Institute of Physics, May 2005, pp. 1–7. ISBN: 1070664X. DOI: 10.1063/1.1873792. URL: http://aip.scitation.org/doi/10.1063/1.1873792.

[78] Alberto Loarte. *Chaos cuts ELMs down to size*. June 2006. DOI: 10.1038/nphys331. URL: http://www.nature.com/articles/nphys331.

[79] T. E. Evans et al. "Suppression of Large Edge-Localized Modes in High-Confinement DIII-D Plasmas with a Stochastic Magnetic Boundary". In: *Phys. Rev. Lett.* 92.23 (June 2004), p. 235003. ISSN: 0031-9007. DOI: 10.1103/PhysRevLett.92.235003. URL: https://link.aps.org/doi/10.1103/PhysRevLett.92.235003%20http://link.aps.org/doi/10.1103/PhysRevLett.92.235003%7B%5C%%7D5Cn%7B%5C%%7D3CGo%20to%20ISI%7B%5C%%7D3E://WOS:000221961900022.

[80] W. Suttrop et al. "First observation of edge localized modes mitigation with resonant and nonresonant magnetic perturbations in ASDEX upgrade". In: *Phys. Rev. Lett.* 106.22 (June 2011), p. 225004. ISSN: 00319007. DOI: 10.1103/PhysRevLett.106.225004. URL: https://link.aps.org/doi/10.1103/PhysRevLett.106.225004.

[81] W. Suttrop et al. "Experimental conditions to suppress edge localised modes by magnetic perturbations in the ASDEX Upgrade tokamak". In: *Nucl. Fusion* 58.9 (Sept. 2018), p. 096031. ISSN: 17414326. DOI: 10.1088/1741-4326/aace93. arXiv: 1804.00933. URL: http://stacks.iop.org/0029-5515/58/i=9/a=096031?key=crossref.c892d99977968d590772b1111d6a5300.

[82] P. T. Lang et al. "ELM pace making and mitigation by pellet injection in ASDEX upgrade". In: *Nucl. Fusion* 44.5 (May 2004), pp. 665–677. ISSN: 00295515. DOI: 10.1088/0029-5515/44/5/010. URL: http://stacks.iop.org/0029-5515/44/i=5/a=010?key=crossref.cc34cc81b26e76711d6cdd99fba3f2b7.

[83] P. T. Lang et al. "ELM pacing and trigger investigations at JET with the new ITER-like wall". In: *Nucl. Fusion* 53.7 (July 2013), p. 073010. ISSN: 00295515. DOI: 10.1088/0029-5515/53/7/073010. URL: http://stacks.iop.org/0029-5515/53/i=7/a=073010?key=crossref.eb9c51dccee72754f8483ee988efd9ab.

[84] Eleonora Viezzer. "Access and sustainment of naturally ELM-free and small-ELM regimes". In: *Nucl. Fusion* 58.11 (Nov. 2018), p. 115002. ISSN: 0029-5515. DOI: 10.1088/1741-4326/aac222. URL: http://stacks.iop.org/0029-5515/58/i=11/a=115002?key=crossref.32a8217e77eafbb62faa56d86e888d55%20http://iopscience.iop.org/article/10.1088/1741-4326/aac222.

[85] C. T. Hsu and D. J. Sigmar. "Alpha-particle losses from toroidicity-induced Alfvén eigenmodes. Part I: Phase-space topology of energetic particle orbits in tokamak plasma". In: *Phys. Fluids B* 4.6 (June 1992), pp. 1492–1505. ISSN: 08998221. DOI: 10.1063/1.860060. URL: http://aip.scitation.org/doi/10.1063/1.860060.

[86] F Zonca et al. "Physics of burning plasmas in toroidal magnetic confinement devices". In: *Plasma Phys. Control. Fusion* 48.12 B (Dec. 2006), B15–B28. ISSN: 07413335. DOI: 10.1088/0741-3335/48/12B/S02. URL: http://stacks.iop.org/0741-3335/48/i=12B/a=S02?key=crossref.5dded9e9935cc1f2098785964fcedd83.

[87] F Zonca et al. "Nonlinear dynamics of phase space zonal structures and energetic particle physics in fusion plasmas". In: *New J. Phys.* 17.1 (Jan. 2015), p. 013052. ISSN: 13672630. DOI: 10.1088/1367-2630/17/1/013052. URL: http://stacks.iop.org/1367-2630/17/i=1/a=013052?key=crossref.09b8ae4c8f6e58548c47a309b6654a32.

[88] W. W. Heidbrink. "Basic physics of Alfvn instabilities driven by energetic particles in toroidally confined plasmas". In: *Phys. Plasmas* 15.5 (May 2008), p. 055501. ISSN: 1070664X. DOI: 10.1063/1.2838239ÍŤ. URL: https://www.physics.uci.edu/%7B~%7Dwwheidbr/papers/Basic.pdf%20http://aip.scitation.org/doi/10.1063/1.2838239.

[89] F. Porcelli et al. "Solution of the drift-kinetic equation for global plasma modes and finite particle orbit widths". In: *Phys. Plasmas* 1.3 (Mar. 1994), pp. 470–480. ISSN: 1070664X. DOI: 10.1063/1.870792. URL: http://aip.scitation.org/doi/10.1063/1.870792.

[90] R. B. White. "Theory of mode-induced beam particle loss in tokamaks". In: *Phys. Fluids* 26.10 (1983), p. 2958. ISSN: 00319171. DOI: 10.1063/1.864060. arXiv: arXiv:1011.1669v3. URL: http://scitation.aip.org/content/aip/journal/pof1/26/10/10.1063/1.864060.

[91] R. B. White. "Modification of particle distributions by MHD instabilities I". In: *Commun. Nonlinear Sci. Numer. Simul.* 17.5 (May 2012), pp. 2200–2214. ISSN: 10075704. DOI: 10.1016/j.cnsns.2011.02.013. URL: https://www.sciencedirect.com/science/article/pii/S1007570411000888.

[92] David Pfefferle et al. "Impact of RMP magnetic field simulation models on fast ion losses". In: *Nucl. Fusion* 55.1 (Jan. 2015), p. 012001. ISSN: 17414326. DOI: 10.1088/0029-5515/55/1/012001. URL: http://stacks.iop.org/0029-5515/55/i=1/a=012001?key=crossref.b3d20b6269adc22a2bc688182e1ec6ce.

[93] H. E. Mynick. "Transport of energetic ions by low-n magnetic perturbations". In: *Phys. Fluids B* 5.5 (May 1993), pp. 1471–1481. ISSN: 08998221. DOI: 10.1063/1.860886. URL: http://aip.scitation.org/doi/10.1063/1.860886.

[94] H. L. Berk, B. N. Breizman, and M. Pekker. "Numerical simulation of bump-on-tail instability with source and sink". In: *Phys. Plasmas* 2.8 (Aug. 1995), pp. 3007–3016. ISSN: 1070664X. DOI: 10.1063/1.871198. URL: http://aip.scitation.org/doi/10.1063/1.871198.

[95] H. I. Berk, B. N. Breizman, and M. S. Pekker. "Simulation of Alfven-wave-resonant-particle interaction". In: *Nucl. Fusion* 35.12 (Dec. 1995), pp. 1713–1720. ISSN: 00295515. DOI: 10.1088/0029-5515/35/12/I36. URL: http://stacks.iop.org/0029-5515/35/i=12/a=I36?key=crossref.c56820a94c9f959f45a178aebe489d6c.

[96] Boris V Chirikov. *A universal instability of many-dimensional oscillator systems*. May 1979. DOI: 10.1016/0370-1573(79)90023-1. URL: https://www.sciencedirect.com/science/article/pii/0370157379900231?via%7B%5C%%7D3Dihub.

[97] Liu Chen and Fulvio Zonca. "Physics of Alfvén waves and energetic particles in burning plasmas". In: *Rev. Mod. Phys.* 88.1 (Mar. 2016), p. 015008. ISSN: 15390756. DOI: 10.1103/RevModPhys.88.015008. URL: https://link.aps.org/doi/10.1103/RevModPhys.88.015008.

[98] A. Kallenbach et al. "Overview of ASDEX upgrade results". In: *Nucl. Fusion* 57.10 (Oct. 2017), p. 102015. ISSN: 17414326. DOI: 10.1088/1741-4326/aa64f6. URL: http://stacks.iop.org/0029-5515/57/i=10/a=102015?key=crossref.b51cc0eec82d6fb09a50d1e7dccee4e2.

[99] V. Bobkov et al. "First results with 3-strap ICRF antennas in ASDEX Upgrade". In: *Nucl. Fusion* 56.8 (Aug. 2016), p. 084001. ISSN: 17414326. DOI: 10.1088/0029-5515/56/8/084001. URL: http://stacks.iop.org/0029-5515/56/i=8/a=084001?key=crossref.97938d932ea404429e6d1dbbb72c9ac8.

[100] Martin Schubert et al. "Extension of electron cyclotron heating at ASDEX Upgrade with respect to high density operation". In: *EPJ Web Conf.* Vol. 157. 2017. DOI: 10.1051/epjconf/201715703047. URL: https://www.epj-conferences.org/articles/epjconf/pdf/2017/26/epjconf%7B%5C_%7Drfppc2017%7B%5C_%7D03047.pdf.

[101] A. Mlynek et al. "Design of a digital multiradian phase detector and its application in fusion plasma interferometry". In: *Rev. Sci. Instrum.* 81.3 (Mar. 2010), p. 033507. ISSN: 00346748. DOI: 10.1063/1.3340944. arXiv: arXiv:1011.1669v3. URL: http://aip.scitation.org/doi/10.1063/1.3340944.

[102] B. Kurzan and H. D. Murmann. "Edge and core Thomson scattering systems and their calibration on the ASDEX Upgrade tokamak". In: *Rev. Sci. Instrum.* 82.10 (Oct. 2011), p. 103501. ISSN: 00346748. DOI: 10.1063/1.3643771. URL: http://aip.scitation.org/doi/10.1063/1.3643771.

[103] R Fischer, E Wolfrum, and J Schweinzer. "Probabilistic lithium beam data analysis". In: *Plasma Phys. Control. Fusion* 50.8 (Aug. 2008), p. 085009. ISSN: 0741-3335. DOI: 10.1088/0741-3335/50/8/085009. URL: http://stacks.iop.org/0741-3335/50/i=8/a=085009?key=crossref.66dc3a9cef01c87d8417ae7a2c0d3d6a.

[104] M Willensdorfer et al. "Characterization of the Li-BES at ASDEX Upgrade". In: *Plasma Phys. Control. Fusion* 56.2 (2014), pp. 25008–10. ISSN: 07413335. DOI: 10.1088/0741-3335/56/2/025008. URL: http://iopscience.iop.org/article/10.1088/0741-3335/56/2/025008/pdf.

[105] M Willensdorfer et al. "Plasma response measurements of external magnetic perturbations using electron cyclotron emission and comparisons to 3D ideal MHD equilibrium". In: *Plasma Phys. Control. Fusion* 58.11 (Nov. 2016), p. 114004. ISSN: 0741-3335. DOI: 10.1088/0741-3335/58/11/114004. arXiv: 1603.09150. URL: http://stacks.iop.org/0741-3335/58/i=11/a=114004?key=crossref.7ca319e3945448500687904873a72427.

[106] S K Rathgeber et al. "Estimation of edge electron temperature profiles via forward modelling of the electron cyclotron radiation transport at ASDEX Upgrade". In: *Plasma Phys. Control. Fusion* 55.2 (Feb. 2013), p. 025004. ISSN: 07413335. DOI: 10.1088/0741-3335/55/2/025004. URL: http://stacks.iop.org/0741-3335/55/i=2/a=025004?key=crossref.cd47f576ea988b50d7e68f622bc5a473.

[107] S.S. Denk et al. "Radiation transport modelling for the interpretation of oblique ECE measurements". In: *EPJ Web Conf.* 147.02002 (July 2017). Ed. by B.K. Shukla, H.B. Pandya, and S.L. Rao, p. 02002. ISSN: 2100-014X. DOI: 10.1051/epjconf/201714702002. URL: http://www.epj-conferences.org/10.1051/epjconf/201714702002.

[108] R. Fischer et al. "Integrated data analysis of profile diagnostics at ASDEX upgrade". In: *Fusion Sci. Technol.* 58.2 (Oct. 2010), pp. 675–684. ISSN: 15361055. DOI: 10.13182/FST10-110. URL: https://www.tandfonline.com/doi/full/10.13182/FST10-110.

[109] R. J. Fonck, D. S. Darrow, and K. P. Jaehnig. "Determination of plasma-ion velocity distribution via charge-exchange recombination spectroscopy". In: *Phys. Rev. A* 29.6 (June 1984), pp. 3288–3309. ISSN: 10502947. DOI: 10.1103/PhysRevA.29.3288. URL: https://link.aps.org/doi/10.1103/PhysRevA.29.3288.

[110] E. Viezzer et al. "High-accuracy characterization of the edge radial electric field at ASDEX Upgrade". In: *Nucl. Fusion* 53.5 (May 2013), p. 053005. ISSN: 00295515. DOI: 10.1088/0029-5515/53/5/053005. URL: http://stacks.iop.org/0029-5515/53/i=5/a=053005?key=crossref.35fe58d2aea2beffbeded1950163005c.

[111] E. Viezzer et al. "Evidence for the neoclassical nature of the radial electric field in the edge transport barrier of ASDEX Upgrade". In: *Nucl. Fusion* 54.1 (Jan. 2014), p. 12003. ISSN: 0029-5515. DOI: 10.1088/0029-5515/54/1/012003. URL: http://stacks.iop.org/0029-5515/54/i=1/a=012003?key=crossref.236e707f43703dba058508b9bec226c7%20http://iopscience.iop.org/0029-5515/54/1/012003/article/%7B%5C%%7D5Cnpapers3://publication/doi/10.1088/0029-5515/54/1/012003.

[112] E. Viezzer et al. "High-resolution charge exchange measurements at ASDEX Upgrade". In: *Rev. Sci. Instrum.* Vol. 83. 10. American Institute of Physics, Oct. 2012, p. 103501. DOI: 10.1063/1.4755810. URL: http://aip.scitation.org/doi/10.1063/1.4755810.

[113] R. M. McDermott et al. "Extensions to the charge exchange recombination spectroscopy diagnostic suite at ASDEX Upgrade". In: *Rev. Sci. Instrum.* 88.7 (July 2017), p. 073508. ISSN: 10897623. DOI: 10.1063/1.4993131. URL: http://aip.scitation.org/doi/10.1063/1.4993131.

[114] J. Gernhardt. *Magnetic diagnostic on ASDEX Upgrade with external and internal pick-up coils*. Tech. rep. Max-Planck-Insitut for Plasmaphysik, 1992.

[115] B Sieglin. "Experimental Investigation of Heat Transport and Divertor Loads of Fusion Plasmas in All Metal ASDEX Upgrade and JET". PhD thesis. Technical university Munich, 2014.

[116] B. Geiger et al. "Multi-view fast-ion D-alpha spectroscopy diagnostic at ASDEX upgrade". In: *Rev. Sci. Instrum.* 84.11 (Nov. 2013), p. 113502. ISSN: 10897623. DOI: 10.1063/1.4829481. URL: http://aip.scitation.org/doi/10.1063/1.4829481.

[117] P. A. Schneider et al. "A new compact solid-state neutral particle analyser at ASDEX Upgrade: Setup and physics modeling". In: *Rev. Sci. Instrum.* 86.7 (July 2015), p. 073508. ISSN: 10897623. DOI: 10.1063/1.4926886. URL: http://aip.scitation.org/doi/10.1063/1.4926886.

[118] S K Nielsen et al. "Measurements of the fast-ion distribution function at ASDEX upgrade by collective Thomson scattering (CTS) using active and passive views". In: *Plasma Phys. Control. Fusion* 57.3 (Mar. 2015), p. 035009. ISSN: 13616587. DOI: 10.1088/0741-3335/57/3/035009. URL: http://stacks.iop.org/0741-3335/57/i=3/a=035009?key=crossref.7365465e6f467c727eacf01f990a5b01.

[119] R. D'Inca. "Ion Cyclotron Emission on ASDEX Upgrade". PhD thesis. Ludwig Maximilian University of Munich.

[120] L. Giacomelli et al. "The compact neutron spectrometer at ASDEX Upgrade". In: *Rev. Sci. Instrum.* 82.12 (Dec. 2011), p. 123504. ISSN: 00346748. DOI: 10.1063/1.3660811. URL: http://aip.scitation.org/doi/10.1063/1.3660811.

[121] G Tardini et al. "First neutron spectrometry measurements in the ASDEX Upgrade tokamak". In: *J. Instrum.* 7.3 (2012). ISSN: 17480221. DOI: 10.1088/1748-0221/7/03/C03004. URL: http://iopscience.iop.org/article/10.1088/1748-0221/7/03/C03004/pdf.

[122] M. Garcia-Munoz, H. U. Fahrbach, and H. Zohm. "Scintillator based detector for fast-ion losses induced by magnetohydrodynamic instabilities in the ASDEX upgrade tokamak". In: *Rev. Sci. Instrum.* 80.5 (May 2009), p. 053503. ISSN: 00346748. DOI: 10.1063/1.3121543. URL: http://aip.scitation.org/doi/10.1063/1.3121543.

[123] M. Rodriguez-Ramos. "Calibración absoluta y aplicación de los detectores de pérdidas de iones rápidos basados en materiales centelleadores para dispositivos de fusión nuclear". PhD thesis. University of Seville, 2017.

[124] M. C. Jiménez-Ramos et al. "Characterization of scintillator materials for fast-ion loss detectors in nuclear fusion reactors". In: *Nucl. Instruments Methods Phys. Res. Sect. B Beam Interact. with Mater. Atoms* 332 (Aug. 2014), pp. 216–219. ISSN: 0168583X. DOI: 10.1016/j.nimb.2014.02.064. URL: http://linkinghub.elsevier.com/retrieve/pii/S0168583X14003218.

[125] M. Rodríguez-Ramos et al. "Temperature response of several scintillator materials to light ions". In: *Nucl. Instruments Methods Phys. Res. Sect. B Beam Interact. with Mater. Atoms* 403 (July 2017), pp. 7–12. ISSN: 0168583X. DOI: 10.1016/j.nimb.2017.04.084. URL: https://www.sciencedirect.com/science/article/pii/S0168583X17305360?via%7B%5C%%7D3Dihub.

[126] J. Ayllon-Guerola et al. "A fast feedback controlled magnetic drive for the ASDEX Upgrade fast-ion loss detectors". In: *Rev. Sci. Instrum.* 87.11 (Nov. 2016), 11E705. ISSN: 10897623. DOI: 10.1063/1.4959913. URL: http://aip.scitation.org/doi/10.1063/1.4959913.

[127] J. Gonzalez-Martin and Et Al. "First measurements of a scintillator based Fast-Ion Loss Detector near the ASDEX Upgrade divertor a)". In: *Rev. Sci. Instruments* 89.10 (Oct. 2018), p. 10I106. ISSN: 10897623. DOI: 10.1063/1.5038968. URL: http://aip.scitation.org/doi/10.1063/1.5038968.

[128] D. S. Darrow et al. "Measurement of loss of DT fusion products using scintillator detectors in TFTR (invited)". In: *Rev. Sci. Instrum.* 66.1 (Jan. 1995), pp. 476–482. ISSN: 00346748. DOI: 10.1063/1.1146484. URL: http://aip.scitation.org/doi/10.1063/1.1146484.

[129] R. K. Fisher et al. "Scintillator-based diagnostic for fast ion loss measurements on DIII-D". In: *Rev. Sci. Instrum.* Vol. 81. 10. American Institute of Physics, Oct. 2010, p. 10D307. ISBN: 0034-6748. DOI: 10.1063/1.3490020. URL: http://aip.scitation.org/doi/10.1063/1.3490020.

[130] X. Chen et al. "Enhanced Localized Energetic-Ion Losses Resulting from Single-Pass Interactions with Alfvén Eigenmodes". In: *Phys. Rev. Lett.* 110.6 (Feb. 2013), p. 065004. ISSN: 0031-9007. DOI: 10.1103/PhysRevLett.110.065004. URL: https://link.aps.org/doi/10.1103/PhysRevLett.110.065004.

[131] X. Chen et al. "Prompt non-resonant neutral beam-ion loss induced by Alfvén eigenmodes in the DIII-D tokamak". In: *Nucl. Fusion* 53.12 (Dec. 2013), p. 123019. ISSN: 0029-5515. DOI: 10.1088/0029-5515/53/12/123019. URL: http://stacks.iop.org/0029-5515/53/i=12/a=123019?key=crossref.aa2c1cd40faa2e435200118dbb3fac81.

[132] Xi Chen et al. "Non-linear wave-particle interactions and fast ion loss induced by multiple Alfvén eigenmodes in the DIII-D tokamak". In: *Nucl. Fusion* 54.8 (Aug. 2014), p. 083005. ISSN: 17414326. DOI: 10.1088/0029-5515/54/8/083005. URL: http://stacks.iop.org/0029-5515/54/i=8/a=083005?key=crossref.5e0b2b4e05fd79db7e883d8654d93831.

[133] M. García-Muñoz et al. "Fast-ion losses due to high-frequency MHD perturbations in the ASDEX upgrade Tokamak". In: *Phys. Rev. Lett.* 100.5 (Feb. 2008), p. 055005. ISSN: 00319007. DOI: 10.1103/PhysRevLett.100.055005. URL: https://link.aps.org/doi/10.1103/PhysRevLett.100.055005.

[134] C. Perez Von Thun et al. "Numerical simulation of fast ion loss detector measurements for fishbones on JET". In: *Nucl. Fusion* 51.5 (May 2011), p. 053003. ISSN: 00295515. DOI: 10.1088/0029-5515/51/5/053003. URL: http://stacks.iop.org/0029-5515/51/i=5/a=053003?key=crossref.0db64a58ca6f53bc79b7af41bf1c595e.

[135] S.J. Zweben. "Pitch angle resolved measurements of escaping charged fusion products in TFTR". In: *Nucl. fusion* 29.5 (May 1989), pp. 825–833. ISSN: 17414326. DOI: 10.1088/0029-5515/29/5/012. URL: http://stacks.iop.org/0029-5515/29/i=5/a=012?key=crossref.43be640d68fb87800dd8ae5cb9d1f7bb%20http://iopscience.iop.org/0029-5515/29/5/012.

[136] D. C. Pace et al. "Modeling the response of a fast ion loss detector using orbit tracing techniques in a neutral beam prompt-loss study on the DIII-D tokamak". In: *Rev. Sci. Instrum.* Vol. 81. 10. American Institute of Physics, Oct. 2010, p. 10D305. DOI: 10.1063/1.3478996. URL: http://aip.scitation.org/doi/10.1063/1.3478996.

[137] D. C. Pace et al. "Mapping and uncertainty analysis of energy and pitch angle phase space in the DIII-D fast ion loss detector". In: *Rev. Sci. Instrum.* 85.11 (Nov. 2014), p. 11D841. ISSN: 10897623. DOI: 10.1063/1.4891596. URL: http://aip.scitation.org/doi/10.1063/1.4891596.

[138] Y. P. Zhang et al. "Development of the scintillator-based probe for fast-ion losses in the HL-2A tokamak". In: *Rev. Sci. Instrum.* 85.5 (May 2014), p. 053502. ISSN: 10897623. DOI: 10.1063/1.4872385. URL: http://aip.scitation.org/doi/10.1063/1.4872385.

[139] J Galdon-Quiroga et al. "Velocity-space sensitivity and tomography of scintillator-based fast-ion loss detectors". In: *Plasma Phys. Control. Fusion* 60.10 (Oct. 2018), p. 105005. ISSN: 0741-3335. DOI: 10.1088/1361-6587/aad76e. URL: http://stacks.iop.org/0741-3335/60/i=10/a=105005?key=crossref.b42633c5760bd48362347bf45a33e689.

[140] W W Heidbrink et al. "Measurements of fast-ion acceleration at cyclotron harmonics using Balmer-alpha spectroscopy". In: *Plasma Phys. Control. Fusion* 49.9 (Sept. 2007), pp. 1457–1475. ISSN: 0741-3335. DOI: 10.1088/0741-3335/49/9/008. URL: http://stacks.iop.org/0741-3335/49/i=9/a=008?key=crossref.02c45eaba70929557244a36d0a30ee84.

[141] M. Salewski et al. "On velocity space interrogation regions of fast-ion collective Thomson scattering at ITER". In: *Nucl. Fusion* 51.8 (Aug. 2011), p. 083014. ISSN: 0029-5515. DOI: 10.1088/0029-5515/51/8/083014. URL: http://stacks.iop.org/0029-5515/51/i=8/a=083014?key=crossref.3879077a9c9c7d3584e09de32606fc1f.

[142] M Salewski et al. "On velocity-space sensitivity of fast-ion D-alpha spectroscopy". In: *Plasma Phys. Control. Fusion* 56.10 (Oct. 2014), p. 105005. ISSN: 13616587. DOI: 10.1088/0741-3335/56/10/105005. URL: http://stacks.iop.org/0741-3335/56/i=10/a=105005?key=crossref.c020255929fcda517d8ad30beefce86b.

[143] A. S. Jacobsen et al. "Velocity-space sensitivity of neutron spectrometry measurements". In: *Nucl. Fusion* 55.5 (May 2015), p. 053013. ISSN: 17414326. DOI: 10.1088/0029-5515/55/5/053013. URL: http://stacks.iop.org/0029-5515/55/i=5/a=053013?key=crossref.4b91de6049c4d2b39fb2a37e6bb9b51e.

[144] M. Salewski et al. "Velocity-space observation regions of high-resolution two-step reaction gamma-ray spectroscopy". In: *Nucl. Fusion* 55.9 (Sept. 2015), p. 093029. ISSN: 17414326. DOI: 10.1088/0029-5515/55/9/093029. URL: http://stacks.iop.org/0029-5515/55/i=9/a=093029?key=crossref.00bd9a4e5ba32267a40672909e69bf10.

[145] M. Salewski et al. "Fast-ion energy resolution by one-step reaction gamma-ray spectrometry". In: *Nucl. Fusion* 56.4 (Apr. 2016), p. 046009. ISSN: 17414326. DOI: 10.1088/0029-5515/56/4/046009. URL: http://stacks.iop.org/0029-5515/56/i=4/a=046009?key=crossref.7dddf294f278e99d189ece1d8d7222e8.

[146] A S Jacobsen et al. "Velocity-space sensitivities of neutron emission spectrometers at the tokamaks JET and ASDEX Upgrade in deuterium plasmas". In: *Rev. Sci. Instrum.* 88.7 (2017). ISSN: 10897623. DOI: 10.1063/1.4991651. URL: https://doi.org/10.1063/1.4991651%20http://aip.scitation.org/toc/rsi/88/7.

[147] W. W. Heidbrink. "Fast-ion Dα measurements of the fast-ion distribution (invited)". In: *Rev. Sci. Instrum.* 81.10 (Oct. 2010), p. 10D727. ISSN: 0034-6748. DOI: 10.1063/1.3478739. URL: http://www.ncbi.nlm.nih.gov/pubmed/21033920%20http://aip.scitation.org/doi/10.1063/1.3478739.

[148] M Rodriguez-Ramos et al. "First absolute measurements of fast-ion losses in the ASDEX Upgrade tokamak". In: *Control. Fusion* 59.10 (Oct. 2017), p. 105009. ISSN: 13616587. DOI: 10.1088/1361-6587/aa7e5f. URL: http://stacks.iop.org/0741-3335/59/i=10/a=105009?key=crossref.ae062acc34583cda326a1eae26f6dd69%20http://iopscience.iop.org/article/10.1088/1361-6587/aa7e5f/pdf.

[149] E. Hirvijoki et al. "ASCOT: Solving the kinetic equation of minority particle species in tokamak plasmas". In: *Comput. Phys. Commun.* 185.4 (2014), pp. 1310–1321. ISSN: 00104655. DOI: 10.1016/j.cpc.2014.01.014. arXiv: 1308.1904v2.

[150] Keiji Tani et al. "Effect of toroidal field ripple on fast ion behavior in a tokamak". In: *J. Phys. Soc. Japan* 50.5 (May 1981), pp. 1726–1737. ISSN: 13474073. DOI: 10.1143/JPSJ.50.1726. URL: http://journals.jps.jp/doi/10.1143/JPSJ.50.1726.

[151] J. Galdon-Quiroga et al. "Velocity space resolved absolute measurement of fast ion losses induced by a tearing mode in the ASDEX Upgrade tokamak". In: *Nucl. Fusion* 58.3 (Mar. 2018), p. 036005. ISSN: 0029-5515. DOI: 10.1088/1741-4326/aaa33b. URL: http://stacks.iop.org/0029-5515/58/i=3/a=036005?key=crossref.355c77134e045b8ad6e90f9a5266b0c4.

[152] M. Salewski et al. "Tomography of fast-ion velocity-space distributions from synthetic CTS and FIDA measurements". In: *Nucl. Fusion* 52.10 (Oct. 2012), p. 103008. ISSN: 00295515. DOI: 10.1088/0029-5515/52/10/103008. URL: http://stacks.iop.org/0029-5515/52/i=10/a=103008?key=crossref.261e4d16da4a763fa9c88b8bec43d7ca.

[153] M. Salewski et al. "Combination of fast-ion diagnostics in velocity-space tomographies". In: *Nucl. Fusion* 53.6 (June 2013), p. 063019. ISSN: 00295515. DOI: 10.1088/0029-5515/53/6/063019. URL: http://stacks.iop.org/0029-5515/53/i=6/a=063019?key=crossref.1b9670e3bff0aaee467566e3911bdca8.

[154] M. Salewski et al. "Measurement of a 2D fast-ion velocity distribution function by tomographic inversion of fast-ion D-alpha spectra". In: *Nucl. Fusion* 54.2 (Feb. 2014), p. 023005. ISSN: 0029-5515. DOI: 10.1088/0029-5515/54/2/023005. arXiv: 1509.08482. URL: http://stacks.iop.org/0029-5515/54/i=2/a=023005?key=crossref.f69c570485fe836195e4bc253fb530c0%20http://iopscience.iop.org/0029-5515/54/2/023005/article/.

[155] A S Jacobsen et al. "Inversion methods for fast-ion velocity-space tomography in fusion plasmas". In: *Plasma Phys. Control. Fusion* 58.4 (Apr. 2016), p. 045016. ISSN: 0741-3335. DOI: 10.1088/0741-3335/58/4/045016. URL: http://stacks.iop.org/0741-3335/58/i=4/a=045016?key=crossref.4e2cee4abcaac8c8c0235068cd6a2fd5.

[156] M. Salewski et al. "High-definition velocity-space tomography of fast-ion dynamics". In: *Nucl. Fusion* 56.10 (Oct. 2016), p. 106024. ISSN: 0029-5515. DOI: 10.1088/0029-5515/56/10/106024. URL: http://stacks.iop.org/0029-5515/56/i=10/a=106024?key=crossref.6f0d0c839b00897322ee5125f8b5e44e%20http://stacks.iop.org/0029-5515/56/i=10/a=106024.

[157] M. Salewski et al. "MeV-range velocity-space tomography from gamma-ray and neutron emission spectrometry measurements at JET". In: *Nucl. Fusion* 57.5 (May 2017), p. 056001. ISSN: 17414326. DOI: 10.1088/1741-4326/aa60e9. URL: http://stacks.iop.org/0029-5515/57/i=5/a=056001?key=crossref.f10873e19541f92de0a1f7e8d485cf71.

[158] V. Igochine et al. "Conversion of the dominantly ideal perturbations into a tearing mode after a sawtooth crash". In: *Phys. Plasmas* 21.11 (Nov. 2014), p. 110702. ISSN: 10897674. DOI: 10.1063/1.4902106. URL: http://aip.scitation.org/doi/10.1063/1.4902106.

[159] L.-G Eriksson, T Hellsten, and U Willen. "Comparison of time dependent simulations with experiments in ion cyclotron heated plasmas". In: *Nucl. Fusion* 33.7 (July 1993), pp. 1037–1048. ISSN: 0029-5515. DOI: 10.1088/0029-5515/33/7/I07. URL: http://stacks.iop.org/0029-5515/33/i=7/a=I07?key=crossref.70ac0f8f9f48e09cc1335ef86736041e.

[160] M J Mantsinen et al. "Analysis of ICRF Heating and ICRF-Driven Fast Ions in Recent JET Experiments". In: (2015). URL: http://www.euro-fusionscipub.org/wp-content/uploads/2015/11/EFCP150704.pdf.

[161] G. D. Kerbel and M. G. Mccoy. "Kinetic-Theory and Simulation of Multispecies Plasmas in Tokamaks Excited with Electromagnetic-Waves in the Ion-Cyclotron Range of Frequencies". In: *Phys. Fluids* 28.1985 (1985), pp. 3629–3653. ISSN: 1070-6631. DOI: 10.1063/1.865319. URL: http://scitation.aip.org/content/aip/journal/pof1/28/12/10.1063/1.865319%20//a1985avl5300026.

[162] J. Galdon-Quiroga et al. "Beam-Ion Acceleration during Edge Localized Modes in the ASDEX Upgrade Tokamak". In: *Phys. Rev. Lett.* 121.2 (July 2018), p. 025002. ISSN: 10797114. DOI: 10.1103/PhysRevLett.121.025002. URL: https://link.aps.org/doi/10.1103/PhysRevLett.121.025002.

[163] J Galdon-Quiroga et al. "Observation of accelerated beam ion population during edge localized modes in the ASDEX Upgrade tokamak". In: *submitted to Nucl. Fusion* (2018).

[164] Todd E. Evans et al. "Edge stability and transport control with resonant magnetic perturbations in collisionless tokamak plasmas". In: *Nat. Phys.* 2.6 (June 2006), pp. 419–423. ISSN: 1745-2473. DOI: 10.1038/nphys312. URL: http://www.nature.com/doifinder/10.1038/nphys312.

[165] W Suttrop et al. "Experimental studies of high-confinement mode plasma response to non-axisymmetric magnetic perturbations in ASDEX Upgrade". In: *Plasma Phys. Control. Fusion* 59.1 (Jan. 2017), p. 014049. ISSN: 13616587. DOI: 10.1088/0741-3335/59/1/014049. URL: http://stacks.iop.org/0741-3335/59/i=1/a=014049?key=crossref.76fe128ab2daa52c8320e1ed0fb4a787.

[166] Maraschek M. Igochine V., Gude A. and ASDEX Upgrade Team. *Hotlink based soft x-ray diagnostic on ASDEX Upgrade*. Tech. rep. Max Planck Institute for Plasma Physics, 2010. URL: http://pubman.mpdl.mpg.de/pubman/item/escidoc:2140623:1/component/escidoc:2140622/IPP%7B%5C_%7D1%7B%5C_%7D338.pdf.

[167] Matthias Willensdorfer et al. "Dynamics of ideal modes and subsequent ELM crashes in 3D tokamak geometry from external magnetic perturbations". In: *Plasma Phys. Control. Fusion* (Aug. 2018). ISSN: 0741-3335. DOI: 10.1088/1361-6587/aadc39. URL: http://iopscience.iop.org/article/10.1088/1361-6587/aadc39.

[168] S. J. Freethy et al. "Electron kinetics inferred from observations of microwave bursts during edge localized modes in the mega-amp spherical tokamak". In: *Phys. Rev. Lett.* 114.12 (Mar. 2015), p. 125004. ISSN: 10797114. DOI: 10.1103/PhysRevLett.114.125004. arXiv: arXiv:1411.0842v1. URL: https://link.aps.org/doi/10.1103/PhysRevLett.114.125004.

[169] G.T.A Huysmans and O Czarny. "MHD stability in X-point geometry: simulation of ELMs". In: *Nucl. Fusion* 47.7 (July 2007), pp. 659–666. ISSN: 0029-5515. DOI: 10.1088/0029-5515/47/7/016. URL: http://stacks.iop.org/0029-5515/47/i=7/a=016?key=crossref.54c4a396297481f3a5413a556faf8695.

[170] Felician Mink et al. "Toroidal mode number determination of ELM associated phenomena on ASDEX Upgrade". In: *Plasma Phys. Control. Fusion* 58.12 (Dec. 2016), p. 125013. ISSN: 13616587. DOI: 10.1088/0741-3335/58/12/125013. URL: http://stacks.iop.org/0741-3335/58/i=12/a=125013?key=crossref.c85dabfb71712cc67d14b5af1550c3eb.

[171] L Sanchis-Sanchez et al. "Main Parametric Dependencies of the Fast-Ion Edge Resonant Transport Layer Induced by 3D Perturbative Fields in the ASDEX Upgrade Tokamak". In: *Submitt. to Plasma Phys. Control. Fusion* (2018).

[172] H. Dreicer. "Electron and ion runaway in a fully ionized gas. I". In: *Phys. Rev.* 115.2 (Jan. 1959), pp. 238–249. ISSN: 0031899X. DOI: 10.1103/PhysRev.115.238. arXiv: arXiv:1011.1669v3. URL: https://link.aps.org/doi/10.1103/PhysRev.117.329%20https://link.aps.org/doi/10.1103/PhysRev.115.238.

[173] S. Eilerman et al. "Runaway of energetic test ions in a toroidal plasma". In: *Phys. Plasmas* 22.2 (Feb. 2015), p. 020702. ISSN: 10897674. DOI: 10.1063/1.4907662. URL: http://aip.scitation.org/doi/10.1063/1.4907662.

[174] M. Garcia-Munoz et al. "Conceptual design of the ITER fast-ion loss detector". In: *Rev. Sci. Instrum.* 87.11 (Nov. 2016), p. 11D829. ISSN: 0034-6748. DOI: 10.1063/1.4961295. URL: http://aip.scitation.org/doi/10.1063/1.4961295.

[175] J. F. Rivero-Rodriguez et al. "A rotary and reciprocating scintillator based fast-ion loss detector for the MAST-U tokamak". In: *Rev. Sci. Instrum.* 89.10 (Oct. 2018), p. 10I112. ISSN: 0034-6748. DOI: 10.1063/1.5039311. URL: http://aip.scitation.org/doi/10.1063/1.5039311.

[176] L. Stagner and W. W. Heidbrink. "Action-angle formulation of generalized, orbit-based, fast-ion diagnostic weight functions". In: *Phys. Plasmas* 24.9 (Sept. 2017), p. 092505. ISSN: 10897674. DOI: 10.1063/1.4990391. URL: http://aip.scitation.org/doi/10.1063/1.4990391.

[177] P. Helander et al. "Ion Acceleration during Reconnection in MAST". In: *Phys. Rev. Lett.* 89.23 (Nov. 2002), p. 235002. ISSN: 0031-9007. DOI: 10.1103/PhysRevLett.89.235002. URL: https://link.aps.org/doi/10.1103/PhysRevLett.89.235002.

[178] M. Øieroset et al. "Evidence for Electron Acceleration up to 300 k e V in the Magnetic Reconnection Diffusion Region of Earth's Magnetotail". In: *Phys. Rev. Lett.* 89.19 (Oct. 2002), p. 195001. ISSN: 0031-9007. DOI: 10.1103/PhysRevLett.89.195001. URL: https://link.aps.org/doi/10.1103/PhysRevLett.89.195001.

[179] J. Egedal, W. Daughton, and A. Le. "Large-scale electron acceleration by parallel electric fields during magnetic reconnection". In: *Nat. Phys.* 8.4 (Feb. 2012), pp. 321–324. ISSN: 1745-2473. DOI: 10.1038/nphys2249. URL: http://www.nature.com/doifinder/10.1038/nphys2249.

[180] K G McClements and M R Turnyanskiy. "Energetic particles in laboratory, space and astrophysical plasmas". In: *Plasma Phys. Control. Fusion* 59.1 (Jan. 2017), p. 014012. ISSN: 13616587. DOI: 10.1088/0741-3335/59/1/014012. URL: http://stacks.iop.org/0741-3335/59/i=1/a=014012?key=crossref.0247cc97463457c9f0b68322d863d1ce.

[181] W Fundamenski et al. "On the relationship between ELM filaments and solar flares". In: *Plasma Phys. Control. Fusion* 49.5 (May 2007), R43–R86. ISSN: 07413335. DOI: 10.1088/0741-3335/49/5/R01. URL: http://stacks.iop.org/0741-3335/49/i=5/a=R01?key=crossref.9be20b88be0672cc8a8257cbc421e528.

[182] J Galdon-Quiroga et al. "Conceptual design of a scintillator based Imaging Heavy Ion Beam Probe for the ASDEX Upgrade tokamak ." In: *J. Instrum.* 12 (Aug. 2017), p. C08023. ISSN: 17480221. DOI: 10.1088/1748-0221/12/08/C08023. URL: http://stacks.iop.org/1748-0221/12/i=08/a=C08023?key=crossref.4b102dbd8a84aa8fc72437a5c1f917b5.

[183] H. Meyer et al. "Overview of progress in European medium sized tokamaks towards an integrated plasma-edge/wall solution". In: *Nucl. Fusion* 57.10 (Oct. 2017), p. 102014. ISSN: 0029-5515. DOI: 10.1088/1741-4326/aa6084. URL: http://stacks.iop.org/0029-5515/57/i=10/a=102014?key=crossref.2017887bb6c99f0f75fed0a4997e0542.

[184] J. Ayllon-Guerola. "Dynamic and thermal simulations of a fast-ion loss detector for ITER". In: *Fusion Eng. Des.* 123 (Nov. 2017), pp. 807–810. ISSN: 0920-3796. DOI: 10.1016/J.FUSENGDES.2017.04.071. URL: http://www.sciencedirect.com/science/article/pii/S092037961730474X?via%7B%5C%%7D3Dihub.

[185] G. Giruzzi et al. "Physics and operation oriented activities in preparation of the JT-60SA tokamak exploitation". In: *Nucl. Fusion* 57.8 (Aug. 2017), p. 085001. ISSN: 0029-5515. DOI: 10.1088/1741-4326/aa7962. URL: http://stacks.iop.org/0029-5515/57/i=8/a=085001?key=crossref.41409c0230d45f9adf24102fa22159e1.

[186] E Viezzer et al. "Ion heat transport dynamics during edge localized mode cycles at ASDEX Upgrade". In: *Nucl. Fusion* 58.2 (Feb. 2018), p. 026031. ISSN: 17414326. DOI: 10.1088/1741-4326/aaa22f. URL: http://stacks.iop.org/0029-5515/58/i=2/a=026031?key=crossref.ded908319292b5944e4d7c0059067322.

[187] S E Sharapov et al. "The effects of electron cyclotron heating and current drive on toroidal Alfvén eigenmodes in tokamak plasmas". In: *Plasma Phys. Control. Fusion Plasma Phys. Control. Fusion* 60.1 (Jan. 2018), pp. 14026–10. ISSN: 0741-3335. DOI: 10.1088/1361-6587/aa90ee. URL: http://stacks.iop.org/0741-3335/60/i=1/a=014026?key=crossref.870796797bb44fb7cc78fc032f333fbd%20https://doi.org/10.1088/1361-6587/aa90ee.

[188] J. Gonzalez-Martin et al. "First measurements of a scintillator based fast-ion loss detector near the ASDEX Upgrade divertor". In: *Rev. Sci. Instrum.* 89.10 (Oct. 2018), p. 10I106. ISSN: 10897623. DOI: 10.1063/1.5038968. URL: http://aip.scitation.org/doi/10.1063/1.5038968.

[189] M Garcia-Muñoz et al. "Active Control of Alfvén Eigenmodes in Magnetically Confined Toroidal Plasmas". In: *Submitt. to Plasma Phys. Control. Fusion* (2018).

[190] J. Galdon-Quiroga et al. "The synthetic fast-ion loss detector (Poster)". In: *1st European Conference on Plasma Diagnostics*. Frascati. 2015.

[191] J. Galdon-Quiroga et al. "Analysis of fast-ion heat load induced by tearing fluctuations in the ASDEX Upgrade tokamak (Poster)". In: *14th IAEA Technical Meeting on Energetic Particles in Magnetic Confinement Systems*. Vienna. 2015.

[192] J. Galdon-Quiroga et al. "Experimental evidence of beam ion acceleration during ELMs in the ASDEX Upgrade tokamak (Oral)". In: *15th IAEA Technical Meeting on Energetic Particles in Magnetic Confinement Systems*. Princeton. 2017.

[193] J. Galdon-Quiroga et al. "Acceleration of beam ions during edge localized modes in the ASDEX Upgrade tokamak (Poster)". In: *45th EPS Conference on Plasma Physics*. Prague. 2018.

[194] J. Galdon-Quiroga et al. “Impact of an edge resonant transport layer on fast-ion confinement in the ASDEX Upgrade tokamak (Poster)”. In: *27th IAEA Fusion Energy Conference*. Gandhinagar. 2018.